The Thesis Committee for Daniel K. Coleman
Certifies that this is the approved version of the following thesis:

Evaluation of Concrete Modeling in LS-DYNA for Seismic Application

APPROVED BY
SUPERVISING COMMITTEE:

Supervisor:

Eric Williamson

Michael Engelhardt

Evaluation of Concrete Modeling in LS-DYNA for Seismic Application

by

Daniel K. Coleman, B.S.C.E

Thesis

Presented to the Faculty of the Graduate School of

The University of Texas at Austin

in Partial Fulfillment

of the Requirements

for the Degree of

Master of Science in Engineering

The University of Texas at Austin

December 2016

Dedication

To my mom, dad, and brother, for their love and support over the past twenty-four years of my life. Words can't express the love that I have for each one of you.

Acknowledgements

First and foremost, I would like to thank God for every opportunity and gift that I've been given. I'm truly blessed to have had the chance to attend the University of Texas and pursue a degree in a field that I'm passionate about. To Him be all the glory.

To my family, thank you for everything you've done to support me through the years. You've always encouraged me to take risks and seek my dreams, taught me how to persevere through adversity, and reminded me to stay humbled and treat others with love and respect regardless of what I achieve. My bright future is surely a testament to the foundation you all built around me.

To my Advisor, Dr. Williamson, thank you for your guidance and support these past two years. I look forward to working with you in the blast design industry for years to come.

Abstract

Evaluation of Concrete Modeling in LS-DYNA for Seismic Application

Daniel K. Coleman, M.S.E

The University of Texas at Austin, 2016

Supervisor: Eric Williamson

LS-DYNA is a versatile finite element analysis program that can be used as a highly effective tool for solving a wide range of structural engineering problems. The software's capabilities are highly desirable for studying the response of structures under earthquakes due to the large number of independent design parameters that can be considered. Because LS-DYNA has been utilized primarily for blast and impact simulations, however, limited effort has been expended to validate the material models used within the software for seismic-resistant design applications.

The objective of this study was to evaluate the performance of four commonly used LS-DYNA concrete models (*MAT 072R*3, *MAT 084*, *MAT 159*, and *MAT 272*) for seismic applications. The first phase of analysis used individual elements to demonstrate the effects of element size, element formulation, hourglass formulation, and strain application rate on each material model's performance. Additional single-element analyses were conducted to investigate each model's capability to accurately capture different components of seismic loading, such as shear, cyclic compression, and cyclic load reversal. This single-element study yielded a collection of strengths and weaknesses associated with each material

model. The second phase of analysis investigated how the strengths and weaknesses identified in the single-element analyses applied to multi-element simulations. This portion of the research was accomplished by replicating two experimental programs and observing and analyzing the differences between the generated numerical results and the documented experimental results.

Based on observations from the single-element and multi-element studies, a series of limitations and recommendations pertaining to each material model were developed. *MAT 072R3* and *MAT 272* were not recommended for use with seismic applications due to damage accumulation limitations and hourglass control restrictions, respectively. Both *MAT 084* and *MAT 159* demonstrated they include all the necessary capabilities to be used for seismic problems; nonetheless, users should understand that there is some inherent error when applying these models. Additionally, it was observed that both *MAT 084* and *MAT 159* overpredicted energy dissipation by more than 200%. As a result, the current version of LS-DYNA is not recommended for problems with imposed acceleration histories.

Table of Contents

List of Tables

List of Figures

CHAPTER 1: INTRODUCTION

1.1 MOTIVATION

Seismic-resistant design of structures has developed considerably over the past several decades due to extensive research, including detailed experimental testing programs and careful observation following seismic events. This last category, careful observation following seismic events, offers engineers a chance to understand how structures designed in accordance with various building code provisions (IBC, ACI, AISC, etc.) faired against an actual earthquake. In essence, the seismic event becomes a large-scale experimental testing program where engineers are given ample opportunity to evaluate how various structural systems behave. While this is a great learning opportunity for designers and has contributed considerably to our understanding of how structures perform under seismic events, the associated damage and casualties are a reminder that learning prior to a disaster is significantly more desired than learning after a disaster. With every seismic event it becomes clear that significant amounts of research are still needed to limit the loss of life and economic impact that earthquakes can have. Researchers need to take a proactive role prior to seismic events rather than relying on damage seen in actual earthquakes to dictate design changes.

Current design codes, especially in countries with frequent seismic activity such as the United States (IBC), Japan (BSLJ), and New Zealand (NZS), are fairly robust and give designers extensive guidance as to what systems and details will perform adequately under seismic loading. However, these various codes have seen significant revision over the past several decades, and many buildings have been constructed using what are now known to be out-of-date construction techniques, detailing choices, and lateral system designs. This means that field research need not only focus on current design, but also consider designs

that have been used over the past several decades. The breadth of required future research is expansive.

Experimental testing is a common method for filling this research gap. It provides a researcher with the opportunity to test specimens identical to what would be used in the field, observe behavior under specified conditions, and adjust configurations to observe the effects that different variables have on a system's performance. Experimental testing has been used since the development of the scientific method and will clearly be used for decades to come. The drawback of testing physical systems, however, is that the experiments are often expensive, time consuming, and limited in scope because it's difficult to test a broad array of variables. These limitations pose problems for addressing a research gap with numerous combinations of materials and configurations. In summary, experimental testing, while effective, is a laborious process that requires decades to work through the extent of variables present in many design problems.

An alternative approach to investigating how different variables affect system response is numerical modeling. This technique, routinely implemented through use of the finite element method, was first developed back in the 1950s. This approach is popular in the academic and professional world because of its ease of use and speed at which it yields results. The technique allows a user to define a series of line, shell, or solid elements and uses various integration techniques to estimate such quantities as displacement under specified boundary conditions. The technique, which had humble beginnings and could be tracked using hand-based solutions, is now a robust process that can be carried out on several different software platforms with thousands of variables. The progression of speed and power of computers has undoubtedly allowed for a big breakthrough in the field of numerical modeling. It's now possible to simulate countless scenarios bridging different material and geometrical combinations. While numerical modeling does require a

knowledgeable user to build the model, a sophisticated software package to run the simulation, and time for data analysis, the generated solution is relatively cheap, fast, and flexible as compared to experimental testing. This makes numerical modeling an ideal tool for bridging the current seismic design gap. As software becomes even more robust, numerical modeling will become a more popular tool; therefore, it is paramount that researchers gain an understanding for how systems can be accurately modeled under seismic loading.

Even as the popularity of numerical modeling increases, experimental testing still has a valuable role in the process. Without first understanding how a physical system behaves, it is impossible to know if numerically generated results are reliable. Therefore, it is necessary to do what is called experimental validation; a process where identical physical and numerical models are constructed and direct comparison between the two is made. The goal of this process is to provide the software user confidence in the numerically generated results. Once this confidence has been established, the model can be relatively quickly reconfigured for a unique combination of variables. If the validation has been done properly and yielded a positive outcome, the results can be accepted with confidence, and the knowledge base can be expanded.

To better understand this process, consider the lateral resistance provided by a steel beam and column connected together by a simple shear connection with an overlaying concrete floor. Such a configuration, which has been used for many decades, can be found in buildings throughout the United States. Historically, such an arrangement would not be considered part of the lateral-force resisting system because a moment-resisting connection has not been used to join the beam and column. Despite this idealization, it is hypothesized that even members connected with “simple shear” connections may be able to provide some lateral resistance. An understanding of this capacity can be important in evaluating

the seismic risk to existing structures. It may also be important in evaluating the possibility of upgrading an existing structure, which would require adherence to current building code provisions that are likely more stringent than the provisions under which an older building was originally designed. While older buildings could be upgraded by retrofitting the lateral-force resisting system, this option is often prohibitively expensive. If the lateral resistance of possibly hundreds of simple shear connections already within the building could be reliably computed and counted upon for lateral strength, however, the building may meet current code requirements without any further retrofit. Experimental testing of such a scenario can be highly effective in this specific instance; however, there is a large matrix of variables (e.g., concrete decking orientation, concrete decking reinforcement layout, selected simple shear detail, etc.) that would require considerable time and money to be spent to understand every unique system combination. To solve this problem, experimental testing can be performed on a variety of system combinations, and numerical models can be validated against such physical results. Once confidence has been established, the numerical models can be altered to fill in the remaining combinations of variables. Thus, numerical modeling, paired with experimental testing, can be used as a highly efficient tool to fill in wide-spanning research gaps.

As previously mentioned, it takes a knowledgeable user to build a numerical model that can be considered reliable. Although any user can generate a model that may seem to match experimental results, models built by untrained users can often yield the correct results for the wrong reasons. That is, multiple mistakes may inadvertently cancel each other out, leading to results that seem to agree with the "correct" answer. To avoid this problem, it's important to understand the various parameters of a numerical model because it is the aggregated parameter response that drives the behavior of the system. Note that because there are many different parameters within a numerical model, there are multiple

levels of experimental validation that must be performed. The numerical model must be validated on a system level as well as on a parameter level if the results are to be considered reliable.

1.2 Objectives And Scope

The overarching goal of this study is to understand, and experimentally validate, the seismic response of concrete. Understanding the seismic response of LS-DYNA concrete models will allow users to more confidently implement concrete components into their models. Consider the previously mentioned example regarding a steel beam and column connected together by a simple shear connection with a composite concrete floor. The information provided in this thesis is intended to provide users with a means of confidently adding the concrete floor into a numerical model of a typical steel-framed building system. In a more general sense, this research is intended to expand the breadth of knowledge such that the LS-DYNA platform can be confidently used to bridge the before-mentioned seismic design gap. This will be accomplished by providing the reader with an overview of the seismic performance of the various concrete models, as well as a list of recommendations and limitations associated with each material model's seismic response.

1.3 Organization

This thesis is organized as follows:

- Chapter 2 includes a technical background on the various numerical modeling parameters used throughout the validation study. Included within this section is a background, brief history, and list of previous validation studies performed on the selected LS-DYNA concrete models. Previous

seismic validation studies on various software platforms are also included in this chapter.

- Results from single-element validation studies, as well as discussion regarding the LS-DYNA keycard definitions used with these models, are presented in Chapter 3. Analysis of the single-element model results is also detailed at the end of Chapter 3.
- Results from multi-element validation studies, as well as discussion regarding the LS-DYNA keycard definitions used with these models, are presented in Chapter 4. Analysis of the multiple-element validation results is provided at the end of Chapter 4.
- A summary of results from Chapters 3 and 4 as well as a set of conclusions are presented in Chapter 5. This includes a list of recommendations and limitations associated with each of the selected LS-DYNA concrete models and general remarks regarding seismic modeling in LS-DYNA.
- LS-DYNA keycard definitions used in the multi-element validation effort are included in Appendix A.

CHAPTER 2: BACKGROUND INFORMATION

2.1 FEA PARAMETER BACKGROUND

While the objective of this thesis is to validate four concrete material models for computing structural response under seismic loading, the behavioral response of a finite element model is sensitive to several additional parameters including: boundary conditions, strain-rate effects, element formulation, hourglass stabilization, and geometric considerations. Because these additional parameters can play a pivotal role in the material model's response, it is essential to understand how they can be defined. This section details how previous studies have defined each parameter and presents a series of recommendations, provided by previous researchers, as to how each parameter should be defined for various situations. Note that specific definitions, as they pertain to the validation presented in this thesis, will be discussed in Chapters 3 and 4.

2.1.1 BOUNDARY CONDITIONS

As they apply to single element studies, boundary conditions (pin constraints, roller constraints, etc.) can be incorporated into a numerical model using one of two different methods. The first technique simply prescribes a series of constraints to each node of the single element [DYNA-Manual, 2012]. The second technique prescribes three planes of symmetry within the model, thus requiring only a single node of the element to be constrained. This second technique ensures a state of uniform strain and stress within the element [Crawford et. al., 2012]. The following section provides an example of the two different techniques as they are applied in practice.

The first technique is commonly utilized when performing a patch test. A patch test is a numerical simulation run with only a few elements designed to ensure an element's convergence (thus testing its consistency and stability) [Schwer et al, 2005]. Note that

while patches are commonly comprised of a few elements, a patch can also be defined using a single element [Zienkiewicz, 1997]. Figure 2-1 shows the exploded view of a patch test designed to verify the consistency of several different hourglass formulations used within LS-DYNA. The authors of this study used the first technique with, explicitly defined boundary conditions for their verification study. Prescribed motion, which is an alternative to simple constraints such as a roller or pin, was applied to each of the eight exterior overlapping nodes [Schwer et al, 2005].

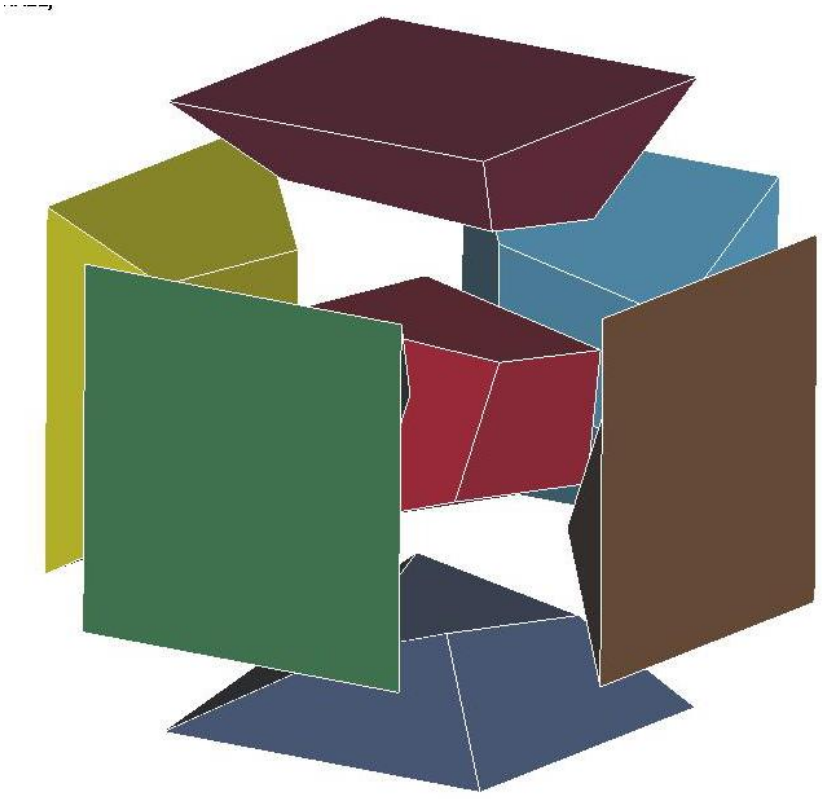

Figure 2-1: Exploded view of a 3D patch test assembly [Schwer et al, 2005]

An example of such boundary conditions applied to a single element test can be found in a validation performed on the Winfrith concrete model. As part of this validation,

a test was run on a single cube element. The top four corners of the element were prescribed a vertical, z-direction, displacement curve while the bottom four corners of the element were fixed against z-direction displacement. Note that the element was allowed to freely expand in the out-of-plane directions [Schwer, 2011].

The second technique, which utilizes a series of symmetry planes, has traditionally been used for various single element analyses as it provides a convenient way ensure element stability. Figure 2-2 shows an example of a study that used three planes of symmetry and one explicitly defined constraint to adequately limit the element's degrees of rigid body motion. This particular test was designed to evaluate concrete compressive strength under confined conditions [Crawford et. al., 2012]. The applied boundary conditions performed as expected.

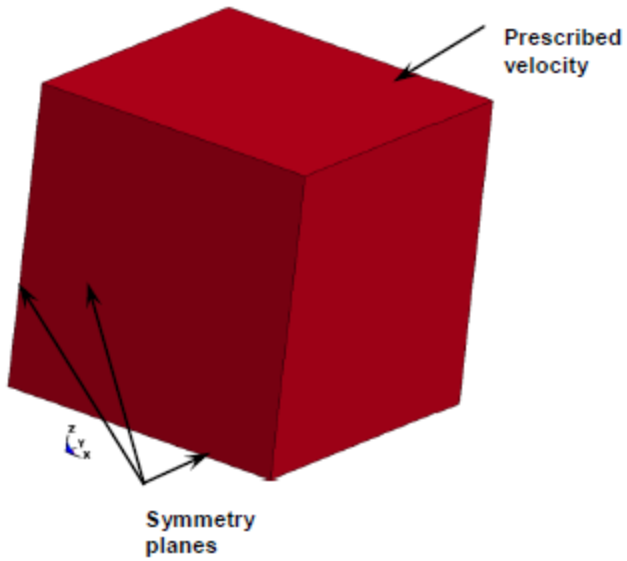

Figure 2-2: Singe element model with three planes of symmetry [Crawford et. al., 2012]

2.1.2 STRAIN RATE EFFECTS

Load application speed, and the resulting strain rate, is an important issue to address as it can have a dramatic impact on the exhibited material response [Bischof, 1991]. When considering validation for a new application, it is important to consider the expected strain rates that may occur at any time in a given analysis and to understand the anticipated impacts that these strain rates will have on the material's response. Because concrete, like most civil engineering materials, is rate sensitive, higher rates can affect the material's strength, stiffness, and ductility [Bischof, 1991]. Traditionally, these strain rate effects are added to a model through what is known as a dynamic increase factor (DIF). Material properties under expected dynamic loads are then simply calculated by multiplying the static properties of the material by the appropriate DIF [Bischof, 1991].

Figure 2-3 shows that the anticipated strain rate for earthquake problems can range anywhere from 10^{-4} per second to as much as 10 per second. This range of strain rates, as shown in Figure 2-4, can result in a DIF factor range of approximately 1 to 1.5 [Pjak, 2011]. Such a range indicates that strain rate enhancement is important for seismic applications.

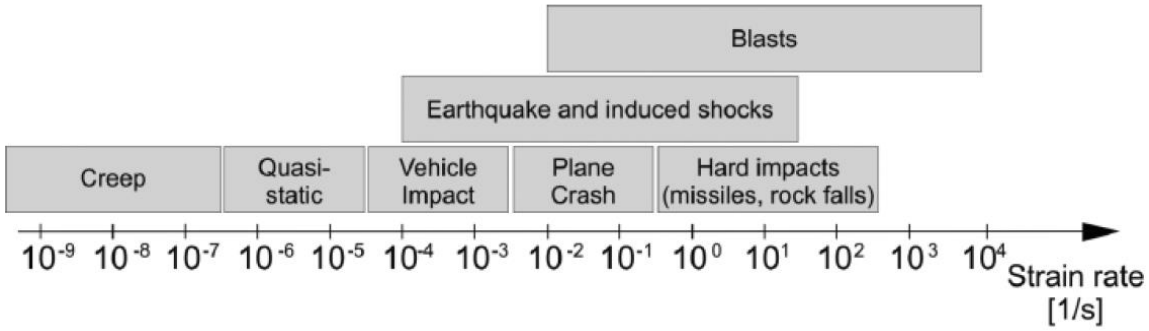

Figure 2-3: Anticipated strain rates for different types of load [Pajak, 2011]

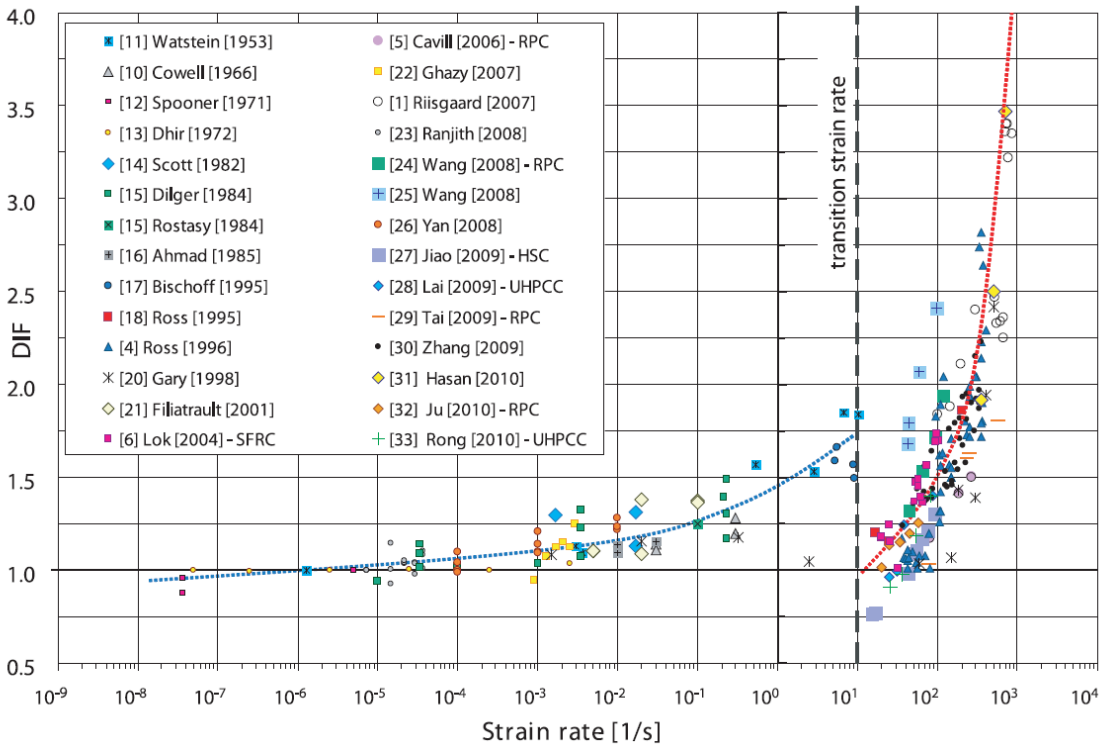

Figure 2-4: Strain rate effect on the compressive strength of concrete [Pajak, 2011]

Strain rate enhancement is incorporated into the material models described in this thesis in one of two ways. The KCC model requires the user to specify a load curve indicating the specific DIF factors to be used. The Winfrith, CSC, and RHT models, however, all have DIF factors built into their formulation [Crawford, 2012]. Note that the user must activate the DIF function in the material definition for each of these three models [DYNA-Manual, 2012].

2.1.3 Element Formulation

The validation presented in this thesis pertains to 8-noded hexahedral elements (i.e., "brick" elements). Definition of these solid brick elements includes a geometric definition (i.e., defining where the nodes of the elements are to be located) and an integration definition [DYNA-Manual, 2012]. The integration definition determines the number of

integration points defined within the element, which also determines the variation of stress and strain over the element.

The two most popular integration definitions used within LS-DYNA are full integration and reduced integration [Schwer et al, 2005]. In two dimensions, a full integration definition produces four integration points within the area of a quadrilateral element with only displacement degrees of freedom at the nodes, while a reduced integration definition uses only one integration point within the area of such an element. These definitions, as applied to an 8-noded hexahedral element, can be simply extrapolated into a three-dimensional environment, where fully integrated elements have eight integration points and reduced integration elements still have only a single integration point [DYNA-Manual, 2012]. Figure 2-5 shows an example of an element assigned a reduced integration definition, shown to the left, and an element assigned a full integration definition, shown to the right. The integration points have been marked using an "X."

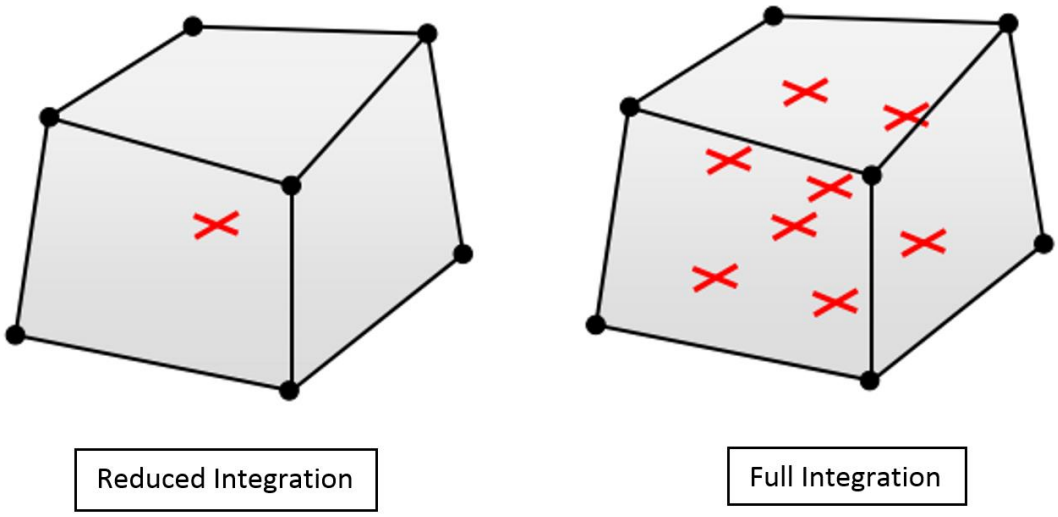

Figure 2-5: An element defined using reduced integration and full integration [DYNA-Manual, 2012]

Note that two integration points over the length an element allows the element to consider a linear variation of stress and strain over the defined length. The drawback of reduced integration is that, with only a single integration point defined over the length, the element can only consider a state of constant stress and strain [DYNA-Manual, 2012]. Additionally, with only a single integration point within the volume of the solid, the element is susceptible to zero energy deformation modes [Schwer et al, 2005]. Additional discussion on these zero energy deformation modes is provided in Section 2.1.4.

While reduced integration elements do have several limitations, they also offer much improved efficiency as compared to their fully integrated counterparts. It has been shown that runtimes can be reduced by as much as an order of magnitude by simply switching from full integration to reduced integration [DYNA-Manual, 2012]. This superior efficiency is why the reduced integration definition is LS-DYNA's default option and likely the most used element type in LS-DYNA [Schwer et al, 2005].

It should also be noted that the full integration definition most commonly used in LS-DYNA, *ELFORM 2*, is susceptible to transverse shear locking, especially in elements with poor aspect ratios. Definitions *ELFORM -1* and *ELFORM -2* have both been introduced into LS-DYNA as full integration options that aim to mitigate this transverse shear locking problem [Livemore, 2006]. Although these definitions have been shown to help convergence in cases dominated by shear locking, they have also been shown to be significantly less efficient than both reduced integration and the typical full integration [Livemore, 2006]. Because of this drawback, and the infrequency of such transverse shear locking problems occurring, these definitions are less commonly used.

2.1.4 HOURGLASS STABILIZATION

Hourglass stabilization is often incorporated into models with under-integrated elements to address the elements' tendencies to exhibit zero energy deformation modes. An example of such a mode is shown in Figure 2-6. Note that although the element has clearly undergone deformation, the dimensions of the element relative to the integration point have remained unchanged. This means that the present displacement has produced zero internal strain energy within the element. These non-physical deformation modes are typically addressed by introducing internal forces, depicted as "F1" through "F4" in Figure 2-6, into the model to prevent hourglass modes [Livemore, 2006]. Note that the work done by these artificial forces, or hourglass energy, takes away from the overall energy of the system and thus must be monitored. It is recommended that the calculated hourglass energy not exceed 10% of the total internal energy [Baeck et al.].

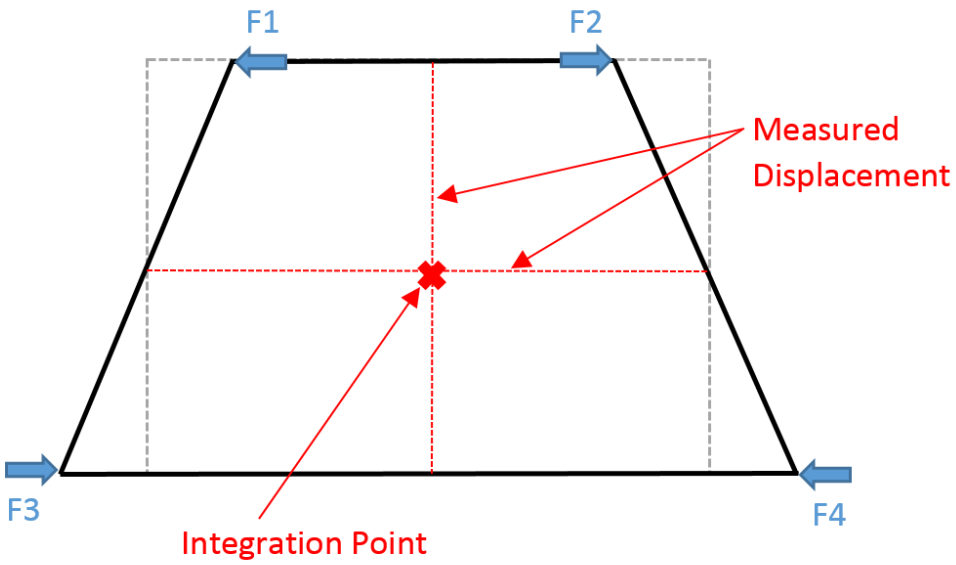

Figure 2-6: Hourglass mode and typical mitigation technique

LS-DYNA primarily utilizes two kinds of hourglass stabilization techniques: (1). a viscous control, which is best used in high velocity problems, and (2). stiffness control, which is best used in low velocity problems. The viscous control techniques generate hourglass forces proportional to the element's nodal velocities, while the stiffness control techniques generate forces proportional to the element's nodal displacements [Livemore, 2006]. Note that the viscous technique cannot mitigate hourglass deformation that has occurred on previous time steps of a simulation as it is based on a change in displacement rather than the displacement itself. In other words, if an element has undergone significant hourglass deformation at a previous point in the simulation but currently has nodal velocities of zero, the viscous technique will not introduce any correcting force into the simulation. However, the stiffness technique, when utilized in the same situation, would still work towards correcting for hourglass deformation as the form is based on nodal displacements and these nodal displacements indicate a need for hourglass control [Livemore, 2006].

These two kinds of hourglass stabilization techniques can be further subdivided into six different commonly used forms, as summarized in Table 2-1. Forms *IQH 1*, *IQH 2*, and *IQH 3* pertain to viscous-based techniques, while forms *IQH 4*, *IQH 5*, and *IQH 6* refer to stiffness-based techniques [DYNA-Manual, 2012]. These forms vary based on the means of force generation (i.e., viscous-based or stiffness-based), as well as the integration procedure used within the form. Forms *IHQ 1*, *IHQ 2*, and *IHQ 4* use a single-point quadrature method of integration, while forms *IHQ 3*, *IHQ 5*, and *IHQ 6* use exact volume integration. Table 2-1 also includes three additional forms, *IQH 7, IQH 9, and IQH 10*. While hourglass stabilization can play an important role in the material response of a numerical model, it is not possible for every parameter to be fully evaluated; therefore, this

thesis will focus on the more traditional hourglass stabilization forms (i.e. *IQH 1* through *IQH 6*).

Table 2-1: LS-DYNA hourglass stabilization forms

IQH	Description
1	Standard LS-DYNA viscous form
2	Flanagan-Belytschko viscous form
3	Flanagan-Belytschko viscous form with exact volume integration
4	Flanagan-Belytschko stiffness form
5	Flanagan-Belytschko stiffness form with exact volume integration
6	Belytschko-Binderman assumed strain co-rotational stiffness
7	Linear total strain form of type 6
9	Puso enhanced assumed strain stiffness
10	Cosserat Point Element

As presented in Section 2.1.1, a patch test was conducted on the six hourglass stabilization forms considered in this thesis (Figure 2-1 shows an exploded view of the element configuration of the test). The results of this patch test, presented in Table 2-2, provide an opportunity to assess the stability and consistency of these forms for use with general elements. As previously mentioned, hourglass stabilization forms within LS-DYNA include a combined force generation definition and an integration procedure definition. The results of the patch test study suggest that the single-point quadrature integration procedure is unable to correctly assess a state of uniform stress in a general hexahedron [Schwer et al., 2005]. Although initial element generation typically produces a uniform mesh where single-point quadrature integration procedures will accurately assess uniform stress fields, once the elements have undergone large deformations, there is greater potential for highly non-uniform element shapes. A failed patch test indicates that once these non-uniform shapes exist, error will begin to accumulate within the model [Schwer et. at., 2005].

Table 2-2: Patch test results for LS-DYNA hourglass stabilization forms

Hourglass Formulation	Integration Method	
	One-Point	Exact Volume
Standard LS-DYNA Viscous (Default)	IHQ 1[1]	N/A
Flanagan-Belyschko Viscous	IHQ 2[1]	IHQ 3
Flanagan-Belyschko Stiffness	IHQ 4[1]	IHQ 5
Belytschko-Binderman Assumed Strain Co-Rotational Stiffness	N/A	IHQ 6
Notes: 1 -Hourglass formulation failed the patch test		

Lastly, consideration should be given to the hourglass stabilization techniques used for previous validation of the LS-DYNA concrete models considered in this thesis. While these previous validation studies are largely focused on high velocity problems, information can still be collected regarding recommendations from previous researchers.

As previously mentioned, the KCC validation studies to this point have largely focused on blast and impact problems. As such, viscous hourglass controls have been widely used throughout their work [Crawford et. al., 2012, Wu et. al., 2012]. Validation on release three of the KCC material model, the version considered in this thesis, documents an hourglass control study using Forms *IQH 3* and *IQH 5* [Crawford et. al., 2012]. Validation of the Winfrith, CSC, and RHT models all indicate a viscous hourglass stabilization being used but neglect to explicitly provide the definition used.

This section is intended to present a background and overview of hourglass stabilization. Specific discussion addressing hourglassing as applied to the models presented in this thesis has been provided in Section 3.2.1 and 4.3.3. Section 4.3.3 also presents an hourglass study demonstrating the importance of hourglass control as applied to multi-element models.

2.2 Background On The Selected Material Models

While this thesis presents a user level validation of the various material models for a specific application, it is important to understand what these material models were originally developed to accomplish. Understanding the original application, and the differences between it and the problem being addressed in the current study, can provide insight into the anticipated strengths and weaknesses of material models for seismic applications. As such, this section of the of the thesis includes a brief history of the four selected material models, a summary of each material's plasticity model, an introduction to how each model considers damage, and a list of previous validation studies performed on each of the four models. The provided list of previous validation studies is not meant to be comprehensive. Rather, it is provided to demonstrate a focus on impact and blast validation in the past, as well as to establish a need for seismic validation if such an application is anticipated.

2.2.1 Mat 072R3 – Karagozian & Case Concrete (KCC) Model

The KCC model was originally developed in 1994 for applications involving blast loads. This model was implemented within DYNA3D, which is a non-commercial explicit finite element software originally developed for the U.S. Department of Energy [Magallanes, 2010]. A second release was made in 1996 to improve the model's capability to handle shear dilatancy and rate effects. This second release represents the basic form of the model used today [Magallanes, 2010]. In 1999, an automated variable generation scheme was added to improve the model's usability. Finally, in 2004 the model was ported from DYNA3D to LS-DYNA, marking a third release of the model. Subsequent updates to address bugs or add new features have been made, such as those detailed in [Magallanes, 2010]; however, the basic form of the model has remained consistent [Magallanes, 2010].

The KCC model is based on a three-surface plasticity model where the user, or automatic variable generator, is required to define a yield surface, a max surface, and a residual surface, as shown in Figure 2-7. Next, a definition of three softening parameters is required to define the unconfined uniaxial tension (UUT) and unconfined uniaxial compression (UUC) stress paths, as well as a volumetric expansion path. The plasticity variables are generated at every time step based on interpolation between the yield surface and max surface during hardening, or the max surface and residual surface during softening. This interpolation is based on a function using the model's damage parameter [Crawford et. al., 2012]. Note that in release three of the model, there is only a single damage parameter for the compression and tension stress paths. Finally, a series of elastic parameters, the bulk modulus, Poisson's ratio, and shear modulus are defined and used to calculate a trial deviatoric stress [Crawford et. al., 2012].

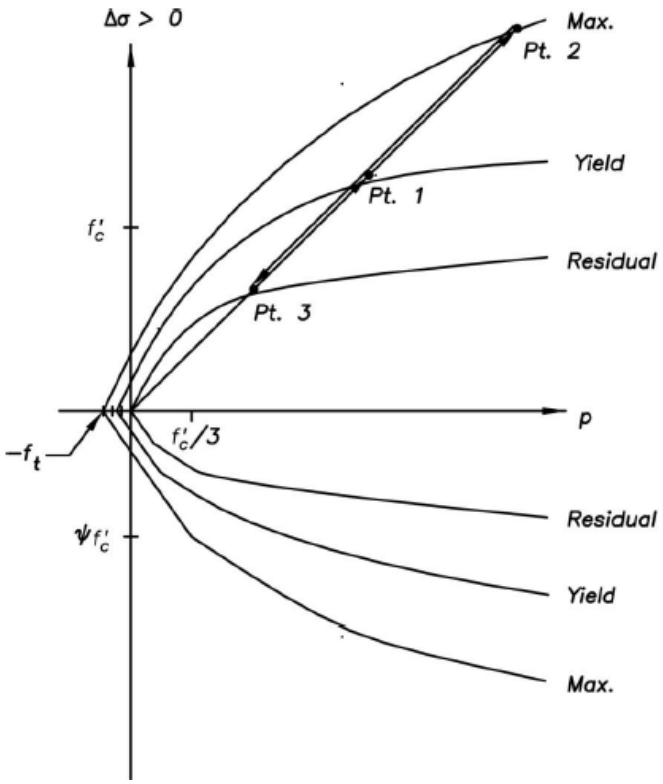

Figure 2-7: Illustration of the three defined surfaces used KCC model (pressure dependent) [Crawford et. al., 2012]

The automatic variable generation scheme is based on a comprehensive experimental testing program presented in Crawford et. al. [2012]. This program established a generalized fit based on a suite of concrete data and experimental testing designed to characterize each input variable. The result of the study was an automated scheme that could calculate the necessary 50 input variables based on the unconfined compressive strength of the concrete [Crawford et. al., 2012]. Note that the user can override specific automated variables, such as the variable used to signify the use of lightweight concrete, to further improve the automatic variable generation. Additional recommendations have been made regarding user input that will improve certain behaviors

of the concrete. Namely, this refers to manually specifying a $b1$ parameter (defined in Equation 2-1), based on the defined mesh size, to improve the exhibited shear dilatancy and softening behavior [Crawford et. al., 2012].

$$b1 = 0.34h + 0.79 \qquad \text{Equation 2-1}$$

where h is the maximum element edge dimension.

Previous validation efforts include:

- Unconfined uniaxial compression (UUC) – SE Test [Crawford et. al., 2012]
- Unconfined uniaxial tension (UUT) – SE Test [Crawford et. al., 2012]
- Triaxial compression (TXC) – SE Test [Crawford et. al., 2012]
- Triaxial compression test of a solid cylinder [Crawford et. al., 2012]
- Cylinder implosion test [Crawford et. al., 2012]
- Reinforced concrete column subjected to blast loads [Crawford et. al., 2012]
- Reinforced concrete slab subjected to impact loads [Crawford et. al., 2012]
- Quasi-static column confinement test [Crawford et. al., 2012]
- Quasi-static FRP column shear dilation test [Crawford et. al., 2012]

2.2 MAT 084 – WINFRITH CONCRETE MODEL

The Winfrith concrete model was developed in the 1980's as a means of modeling reinforced concrete structures subjected to impact loading. It was added into LS-DYNA in 1991 and has remained a popular tool for evaluating concrete's response to impact loading. It has also been shown to accurately model reinforced concrete subjected to blast loading [Shetye, 2013].

The Winfrith concrete model is based on the four-parameter Ottosen plasticity model, detailed in [Ottosen, 1977] and presented here:

$$Y\left(I_1, J_2, J_3\right) = aJ_2 + \lambda\sqrt{J_2} + bI_1 - 1 \qquad \text{Equation 2-2}$$

$$\lambda = \begin{cases} k_1 cos\left[\frac{1}{3}cos^{-1}(k_2 \cos(3\theta))\right] & cos(3\theta) \geq 0 \\ k_1 cos\left[\frac{\pi}{3} - \frac{1}{3}cos^{-1}(-k_2 \cos(3\theta))\right] & cos(3\theta) \leq 0 \end{cases} \qquad \text{Equation 2-3}$$

$$F_{in,\max} = \frac{d^2u}{dt^2}m = 0.791 \cdot A_{\max} = 180lbs$$

$$\cos(3\theta) = \frac{3\sqrt{3}}{2}\frac{J_3}{J_2^{\frac{3}{2}}} \qquad \text{Equation 2-4}$$

The four parameters of this model (a, b, $k1$, and $k2$) are determined from uniaxial tension, uniaxial compression, biaxial compression, and triaxial compression tests [Ottosen, 1977]. The model does not consider damage accumulation.

Additionally, the Winfrith model has the unique capability of crack mapping in the post-processing portion of the analysis [DYNA-Manual, 2012].

Previous validation efforts include:

- Unconfined uniaxial compression (UUC) – SE Test [Crawford et. al., 2012]
- Unconfined uniaxial tension (UUT) – SE Test [Crawford et. al., 2012]
- Triaxial compression (TXC) – SE Test [Crawford et. al., 2012]
- Triaxial compression test of a solid cylinder [Crawford et. al., 2012]
- Cylinder implosion test [Crawford et. al., 2012]
- Reinforced concrete column subjected to blast loads [Crawford et. al., 2012]
- Reinforced concrete slab subjected to impact loads [Crawford et. al., 2012]
- Quasi-static column confinement test [Crawford et. al., 2012]
- Quasi-static FRP column shear dilation test [Crawford et. al., 2012]

- Reinforced concrete panel subjected to blast loading [Tanapornraweeki et. al., 2007]

2.2 MAT 159 – CONTINUOUS SURFACE CAP MODEL

The CSC model was developed in the 1990s as part of a project intended to improve safety associated with road side impact. The model was added into LS-DYNA in 2004 in large part due to sponsorship provided by the U.S. Department of Transportation (DOT).

The continuous surface cap model refers to a "cap" plasticity model with a smooth, or continuous transition between the failure surface, or shear surface, and the cap surface, as shown in Figure 2-8 [Murray, 2004]. The concrete's strength is governed by the shear surface in tensile and low-pressure regimes, the cap surface in high-pressure regimes, and a combination of the shear surface and cap surface in moderate-pressure regimes. The continuous transition between the two surfaces prevents numerical instability introduced by using a discrete transition point [Murray, 2007]. An illustration of sample stress paths taken to failure are provided in Figure 2-9.

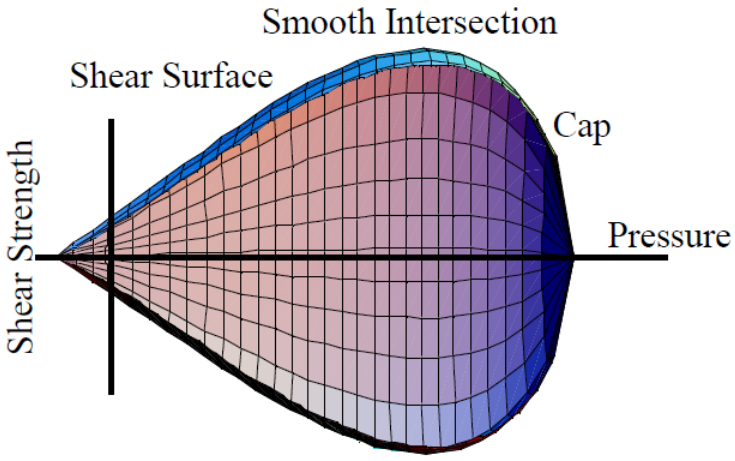

Figure 2-8: Two-dimensional view the CSC's failure and hardening surfaces – plotted on the deviatoric stress plane [Murray, 2004]

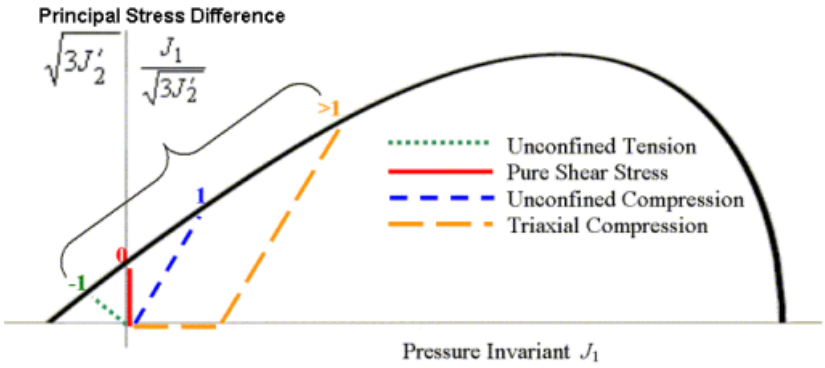

Figure 2-9: Illustration of stress paths and their stress invariant ratios [Murray, 2007]

Similarly to the plasticity models described previously in this chapter, the CSC model is in essence an elastic-plastic model; however, it uses a damage function that allows the model to capture softening in low-to moderate-pressure regimes. The damage function considers both softening and modulus reduction based on a damage parameter, shown in Figure 2-10. This damage parameter allows the material model to capture slope reduction in cyclic loading scenarios [Murray, 2007]. The damage formulation given by Eq. 5 considers both brittle damage (Equation 2-6) and ductile damage (Equation 2-7). Brittle damage is defined as damage accumulated in a tensile pressure regime, whereas ductile damage is defined as damage accumulated in a compression pressure regime [Murray, 2007].

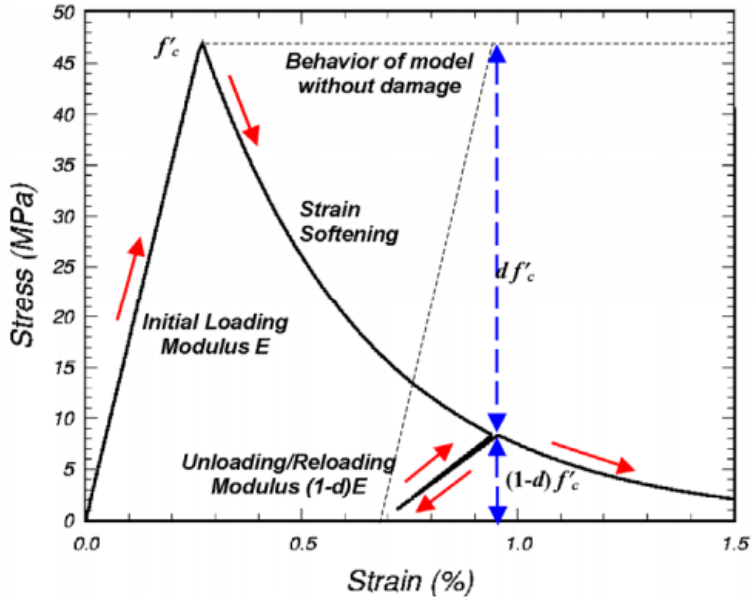

Figure 2-10: CSC damage incorporation

$$\sigma_{ij}^{d} = (1-d)\sigma_{ij}^{vp} \qquad \text{Equation 2-5}$$

$$\sigma_{ij}^{d} = (1-d)\sigma_{ij}^{vp}$$

where σ_{ij}^{d} is the stress tensor with damage, σ_{ij}^{vp} is the stress tensor without damage, and d is a damage parameter. Damage parameters are given by Eqs. 6 and 7 [Murray, 2007].

$$d(\tau_{brittle}) = \frac{0.999}{D}\left[\frac{1+D}{1+Dexp^{-C(\tau_{brittle}-r_{0b})}}-1\right] \qquad \text{Equation 2-6}$$

$$d(\tau_{ductile}) = \frac{d_{max}}{B}\left[\frac{1+B}{1+Bexp^{-A(\tau_{ductile}-r_{0d})}}-1\right] \qquad \text{Equation 2-7}$$

where A, B, C, and D are softening parameters, r_{0b} and r_{0d} are damage threshold parameters, d_{max} is a maximum attainable damage parameter, and $\tau_{brittle}$ and $\tau_{brittle}$ are damage levels calculated as functions of stress and strain [Murray, 2007].

Additional definitions, illustrations, and discussion can be found within [Murray, 2007].

Previous validation efforts include:

- Unconfined uniaxial compression (UUC) – SE Test [Crawford et. al., 2012, Murray, 2004]
- Unconfined uniaxial tension (UUT) – SE Test [Crawford et. al., 2012, Murray, 2004]
- Triaxial compression (TXC) – SE Test [Crawford et. al., 2012]
- Pure shear SE Test [Murray, 2004]
- Cyclic loading SE Test [Murray, 2004]
- Triaxial compression test of a cylinder [Crawford et. al., 2012]
- Unconfined compression test of a cylinder [Murray, 2004]
- Unconfined tension test of a cylinder [Murray, 2004]
- Cylinder implosion test [Crawford et. al., 2012]
- Reinforced concrete column subjected to blast loads [Crawford et. al., 2012]
- Reinforced concrete slab subjected to impact loads [Crawford et. al., 2012]
- Reinforced concrete beam drop tower test [Murray, 2004]
- Vehicle impact simulation [Murray, 2004]
- Quasi-static column confinement test [Crawford et. al., 2012]
- Quasi-static FRP column shear dilation test [Crawford et. al., 2012]

2.2 MAT 272 – RHT MODEL

The RHT model was developed to complement pre-existing impact and blast focused concrete models with specific consideration for porous compaction [Riedel et. al., 2011]. Porous compaction, along with micro-cracking and cell wall buckling, is considered

to significantly contribute to concrete's nonlinearity. This model was developed to capture some of this nonlinearity in a way only few models had previously attempted [Riedel et. al., 2011].

The RHT model is based on a plasticity model that defines three pressure-dependent surfaces: (1). a yield surface, (2). a failure surface, and (3). a residual surface. These surfaces are shown in Figure 2-11. Pressure dependence is defined using the Mie-Gruneisen equation of state [Riedel et. al., 2011]. Specific discussion regarding this particular equation of state is not considered within the scope of this thesis. Readers should consult the before mentioned reference for further description of the equation of state. A cap is also defined based on a porous crushing pressure. Damage evolution in this model is governed by plastic strain and represented by interpolation between the failure surface and residual surface. Fully damaged material is considered to have strength if still supported by a confining pressure [Riedel et. al., 2011].

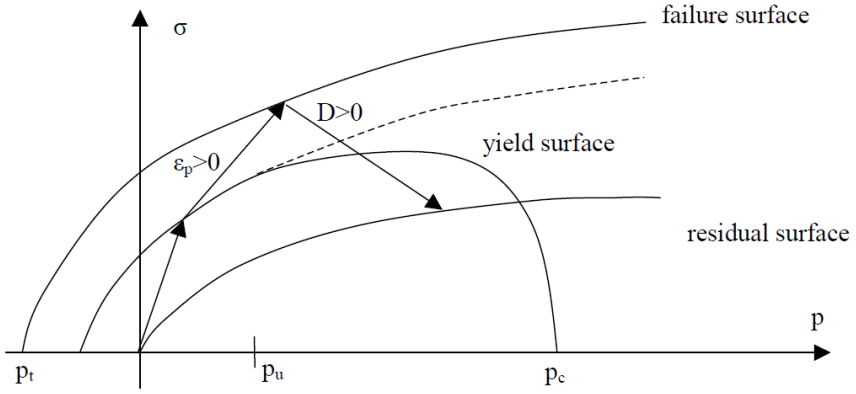

Figure 2-11: RHT three surface plasticity model

Previous validation efforts include:

- Unconfined uniaxial compression (UUC) – SE Test [Crawford et. al., 2012]

- Unconfined uniaxial tension (UUT) – SE Test [Crawford et. al., 2012]
- Triaxial compression (TXC) – SE Test [Crawford et. al., 2012]
- Triaxial compression test of a solid cylinder [Crawford et. al., 2012]
- Cylinder implosion test [Crawford et. al., 2012]
- Reinforced concrete column subjected to blast load [Crawford et. al., 2012]
- Reinforced concrete slab subjected to impact load [Crawford et. al., 2012]
- Quasi-static column confinement test [Crawford et. al., 2012]
- Quasi-static FRP column shear dilation test [Crawford et. al., 2012]

2.3 PREVIOUS SEISMIC AND CONCRETE VALIDATION STUDIES

Prior to conducting a new validation study, it is important to understand the components of previously conducted validation studies. Of particular interest to this thesis are seismic validation studies and other extensive validation programs performed on various LS-DYNA concrete models. This section first presents a seismic validation study and details its validation process. Next, the validation process for two of the four selected LS-DYNA material models is described. Although this second set of studies may focus on a different application (i.e. performance when subjected to blast and impact loadings), the process can be generalized and adapted to a new application such as seismic analysis.

In 2006 and 2007, the University of California embarked on a two-year study to validate the use of finite element software for nonlinear simulations of structural response under seismic loads [Alves, 2006, Alves, 2007]. The goal of the project was to numerically replicate a series of shake table tests conducted on a full-scale seven-story reinforced-concrete structure. This goal can be divided into two sub-goals, namely, the validation of a concrete material model and homogenized rebar and the validation of a full-scale structural system subjected to a seismic loading [Alves, 2006, Alves, 2007]. Figure 2-12

shows the full-scale 7-story test structure subjected to seismic loads by means of the Network for Earthquake Engineering and Simulation Large High-Performance Outdoor Shake Table at the Engelkirk Structural Engineering Center of UCSD and Figure 2-13 shows a rending of the finite element full-scale structural system used in the validation effort.

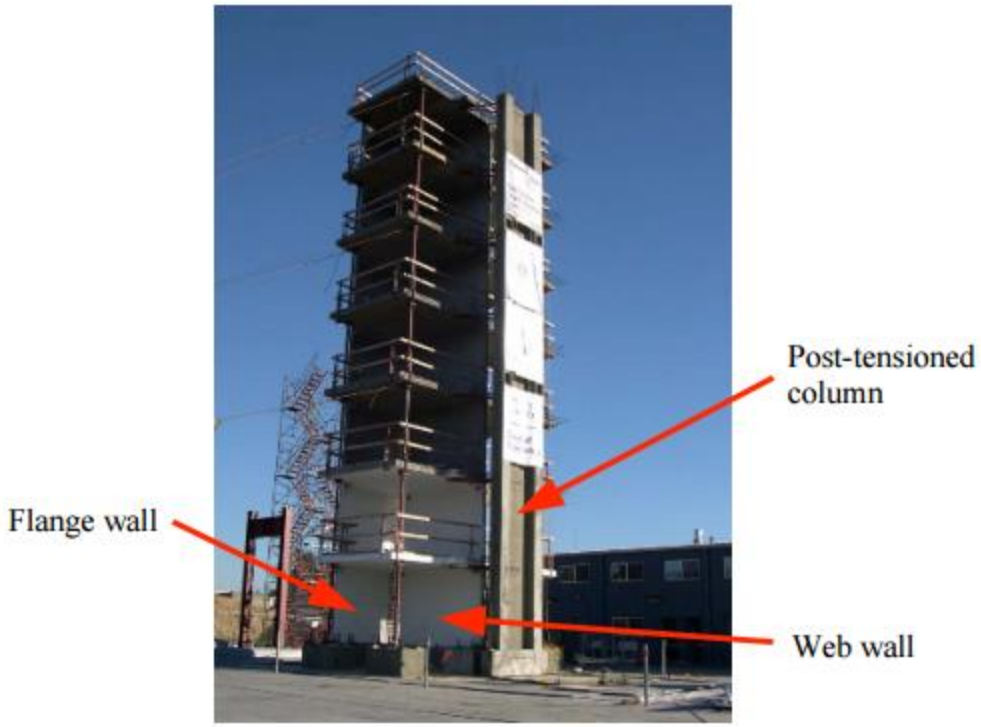

Figure 2-12: Full-scale 7 story test structure [Alves, 2007]

Figure 2-13: Finite-element model used for the Alves validation study [Alves, 2007]

The validation procedure was conducted with the before-mentioned sub-goals in mind. First, a full-scale linear model was constructed and run in DYNA3D, and the results were compared to the full-scale physical test results. It was found that the linear model oscillated with much higher frequencies, in comparison to the results obtained from the experimental study. This outcome was expected because a linear model is not capable of capturing the damage that occurs in the physical systems. Next, a nonlinear model was constructed using *MAT 45*, a previous release of the KCC model, and homogenized rebar [Alves, 2006].

This initial analysis yielded three different problems. First, a time consuming nonlinear simulation could not be completed due to a numerical instability. It was

hypothesized that this instability came about from a singularity in the concrete material model, leading to excessively large local deformations and element inversions [Alves, 2006]. Second, spurious oscillations were seen in the results when *MAT 65*, an updated version of *MAT 45*, was used. It was hypothesized that these oscillations were a result of numerical ill-conditioning and the problem was mitigated by using the older version of the material model. Lastly, the new element architecture could not support the stress initialization feature used to simulate the four different earthquake motions run on the model. This limitation was fixed by using the old element architecture [Alves, 2006]. Two additional cases were run that considered no homogenized rebar (i.e., a pure concrete model) and homogenized rebar in a weaker concrete. To the surprise of the researchers, these two additional models ran with no singularity problems [Alves, 2006]. Later investigations showed that this original instability, encountered in the run using the stronger concrete, was caused by very small effective strain and damage parameter increments. A fix, already included in the newer version of the material model (*MAT 65*), was implemented in *MAT 45*. Additional fixes were also implemented as discussed in [Alves, 2007].

An additional round of linear and nonlinear simulations led to additional conclusions. Although the instability in the material model was fixed, another anomaly was present that could result in larger than expected deformations. It was recommended that users take care in interpreting results. Additionally, the model was significantly more sensitive to the defined concrete properties as compared to the rebar properties. Boundary conditions, as expected, played a very important role in the predicted behavior. The final conclusion drawn from the study was that the material model seemed to accurately assess the onset of structural damage seen from seismic loading, but, at the time of this study, could not be relied upon for long-running seismic simulations [Alves, 2007].

This previous example presents a multi-element evaluation. While useful, it provides the user with only a rough idea of how the material model is actually behaving. The next two examples involving validation of the KCC material model and validation of the CSC material model, present both a single-element validation and multi-element validation of reinforced concrete subjected to impact and blast loads.

Validation of the KCC material model is presented in detail in [Crawford et. al, 2012]. The validation process began by defining key inherent assumptions made regarding keyword definitions. This work included discussion on strain rate enhancement, a default material fit, and several other terms. With the variables defined, analysis was performed on a series of single-element tests designed to take the concrete model through various basic stress paths (e.g., unconfined compression, unconfined tension, triaxial compression, and others). The single-element portion of the validation also included a series of smaller studies testing the sensitivity of the model's behavior to variables and parameters such as hourglass control and $b1$. Next, a series of multi-element tests were conducted to mimic the actual response of material subjected to blast and impact loading. An additional series of these tests was made to validate quasi-static behavior of various structural components. Finally, conclusions were drawn relating the results of the entire investigation [Crawford et. al, 2012].

Validation of the CSC model was conducted in a similar way. Initial assumptions were stated in a technical chapter. A variety single-element models were run to verify the various surfaces of the model and damage accumulation were working as designed. Next, two quasi-static simulations were run on multiple concrete cylinders. The failure mechanisms seen in these quasi-static scenarios were compared to failure mechanisms seen in experimental testing. Next, the model was validated for impact loading using a multiple

element drop tower test, and the final validation considered a vehicle impact simulation test [Murray, 2004].

2.4 Literature Review Closing Remarks

This Chapter has presented a background on several of the various parameters included within a typical finite element model including boundary conditions, strain-rate effects, element formulation, and hourglass stabilization. Additionally, it has presented a brief history of the four material models considered in this thesis as well as a description of the formulations adopted by each material model. Finally, it has provided a few examples of previously conducted seismic and material model validation efforts. The objective of this Chapter has been to establish context for the forthcoming analysis exercises presented in Chapters 3 and 4. The validation methodology used in this thesis, a combination of single-element and multi-element tests, has been drawn from the KCC validation study presented in Section 2.3 and the validation studies presented in this thesis will lean on the background theory presented in Sections 2.1 and 2.2. With this context established, Chapter 3 will begin the validation study portion of this thesis.

Chapter 3: Single Element Analysis and Evaluation

3.1 An Introduction To The Single-Element Validation Phase

As discussed in Section 2.3, numerical model validation typically includes a review of pertinent technical background information, discussion of definitions, a series of single-element validations, and a series of multi-element validations. The technical background for this thesis is provided in Chapter 2. The following chapter presents a collection of single-element validation studies designed to take the LS-DYNA material models *MAT 72R3*, *MAT 84*, *MAT 159*, and *MAT 272* through a series of basic stress paths. Single-element models provide a convenient way to assess a material model's output while limiting uncertainty introduced by complicated geometries. The boundary conditions and load application can be defined in such a way that an individual element is loaded in a state of unconfined compression, unconfined tension, or some other convenient stress path, and the element is not subjected to interaction from other elements.

The single-element study presented in this thesis has been divided into three parts: (1). monotonic compression, (2). indirect shear, and (3). cyclic loading. Each subsection of the single-element validation chapter takes the various material models through strategically designed load paths that may be encountered during seismic loading and is used identify the trends various material definitions have on the model's computed response. The primary objective of this chapter is to identify, in an isolated environment, the strengths and weakness associated with each material model when tasked with capturing concrete's behavior under seismic loading. The objective of Chapter 4, which focuses on material system validation, is to understand the system level repercussions of each identified strength and weakness.

Note that if strengths and weaknesses are to be identified, there must also be some "correct" reference to which each behavior can be compared. Results from single-element

models can be directly compared to pre-existing experimental data as well as pre-established theoretical models. Because single-element models take material models through idealized loading scenarios, previously developed theoretical models describing the "correct" response to such idealized loading scenarios offer convenient reference points. Further discussion regarding each reference model or experimental data will be provided in its respective section.

To this point the specifics of the material definitions themselves have not been directly addressed. Clearly, however, it is important to discuss these definitions prior to presenting any results. Note that the four material models selected for consideration in this thesis were chosen because of their suitability to represent concrete under cyclic loads and their popularity among users.

Specific variable definitions, required within each material's keycards, have been largely defined using the automated parameter generation scheme provided by each of the material definitions. This choice has been made for two reasons. First, the large number of variable definitions required to manually define each model can be cumbersome for most users. For instance, the KCC material model has 50 variable definition options, the Winfrith material Model has 36 variable definition options, the CSC material model has 12 variable definition options, and the RHT model has 37 variable definition options [DYNA-Manual, 2012]. It is beyond the scope of this thesis to analyze each material model's performance associated with a unique idealization of variable inputs. Second, the goal of this work is to provide the general user with an evaluation of the most commonly utilized concrete models under seismic loads. It can be reasonably assumed that the typical user relies upon default parameter generation for a majority of their material definitions. This assumption is reasonable because the majority of additional variables require outside testing for proper specification. As such, the evaluation presented in this thesis will make

a similar assumption and. will be performed using a typical user's input. Note that this "typical" input is dependent on the material model being defined.

The KCC model requires the definition of mass density, unconfined compressive strength, and two separate unit conversion inputs. Although not required, Poisson's ratio, *b1* (as presented in Equation 2-1), and the maximum aggregate size can also be defined to improve the automated variable generation. Note that an equation of state must be linked to the KCC model for proper behavior. Tabulated compaction is recommended for the equation of state requirement.

The Winfrith model requires values for the mass density, unconfined compressive strength, tangent modulus, Poisson's ratio, fracture energy, rate effects, and three separate unit conversion inputs. Although more complicated than the KCC inputs, the Winfrith model still only requires a typical user to input basic material information.

The CSC model requires the definition of a mass density, unconfined compressive strength, aggregate size, and a unit conversion input. It also provides various options for plotting, strain rate, recovery, cap retraction, and pre-existing damage. This model contains perhaps the simplest definition options.

Finally, the RHT model requires inputs for mass density, compressive strength, and a unit conversion. Note that the RHT model relies on pressure dependence defined by the Mie-Gruneisen equation of state (introduced in Section 2.2.3). While this equation of state can be manually defined, this thesis relies upon the default definition generated by the automatic parameter generation scheme included within the model.

To directly compare the different material models with each another and to theoretical material models, a fixed set of material properties, shown in Table 3-1, has been used to define the required variables in the keycards for each of the four material models. These input parameters were selected from a previous validation study conducted by

Crawford et al. [2012] because they represent a well-tested and well-documented concrete material. Selecting such a material was done to provide flexibility for a fluid transition into future research where additional properties may be manually defined.

Table 3-1: Single element material data

f'_c	Mass Density (lbf-s^2 / in4)	Poisson's Ratio	Max Agg Size (in)	Tangent Modulus (psi)
6580	2.25E-04	0.15	8-Mar	4.62E+06

3.2 MONOTONIC COMPRESSION – A PARAMETER STUDY

As previously discussed, the response of a finite element model is sensitive to several parameters outside of the material model including: boundary conditions, element size, strain-rate effects, element formulation, and hourglass stabilization. Because it is the aggregated parameter response that drives the behavior, rather than the material model alone, it is critical to understand how each definition of the additional parameters impacts a numerical model's computed response.

An effective way to identify the relationship between the input variables and the computed response is through a parametric study. In the case of numerical models, parametric studies consist of a series of nearly identical models with only the parameter in question being changed. Prior to conducting a parametric study, it is important to establish three things: (1). identify the parameters of interest, (2). establish dimensions for the parameters of interest, and (3). select the appropriate test set up for conducting the study. This thesis has identified the five parameters listed in the first paragraph of Section 3.2 as the parameters of interest.

Dimensionalizing parameters simply refers to establishing research boundaries for the parameters of interest. For instance, when testing element size, it would be impractical

to test 20 or 30 different element sizes. Limits must be established to efficiently and effectively test the parameter of interest within the scope of the study. Section 2.1 of this thesis provided background on the parameters of interest in this study. This information was presented not only to provide the reader with a background to the technical components of the thesis, but also to help dimensionalize the parameters of interest. Specific dimensions of the various parameters of interest are provided within their respective subsection (i.e. Sections 3.2.1, 3.2.2, and 3.2.3).

A monotonic compression test was selected as the best means of conducting the parametric study because it represents the simplest concrete loading case available, and the results can be directly compared to verified theoretical models. Because there are so many variables that go into developing even a basic model, it's important to establish each parameter's effect on the simplest material test prior to expanding to more complicated loading or a multi-element system.

Although boundary conditions have been listed as a key parameter of the study, Method One, (explicitly applied restraints on each node of the element as defined in Section 2.1.1) will be used as the sole method used in this thesis for restraining single-elements. While Method Two (the symmetry-plane method, again as defined in Section 2.1.1) conveniently ensures element stability, such a model represents an idealized case. When considering a general element within a multiple-element system, there is no assurance that the element's nodes will deform symmetrically. Therefore, Method One allows for a more generalized case of boundary conditions compared to the second approach.

The Thorenfeldt constitutive model, presented in (Equation 3-1), was selected a means of comparison for the monotonic compression analyses presented in this thesis:

$$f_c = f_p \frac{\varepsilon}{\varepsilon_p} \frac{n}{n-1+\left(\frac{\varepsilon}{\varepsilon_p}\right)^{nk}} \qquad \text{Equation 3-1}$$

where f_p is the peak compressive stress (defined in MPa), ε_p is the corresponding strain, and n and k, are decay constants defined by

$$n = 0.8 + \frac{f_p}{17} \qquad \text{Equation 3-2}$$

$k = 1$, for the ascending branch Equation 3-3

$k = 0.67 + \frac{f_p}{62}$, for the descending branch Equation 3-4

and f_p is defined in MPa.

This particular constitutive model is widely accepted for its ability to capture both pre-peak and post-peak behavior of concrete under uniaxial compression [Thorenfeldt, 1987]. Therefore, it is an ideal candidate for comparison purposes. The response predicted by this model is overlaid with the numerically generated results to show the results compare. Note that default values for the decay constants "*n*" and "*k*" have been selected based on recommendations provided by Thorenfeldt [1987].

3.2.1 ELEMENT FORMULATION AND HOURGLASS CONTROL

The first parametric test considered is the element formulation and hourglass control test. These first two parameters are presented together because element formulation and hourglass control are interrelated (i.e., reduced integration typically requires an hourglass control to prevent zero-energy deformation modes from occurring).

As discussed in Section 2.1.3, the most common element formulations used are *ELFORM 1* (the reduced integration formulation) and *ELFORM 2* (the full integration formulation) [Schwer et. al., 2005]. Also introduced in Section 2.1.3 were two additional

formulations, *ELFORM -1* and *ELFORM -2*, presented as options to mitigate a transverse shear locking problem documented with *ELFORM 2* [Livermore, 2012]. Although these additional formulations have been shown to effectively mitigate shear locking in simulations dominated by transverse shear and poor aspect ratios, the frequency of this combination is not enough to warrant consideration of these elements for this initial validation. As such, *ELFORM 1* and *ELFORM 2* will be the only cases considered in the element formulation component of the study.

Section 2.1.4 introduced six different hourglass forms comprised of two different hourglass control techniques and two different integration procedures, as shown in Table 2-2. Because seismic application can span a wide range of loading rates, as demonstrated in Figure 2-3, consideration for both stiffness-based and viscous-based hourglass control is appropriate. Regarding the integration procedure, Schwer et. al. [2005] demonstrated that a single-point quadrature integration procedure is unable to correctly assess a state of uniform stress in a general hexahedron. Because the goal of this thesis is to validate seismic loading for a general element, forms that utilize single-point quadrature integration procedures will not be considered in this thesis. This restriction leaves *IHQ 3*, *IHQ 5*, and *IHQ 6* as potential variable options. *IHQ 3*, Flanagan-Belytschko viscous form with exact volume integration, and *IHQ 5*, Flanagan-Belytschko stiffness form with exact volume integration, have been selected as the best choices for this study as they represent both stiffness and viscous techniques using the same Flanagan-Belytschko formulation.

Although selecting the integration procedure is a majority of the hourglass control definition, additional variables must still be defined. These additional variables are relatively sensitive to the model under consideration and often require considerable experience and fine tuning to properly define. To simplify this process and to ensure a

properly behaving stabilization, this thesis will use a set of definitions, presented in Table 2-3, that have been used for a previous single-element study [Crawford et. al., 2012].

Sections 3.2.2 and 3.2.3 detail investigations conducted on the element size and applied strain rate, respectively. Each sub-study will vary the two parameters over a dimensionalized spectrum; however, the element formulation and hourglass control study requires a single size and strain rate to be defined. The selected element size is 4-inches by 4-inches by 4-inches, and the selected strain rate is 0.01/sec. These two values fall within the dimensionalized spectrum considered in Sections 3.2.2 and 3.2.3, respectively, and will serve as controls for the element formulation and hourglass control study.

Figure 3-1 illustrates the typical set up for the element formulation and hourglass control study. The test consists of a single cube, supported from the bottom by a pinned boundary condition at one corner and roller boundary conditions at the remaining three corners. Note that the rollers allow for unrestricted out-of-plane expansion and prevent confinement from developing within the element. A displacement-controlled procedure was selected for the test so that post-peak behavior could be captured. An identical prescribed displacement was applied at each of the top four corners using the linear time versus displacement curve. A strain rate of 0.01/sec was used for all tests to provide consistency in loading rate. Note that this load rate is not expected to produce substantial dynamic increase factors; thus, strain rate options were not included.

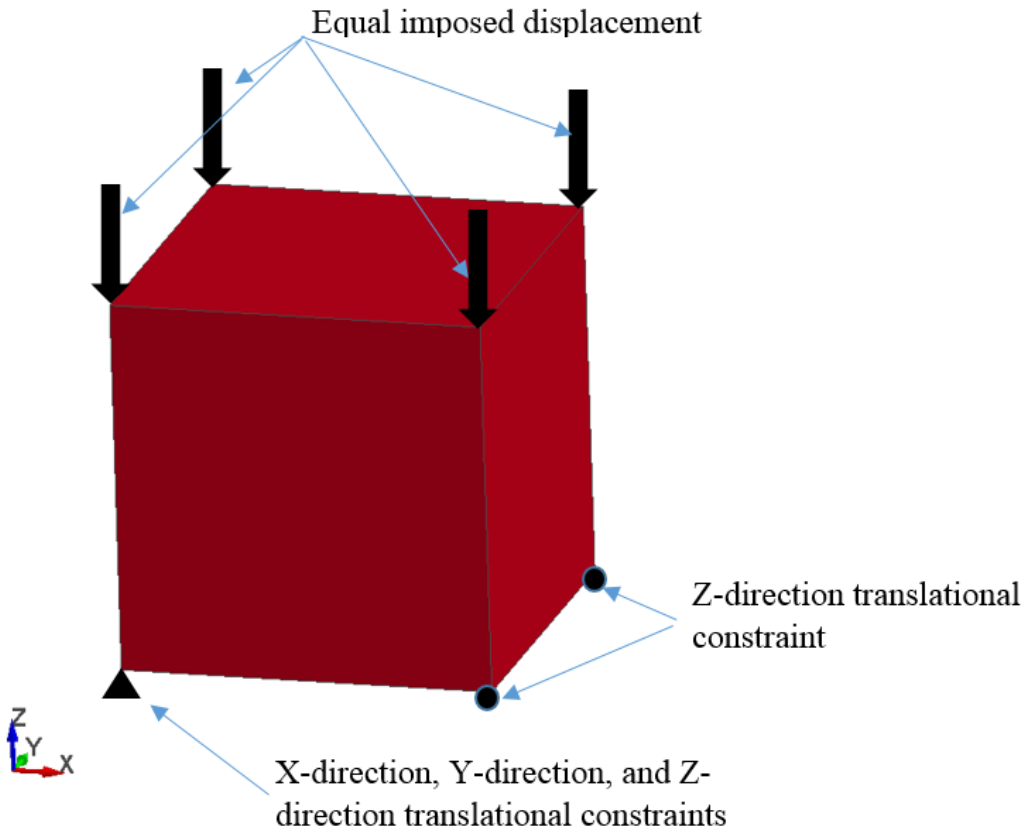

Figure 3-1: Element formulation (EF) & hourglass control (HG) -Monotonic compression test

Figure 3-2 shows the monotonic compression results from the KCC material model defined with *ELFORM 1*, configured with stiffness and viscous hourglass control, and *ELFORM 2*. Viscous hourglass control and stiffness hourglass control have been abbreviated as VHG and SHG, respectively, for the purpose of labeling figures. The KCC model consistently predicts monotonic compression response for a single element regardless of the selected element formulation and hourglass control. The generated behavior also seems to closely align with that predicted by the Thorenfeldt model. The peak capacity and corresponding strain at peak capacity are identical between the numerically generated results and theoretical model. Pre-peak behavior also appears to

agree. The post-peak behavior predicted by the two models shows minor inconsistencies. The Thorenfeldt model uses a curve containing double curvature while the post-peak shape of the KCC model more closely resembles that of a parabola. Regardless of this difference in shape, response up to a strain of 0.0027 still remains fairly consistent. Beyond this strain, the capacity of concrete is often inconsistent; therefore, the disagreement in shape is not of significant concern. Overall, the KCC model appears to adequately capture monotonic compression in a single element regardless of the specified element formulation and hourglass control definition.

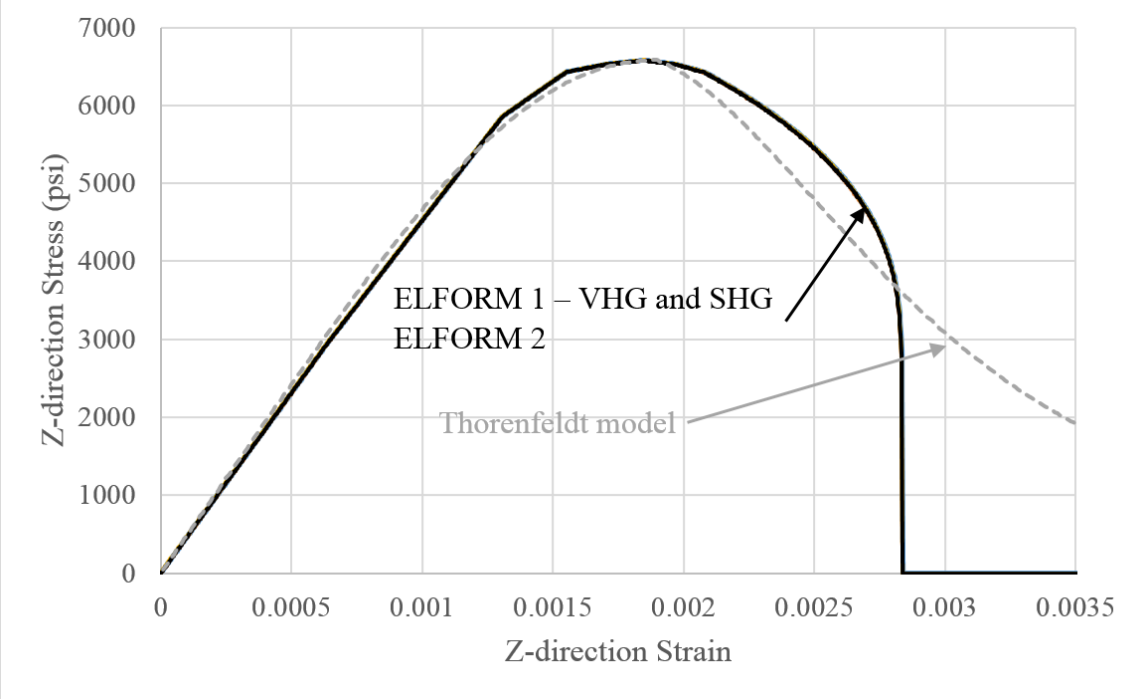

Figure 3-2: KCC model – EF&HC – Monotonic compression results

Figure 3-3 shows the monotonic compression results of the hourglass and element formulation study using the Winfrith model. As observed with the KCC model, the element formulation and selected hourglass control do not appear to have any influence on the exhibited behavior of a single element subjected to monotonic compression. Unlike the KCC model, however, the results generated with the Winfrith model show poor agreement

with the Thorenfeldt solution. The Winfrith model shows elastic behavior up until peak capacity, occurring at a strain of approximately 0.0014, and then plastic behavior until a specified failure strain. The elastic-plastic representation overestimates initial stiffness and then ignores post-peak softening, which is an important component of concrete's behavior, especially when considering damage accumulation under cyclic loading.

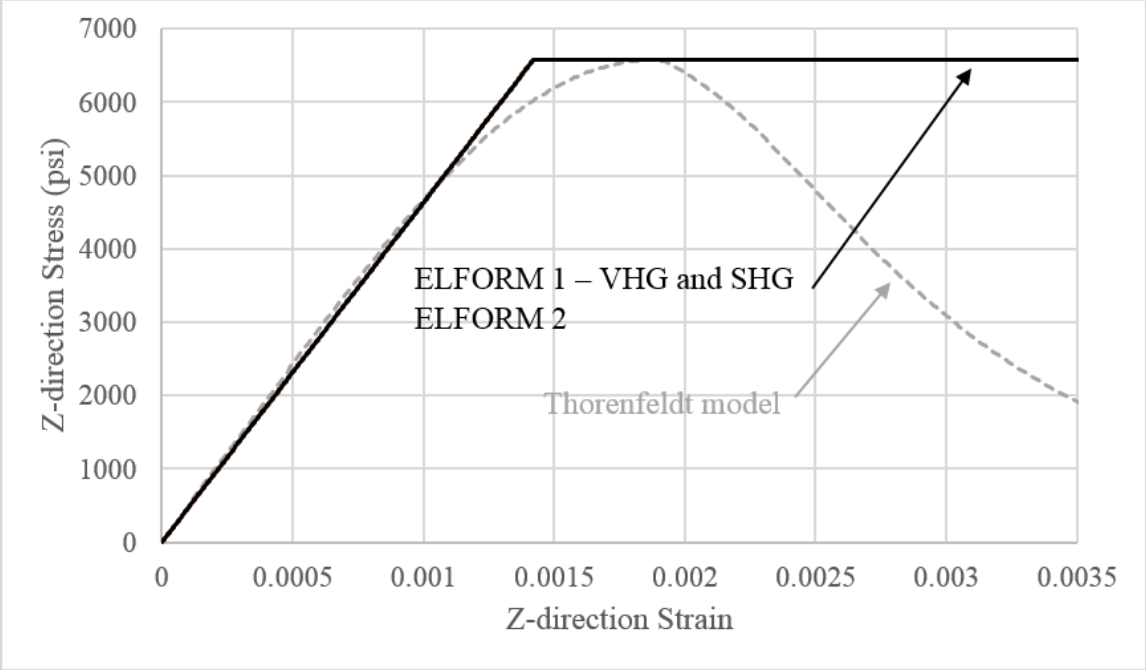

Figure 3-3: Winfrith model – EF&HC – Monotonic compression results

Figure 3-4 shoes the monotonic compression results of the hourglass and element formulation study using the Continuous Surface Cap model. The model shows elastic behavior up to the peak capacity and then shows a varying post-peak softening response based on the selected element formulation. *ELFORM 1*, regardless of hourglass control, exhibits behavior similar to that predicted by Thorenfeldt's model. *ELFORM 2* exhibits a steeper initial softening curve, which then degrades to produce a relatively small magnitude of softening at higher strains. The pre-peak stiffness of the two models is in general

agreement; however, it should be noted that peak capacity of the CSC model occurs at a strain of approximately 0.0015 compared the 0.002 predicted by the Thorenfeldt model. The impact of this 20% difference on a multiple element model will be discussed in Chapter 4. Overall, the CSC model appears to adequately capture monotonic compression in a single element regardless of the specified element formulation and hourglass control definition.

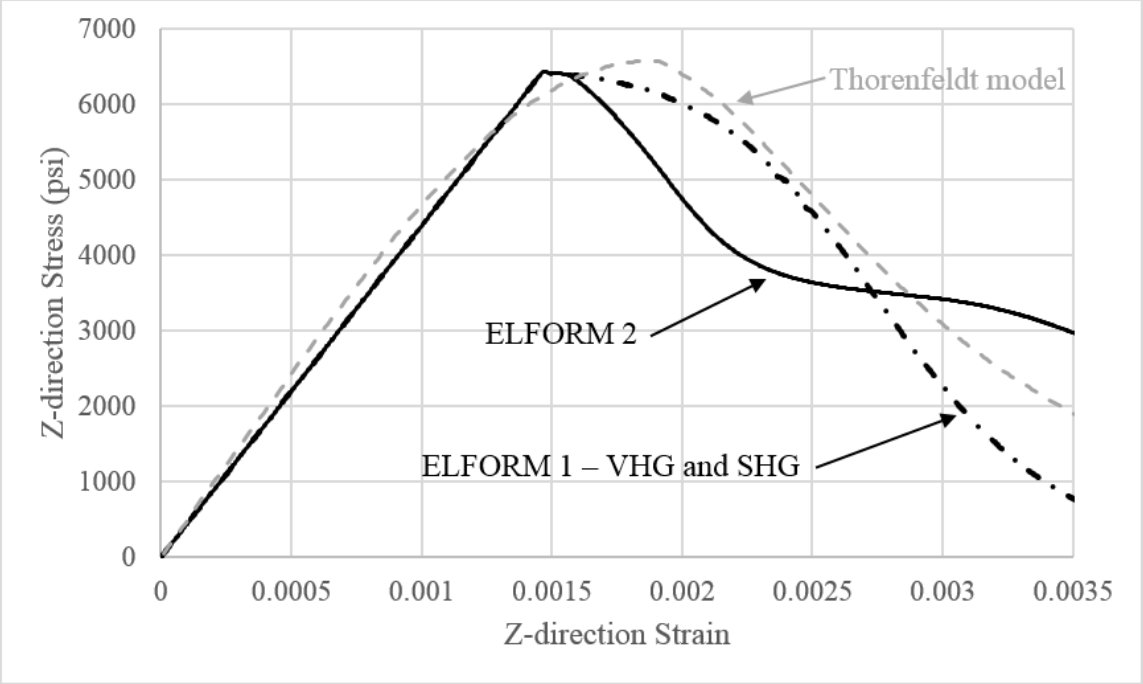

Figure 3-4: CSC model – EF&HC – Monotonic compression results

Figure 3-5 shows the monotonic compression results of the hourglass and element formulation study using the RHT model. This model is considerably more sensitive to the selected element formulation and specified hourglass control than the other material models considered in this study. It appears that the RHT material model does not support

ELFORM 2 and requires a viscous hourglass control definition. Note that the RHT model over-predicts the user-defined concrete capacity. Figure 3-5 shows a numerically predicted maximum capacity that is nearly 18% greater than the specified value. Users should consider this tendency to over-predict strength when using this model. Another noteworthy characteristic of the response is the bi-linear pre-peak behavior. This behavior only roughly approximates concrete's physical behavior. Additionally, the post-peak behavior shows a slow softening response as compared to Thorenfeldt's model.

The combination of slow linear softening, over-prediction of strength, and over-prediction of corresponding peak capacity strain is concerning and can lead to gross over-prediction of concrete capacity at high levels of compressive strain. For example, at a strain of 0.0035, the Thorenfeldt model predicts a capacity of approximately $0.24f'_c$ while the RHT model yields a capacity of roughly $1.09f'_c$. This demonstrates that the RHT model maintains capacities higher than the manually specified strengths at strains well beyond that of crushing.

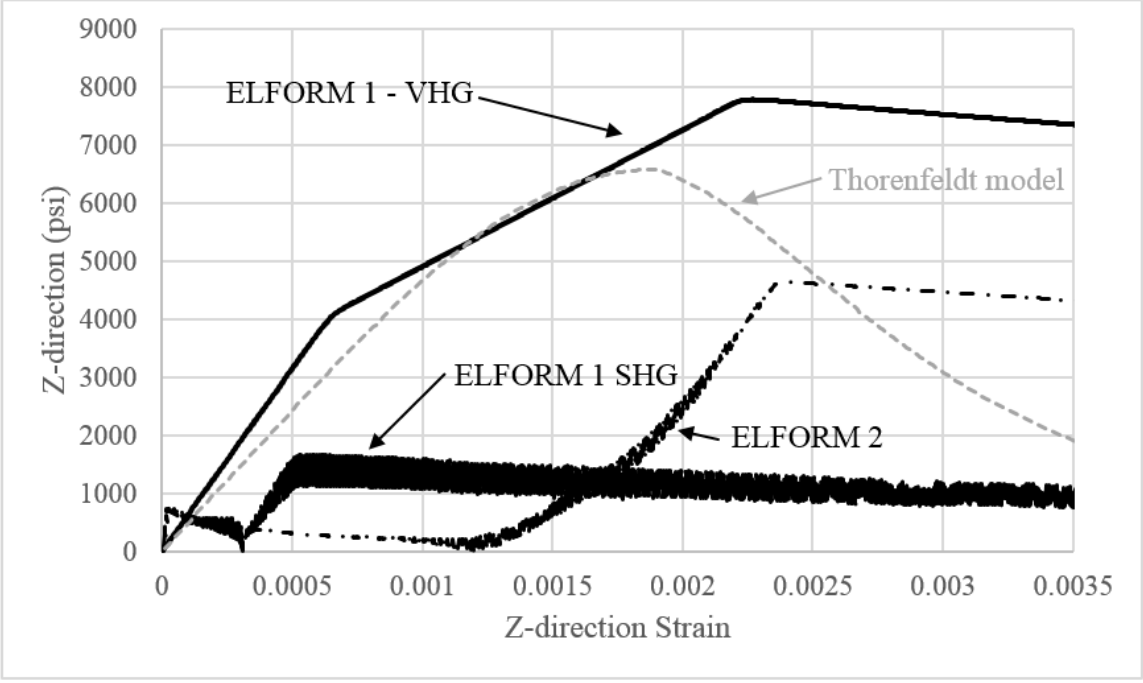

Figure 3-5: RHT model – EF&HC – Monotonic compression results

The element formulation and hourglass control study demonstrates several things. First, the CSC and RHT models are both sensitive to the selected element formulation and hourglass control definitions. While the CSC model appears to behave well regardless of definition choice, users should be aware that the fundamental behavior of concrete in unconfined compression can be altered by simply changing the element formulation option. Future single-element studies should also consider this relation and document the specific definitions they use. The RHT model is significantly more sensitive to the different element formulation and hourglass control options than the other models considered in this study. *ELFORM 1*, incorporating a viscous-based hourglass control, is recommended for all RHT simulations. Additionally, concerning agreement with the Thorenfeldt theoretical model, the KCC and CSC models appear to match the expected behavior while the Winfrith and RHT models appear to lack accurate incorporation of softening.

3.2.2 ELEMENT SIZE STUDY

As it relates to numerical modeling, element size is most often discussed in the context of mesh refinement. In general, using a fine mesh (i.e., small element size) leads to improved accuracy over coarse meshes and limits geometric approximations. When using nonlinear models, however, it's important to consider how changing the element's size, even in an isolated single-element setting, can alter the numerically generated behavior, all other definitions remaining constant. The element size study detailed in this section aims to illustrate this effect.

Figure 3-6 shows the typical test set up for a multiple element study simulation. The element size of the test specimen was varied from 4 inches to 1 inch using 1-inch increments. This variation was selected as the most common range a user would likely

implement. The coarsest mesh (4 inches) has been taken as the upper extreme for what a user would typically use, while 1 inch represents a relatively small mesh size as compared to the aggregate used within a concrete component. Additional discussion on the element-to-aggregate ratio is provided in the results section of this study.

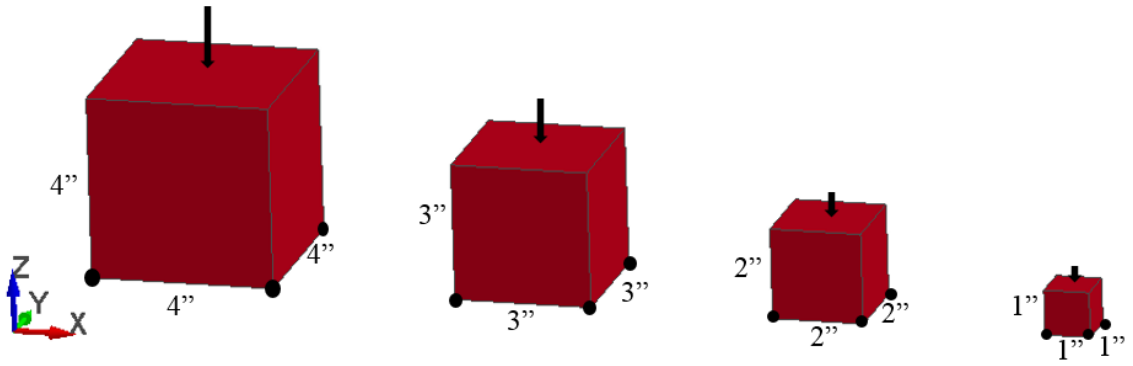

Note: Equal strain has been applied to all elements by scaling imposed displacement based on element size

Figure 3-6: Element size – Monotonic compression test

The boundary conditions for this study were applied just as they were in the element formulation and hourglass control test. Thus, a single bottom corner was pinned while the remaining three bottom corners were supported by rollers. As before, the models were analyzed using displacement control so that the post-peak behavior could be evaluated. An identical displacement curve was assigned to the four top corners of each cube. These displacement curves corresponded to a strain rate of 0.01/sec. Note that the displacement curves applied to each element were modified such that applied strain rate was constant over the entire spectrum of sizes. Additionally, all results shown correspond to *ELFORM 1* implemented with viscous hourglass control. The results did not vary significantly with regards to the specified element formulation or implemented hourglass control, outside of the differences documented in Section 3.2.1.

Figure 3-7 and Figure 3-8 show the results from the element size study run with the KCC material model. As was done with the previous study, results generated using the Thorenfeldt constitutive model have been overlaid with the numerically generated results for comparison purposes. Note that the KCC model computes post-peak behavior variation for varying element sizes. In response to this observation, the model's definition includes the option for user specification of a parameter, *b1*, as defined in Equation 2-1, to account for variation in element size. This parameter essentially acts as a post-peak scaling factor [Crawford et. al., 2012] and has application in simple cases where mesh density is constant over an entire model domain. However, because this is a manually defined parameter, every uniquely sized element must also have a corresponding material definition. Due to this inconvenience, the study of the element size effect on material response has been considered with and without this manual correction factor.

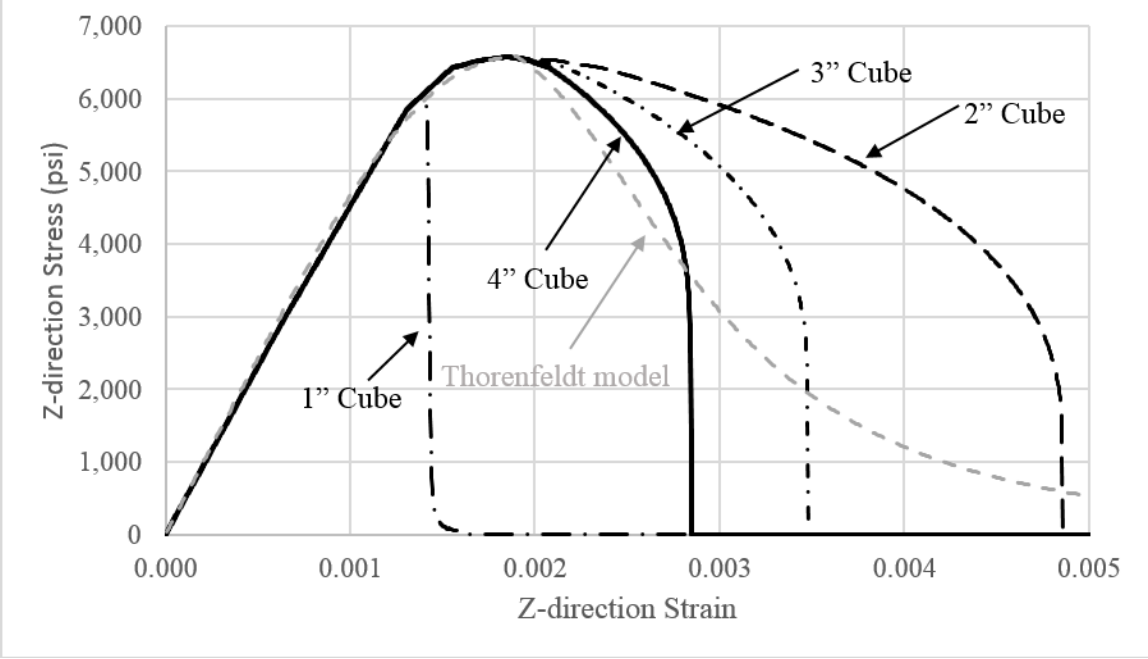

Figure 3-7: KCC element size variation results – No correction factor

Figure 3-7 shows the element size variation results without manual specification of a geometric correction factor. The initial stiffness and capacity of the element was constant over the size variation considered. Furthermore, aside from the 1-inch cube, the numerical model matched the behavior predicted by the Thorenfeldt model. Despite this consistency in the initial response, size variation did have a large effect on the post-peak behavior, where decreasing element size seemed to correspond to decreasing softening rates. As the element size was reduced and the post-peak behavior drawn out, the constitutive model under-estimated post peak-softening and thus over-estimated post-peak capacity as compared to the Thorenfeldt model.

The 1-inch cube element gained strength up to a point less than that seen by the other elements before abruptly losing all capacity. It's hypothesized that this response was seen because the 1-inch cube had a maximum element dimension less than three times the aggregate size used to define the constitutive model. Recommendations by Crawford et. al [2012] advise users against exceeding a 3:1 aggregate-size-to-element-size ratio. Note that this same abrupt capacity loss was also recorded for models implementing a stiffness hourglass control.

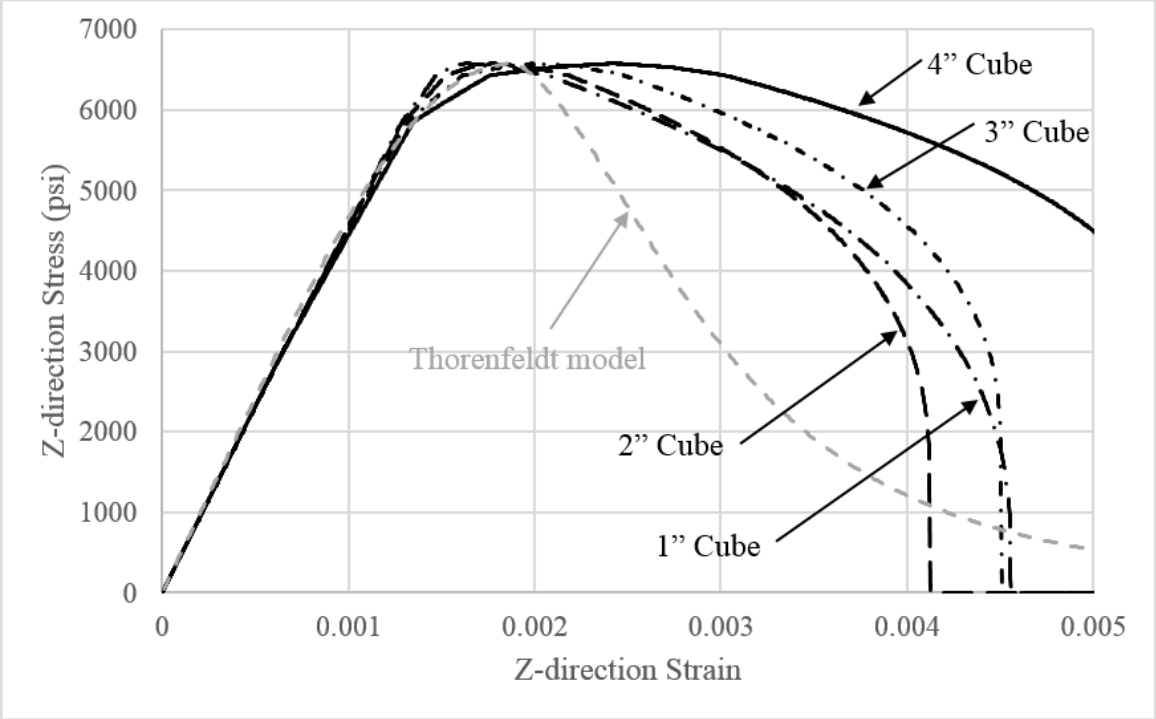

Figure 3-8: KCC Element size variation results – With *b1* correction factor

Figure 3-8 shows the KCC element size variation results with implementation of the *b1* manual adjustment factor. Table 3-2 details the selected adjustment factors for the various sized elements. Including the *b1* factor in the material definition significantly impacted post-peak response and slightly modified the strain corresponding to the element's maximum capacity.

Table 3-2: KCC Element size correction factors

Element Size	4"	3"	2"	1"
b1 factor	2.15	1.81	1.47	1.13

Note that larger elements produced larger *b1* factors, resulting in a greater scaling of post-peak behavior. Prior to the addition of the modification factor, the 4-inch cube showed the quickest post-peak decay; however, after the modification factor was included, the 4-inch element showed the slowest post-peak decay. Additionally, the modification

factor seemed to “fix” the numerical results produced by the 1-inch element. This effect came as a surprise because this modification factor is only intended to modify post-peak behavior, and the 1-inch element abruptly lost capacity prior to reaching the expected peak strength when the correction factor was not included.

In general, the addition of the modification factor seemed to scale the compression response curves beyond that predicted by the Thorenfeldt model. While there are some noted differences in the computed results when using the *b1* factor in comparison to not including it, the overall accuracy was not improved.

As illustrated in Figure 3-9, element size has no impact on the single-element monotonic compression results run using the Winfrith model.

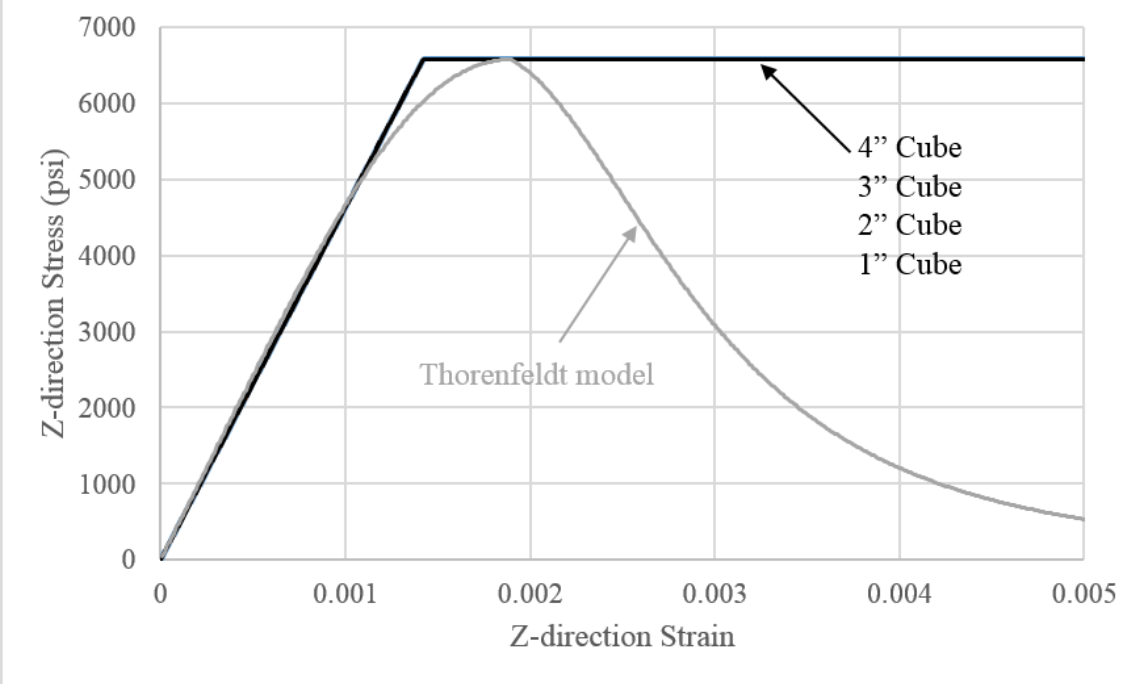

Figure 3-9: Winfrith element size variation results

Figure 3-10 presents the results from the single-element size variation study run with the CSC material model. As with the KCC results, the peak capacity and initial

stiffness were consistent over the entire spectrum of element sizes considered. However, again like the KCC material model, varying the element size produced a scaled difference in the rate of post-peak softening. As the element size decreased, the rate of softening also decreased.

Pre-peak results remained consistent with those predicted by the Thorenfeldt model. The 4-inch cube and 3-inch cube also showed softening responses consistent with that predicted by the Thorenfeldt model; however, both the 2-inch -cube and 1-inch cube showed slow softening degradation as compared to what can be expected for typical concrete. Softening in the 1-inch cube was scaled to a point that the model essentially acted as an elastic-plastic material in the strain range that typically controls concrete response.

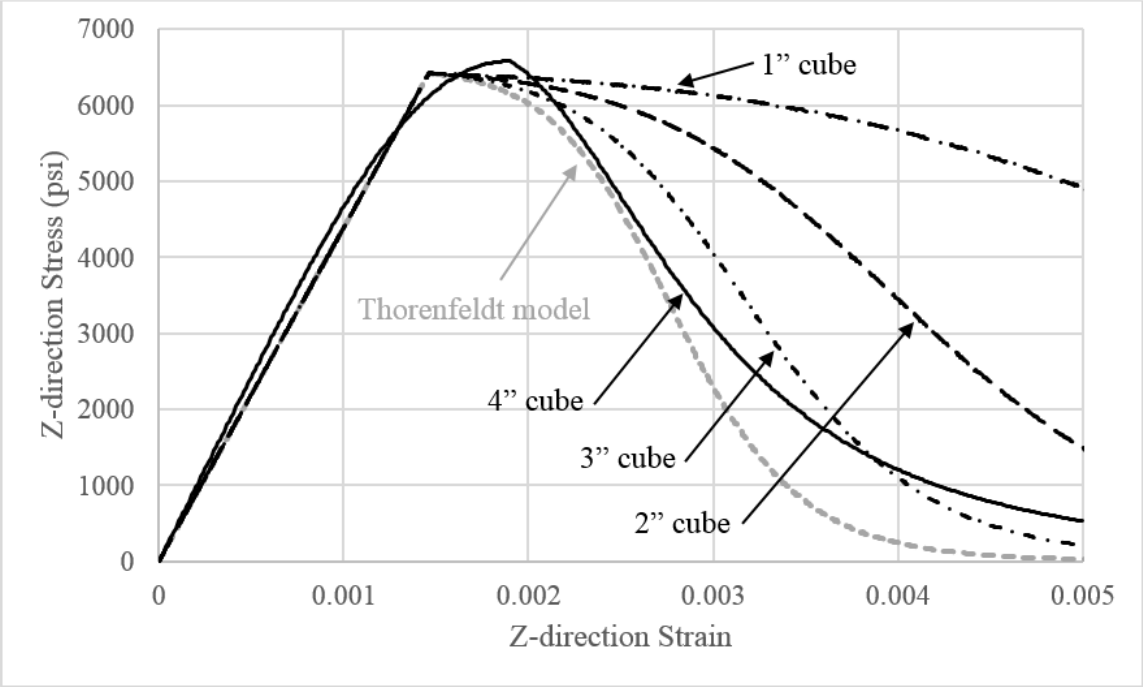

Figure 3-10: CSC element size variation results

As shown in Figure 3-11, element size has no impact on the single-element monotonic compression results run using the RHT model. Again, note that the RHT model over-predicts the user-specified strength for all element sizes.

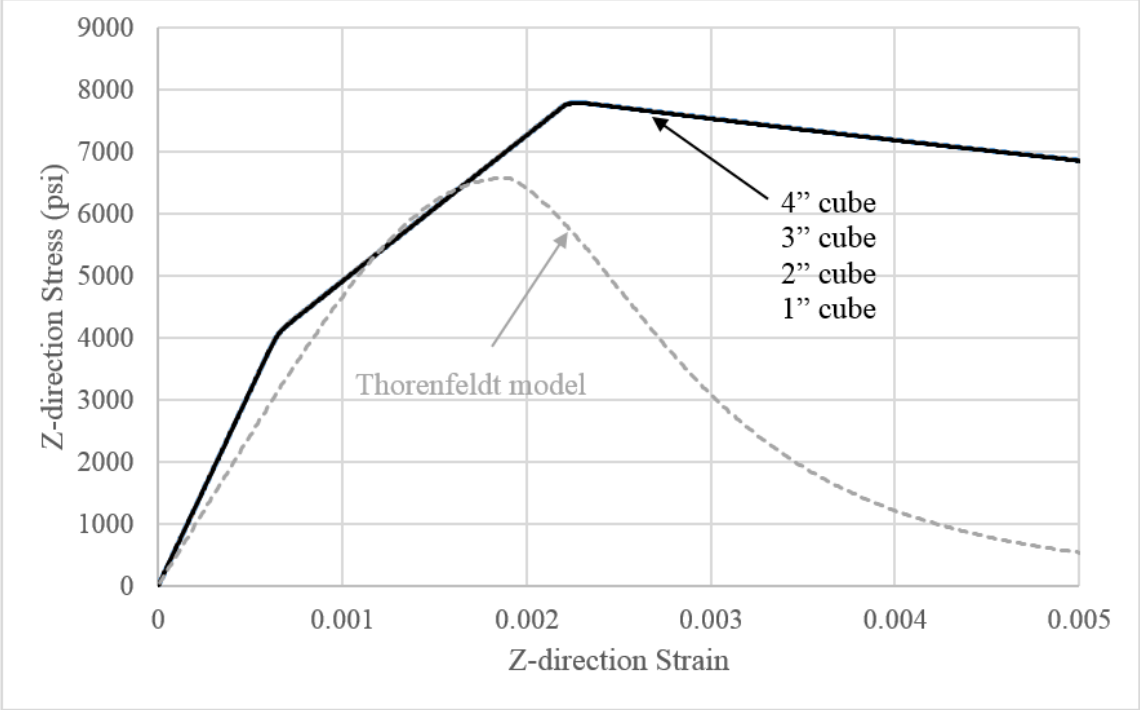

Figure 3-11: RHT element size variation results

3.2.3 STRAIN-RATE STUDY

As discussed in Section 2.1.2, strain rate can play an important role in seismic problems. Seismic strain rates can range anywhere from 10^{-4}/sec to 10/sec, with corresponding DIFs ranging from 1 to 1.5, respectively [Pajak, 2011]. This subsection aims to show how the KCC, Winfrith, CSC, and RHT material models behave when considered with this spectrum of strain rates.

Because LS-DYNA is primarily used for blast and impact problems, the material models contained within the software are generally well equipped to handle strain rate enhancement. As discussed within Section 2.1.2, the Winfrith, CSC, and RHT models all

have DIFs built into their computational algorithms. While the KCC model does not have this built-in feature, it does allow the user to input a curve defining DIF's for a range of strain rates.

Figure 3-13 shows the test set up used for the strain rate variation study. Once again, restraints were added to the bottom surface of the 4-inch-cube using one pin and three rollers. A four-inch element size was selected to minimize the excessive post-peak scaling that can occur in smaller elements as demonstrated in Section 3.2.2. The elements in the test were defined using *ELFORM 1* and a viscous hourglass control. Note that a stiffness hourglass control was also considered for the slower strain rate tests. Identical displacement curves were prescribed to the top four corners of the cubes. Cube 1, Cube 2, Cube 3, and Cube 4 were loaded at rates of 1.0/sec 0.1/sec, 0.01/sec, and 0.001/sec, respectively. This spectrum of strain rates was chosen to best represent the majority of seismic problems.

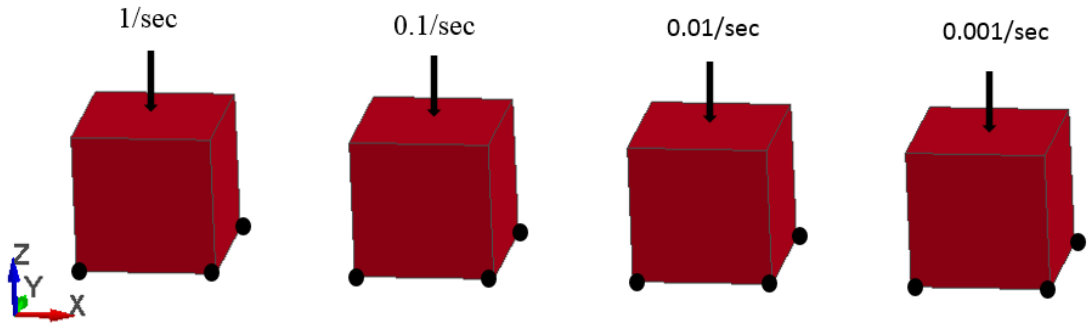

Figure 3-12: Varying loading rate test setup

Figure 3-13 presents the KCC results from the strain-rate variation study (the *b1* scaling factor was not included in the KCC definition used to obtain the results presented in this section). As previously mentioned, the rate effects in this model are incorporated into the formulation by manually specifying a curve that defines DIF versus strain rate. The

specific curve used for this thesis was taken directly from the curve fit proposed in Figure 2-4. While the KCC model does successfully incorporate rate effects into the response, it appears that there is discrepancy between the compressive capacities predicted by the formulation and the expected capacity based on the specified DIF curve. For instance, the manually input curve specifies a DIF of 1.45 at a rate of 1/sec; however, the KCC models yields a value of approximately 1.9 at that same rate. This additional 45% increase in strength beyond the 1.45 user specified DIF value should be noted.

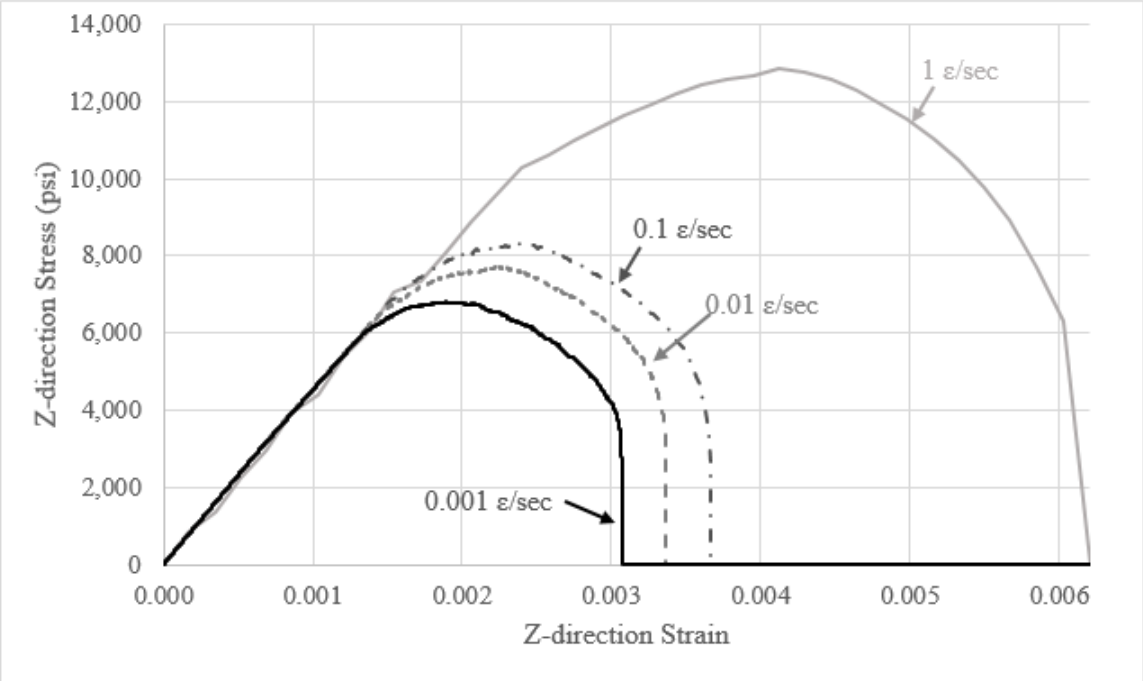

Figure 3-13: KCC strain rate variation study – Including strain-rate enhancement

Of additional note, the KCC strain-rate variation study was repeated for a material definition that did not consider strain-rate enhancement. As expected, the generated numerical results were not sensitive to applied strain rate. However, the lowest strain rate tested, 0.001/sec, appeared to produce a small instability at the transition point between linear and nonlinear behavior. This same abrupt loss of strength was consistently seen over

a spectrum of various hourglass configurations and element sizes. To mitigate this problem, it is recommended that users include a DIF versus strain-rate curve in their material definition regardless of the expected peak strain rate.

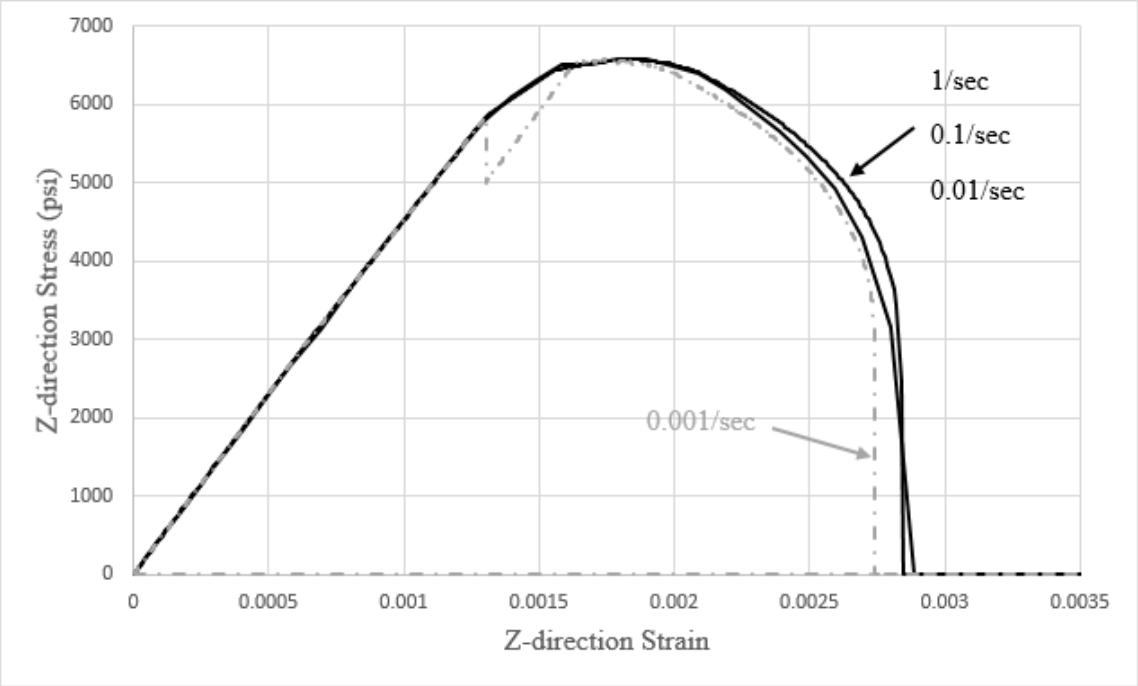

Figure 3-14: KCC strain rate variation study – Not including strain-rate enhancement

Results from the Winfrith strain-rate variation study are shown in Figure 3-15. Rate effects in this model can be turned on and off using the *RATE* variable on the model's keycard definition. Enabling the effects appears not to influence the capacity of the concrete. Additionally, while the Winfrith model typically produces elastic-plastic results, the slowest tested strain rate, 0.001/sec, appears to cause deviations from this perfect elastic-plastic curve shape. However, note that these deviations don't occur until strains far greater than the typical crushing point of concrete. As such, this problem may be mitigated by employing element erosion for plastic strains beyond those typically seen in concrete.

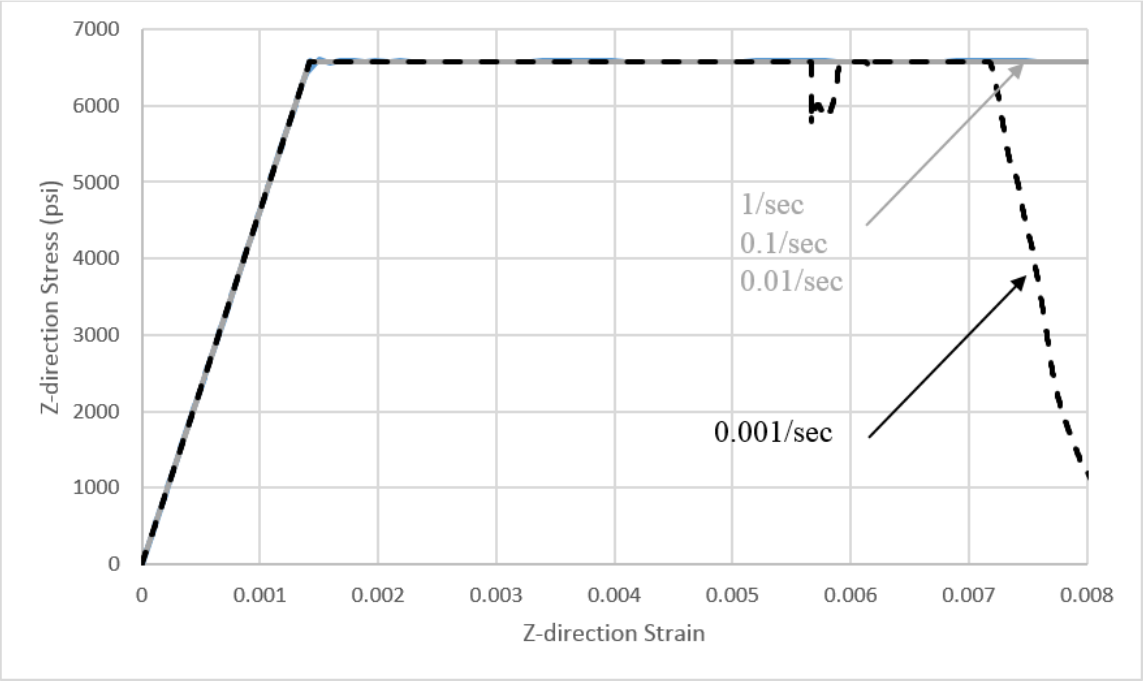

Figure 3-15: Winfrith strain rate variation study

Rate effects in the CSC model are introduced into the formulation by setting the keycard definition *IRATE* to a value of 1. Results showing a variation of strain rates with this effect enabled are provided in Figure 3-16. As expected, the capacity of the concrete increased as the strain rate increased from 0.001/sec to 0.1/sec. The element loaded at a rate of 1/sec, however, had a capacity less than that loaded at rate of 0.1/sec. From Figure 2-4 it's clear that a decrease in predicted capacity is not expected with an increasing strain rate. Note that, as expected, when the strain-rate effects were disabled, each element produced an identical response.

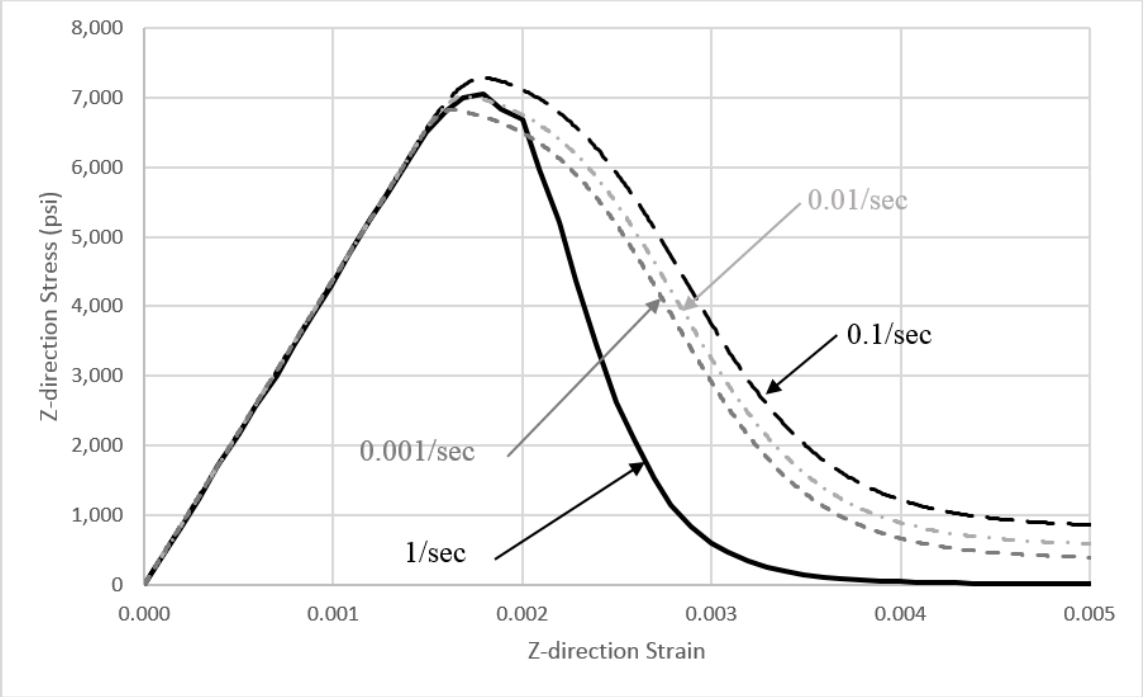

Figure 3-16: CSC strain rate variation study

Figure 3-17 shows the results for the RHT strain-rate variation study. Because the automated parameter tool was utilized for this study, the strain-rate enhancement parameters used within the material's formulation were also automatically generated. Note that a user can manually override the automated variable generator if desired. As expected, increased strain rates resulted in increased capacities for the entire spectrum of tested rates. Initial stiffness was unaffected by the strain rate. This observation is in agreement with anticipated behavior. As previously discussed in Section 3.2.1, the automated RHT curve has a slow softening response compared to experimental data and theoretical models. This effect is exacerbated with increased capacity. Although it is difficult to tell the main ramifications of this increased capacity and slow softening degradation, users should be aware of this simplified response.

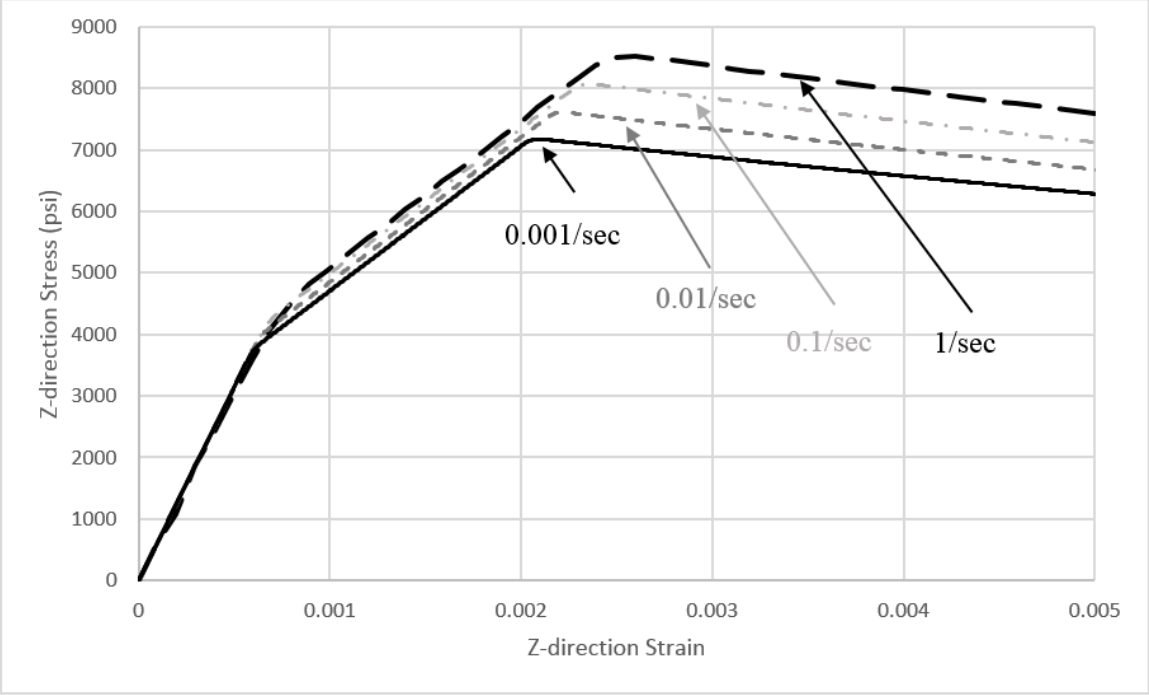

Figure 3-17: RHT strain-rate variation study

3.3 SHEAR STUDY

While modeling the shear capacity of concrete is important for most applications, seismic scenarios often produce large lateral forces that can cause substantial shear demand in lateral systems. As such, a material model's ability to accurately capture shear is of particular importance to seismic problems. Over the past several decades, significant effort has been directed towards properly modeling concrete's response to shear. Entire plasticity models, such as the modified compression field theory (MCFT), have even been developed for such a purpose. Validating concrete response under shear loads is an immensely complicated topic, so much so that a thorough shear validation of the various LS-DYNA concrete models could in itself be a thesis topic. Nonetheless, this thesis aims to show that

the KCC, Winfrith, CSC, and RHT formulations have the capabilities to adequately model concrete's response to shear loading.

Figure 3-18 shows a differential element subjected to a shear stress. Note that the element can be rotated an angle θ_c to transform the shear stress, v_{cxy}, into a combination of principal stresses, f_{c1} and f_{c2}. An element's response to shear can be equivalently tested using a "direct shear" test, illustrated to the left, or using an "indirect shear" test, illustrated to the right. This thesis uses an "indirect shear" approach to investigate such behavior as it presents the most convenient method for basic validation. This basic validation aims to demonstrate each material model's capability to predict concrete's response to tensile loading and to capture compression softening.

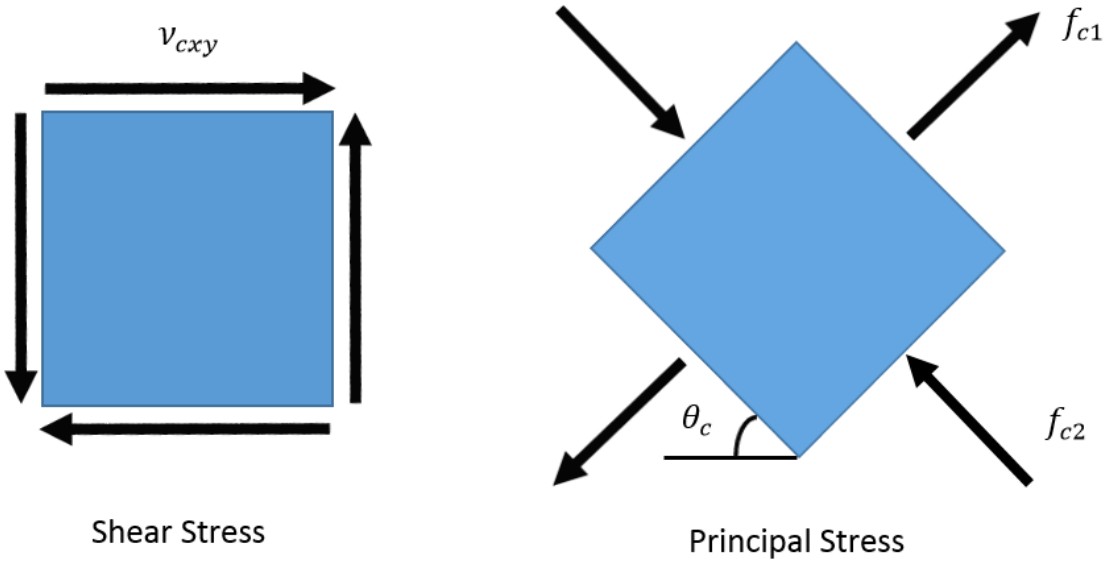

Figure 3-18: A differential element subjected to shear stress

3.3.1 UNCONFINED UNIAXIAL TENSION

When considering the unconfined uniaxial tension response of pure concrete, it's important to make a couple of distinctions. First, pure concrete has no post-crack tensile capacity. Its tensile stress-strain curve can be described using a simple linear equation that abruptly drops to zero at the point of cracking. However, the vast majority of concrete models are implemented in members that contain some percentage of reinforcement. While the material properties and restraints of such reinforcement can be directly included into a numerical model using additional elements, there is a bond interaction between the rebar and concrete that also contributes to strength. This additional contribution to the capacity of the composite material is known as "tension stiffening" and is often added to the concrete constitutive model [Behfarnia, 2009].

As a reinforced concrete member cracks, it forms a series of large "primary cracks." While these large cracks represent an area where the concrete can no longer carry capacity, the concrete between the primary cracks is kept intact by a bond formed between the rebar and the concrete. Because this intact concrete can still carry load, the average tensile stress carried by the concrete is not zero, but rather some fraction of the original concrete tensile capacity. Again, because this effect is typically considered within the concrete constitutive model, pure concrete models often include post-crack capacity. Users should understand that these models are only to be used when reinforcement exists within the concrete being modeled.

While several models have been proposed for modeling tension stiffening, this thesis uses the concrete constitutive model implemented in the 1981 formulation of the MCFT for its tension validation [Vecchio, 1982]. This proposed relation, as described in Equations 3-6 and 3-7, has been selected because it does not require extensive calculations and is particularly effective for small elements.

$$f_{c1} = E_c \varepsilon_{c1} \quad \text{for} \quad 0 < \varepsilon_{c1} \le \varepsilon'_t \qquad \text{Equation 3-6}$$

$$f_{c1} = \frac{f'_t}{1 + \sqrt{200 \varepsilon_{c1}}} \quad \text{for} \quad \varepsilon_{c1} > \varepsilon'_t \qquad \text{Equation 3-7}$$

where f_{c1} is concrete tensile capacity, $E_c = 2f'_c / \varepsilon'_c$, $\varepsilon'_c = 0.002$, $f'_t = 4\sqrt{f'_c}$, and $\varepsilon'_t = f'_t / E_c$. Note that the value predicted by Equation 3-6 may be further limited by the reinforcement's ability to carry stress across a crack [Vecchio, 1986]. This means that when implemented, this proposed curve will have an additional branch capping the tensile capacity at high strains based on the specific problem's reinforcement layout [Vecchio, 1986].

Figure 3-19 shows the KCC, Winfrith, CSC, and RHT models subjected to unconfined uniaxial tension, as well as an overlaid 1981 MCFT prediction. As a whole, the models perform well at capturing tension-stiffening. Although the models appear to have under-predicted the concrete tensile capacity at high strains as compared to the 1981 MCFT model, this plot does not show the limiting branch that applies to the MCFT curve, based on specific reinforcement limits. Because the LS-DYNA models are intended to be used for a general reinforcement layout, it seems reasonable that they implement a more conservative version of the curve. The exception to this good fit is the RHT model, which once again over-predicted concrete capacity by a large margin.

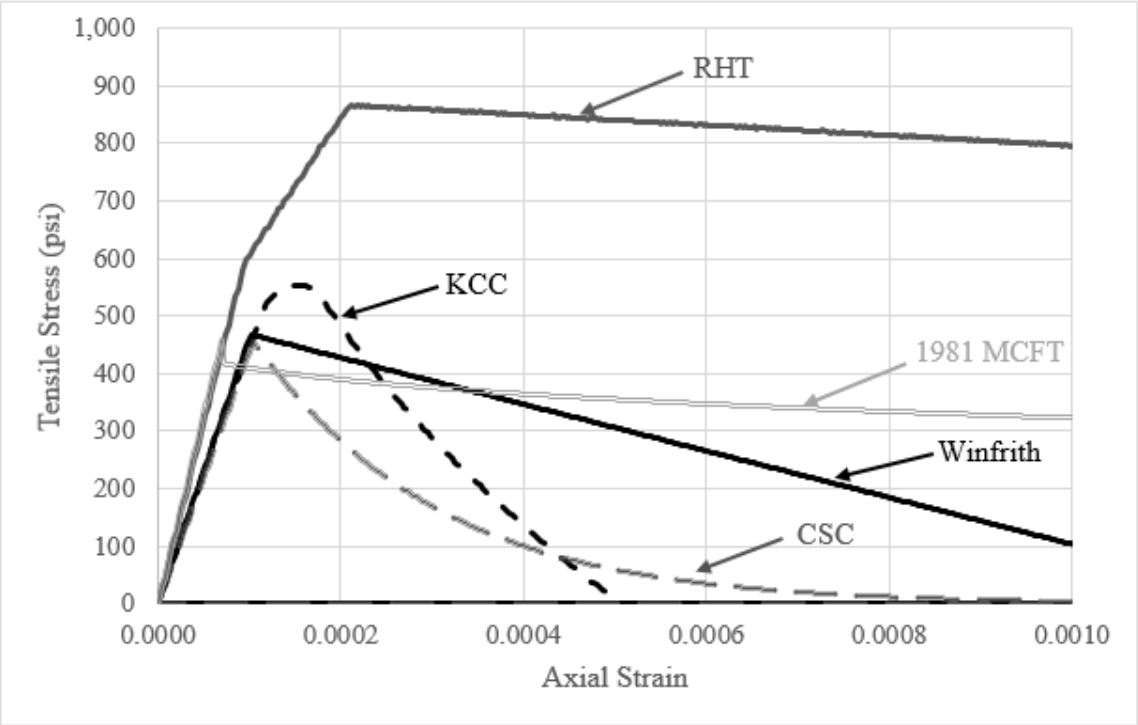

Figure 3-19: KCC, Winfrith, CSC, and RHT material model UUT results

3.3.2 Compression Softening – Concrete's Response To Biaxial Compression-Tension Loading

The second major component of an "indirect shear" validation is assessing how the various material models capture compression softening. Again, consider the element shown in Figure 3-18. Note that the element is in a biaxial state of loading. When concrete is subjected to this particular biaxial stress state, compression on one face and tension on the other, the compressive capacity of the concrete has been shown to be reduced as compared to uniaxial compression [Kufer, 1969].

Validation for this biaxial loading state has been based upon a variation of Saenz's uniaxial compression equation proposed in 1964 [Saenz, 1964]. As per recommendations made by Chen [1981], this equation was adapted to fit a biaxial response by replacing the uniaxial compressive capacity, corresponding strain at maximum capacity,

and secant modulus with their biaxial equivalent versions presented in [Kufer, 1969] and shown in Figure 3-20 and Figure 3-21. This adapted expression is presented in Equation 3-8:

$$\sigma_i = \frac{E_o \varepsilon_i}{1+[(E_o \varepsilon_{1u} / \sigma_p)-2](\varepsilon_i / \varepsilon_{1u})+(\varepsilon_i / \varepsilon_{1u})^2} \qquad \text{Equation 3-8}$$

where σ_i is the uniaxial equivalent stress, E_o is the concrete's initial tangent modulus, σ_p is the uniaxially equivalent peak compressive capacity, ε_{1u} is the corresponding strain at this capacity, and ε_i is the strain at point *i*. The specific variable definitions, as they apply to different states of biaxial loading, are provided in Table 3-3.

Table 3-3: Uniaxially equivalent parameters used to represent biaxial behavior

σ_2 (psi)	0	-100	-200	-300
$\sigma_2 / \beta p$	0.0000	-0.0152	-0.0304	-0.0456
$\sigma_1 / \beta p$	1.0000	0.9758	0.9418	0.8857
σ_1 (psi)	6580	6421	6197	5828
σ_1 / σ_2	-	-64.2	-31.0	-19.4
α	4.71	4.73	4.74	4.76
ε_{1u}	0.0020	0.0018	0.0018	0.0015

where σ_1 is the primary principal stress, σ_2 is the secondary principal stress, β_p is the uniaxial unconfined compressive strength, $\alpha = \tan^{-1}(\sigma_1/\sigma_2)$, and ε_{1u} is the strain corresponding to the maximum compressive strength. The general calculation process was conducted as follows. The secondary principal stress, σ_2, was selected to match the dimensions of the compression softening study. The parameter σ_1/β_p was calculated using Figure 3-21, and ε_{1u} was calculated using Figure 3-22.

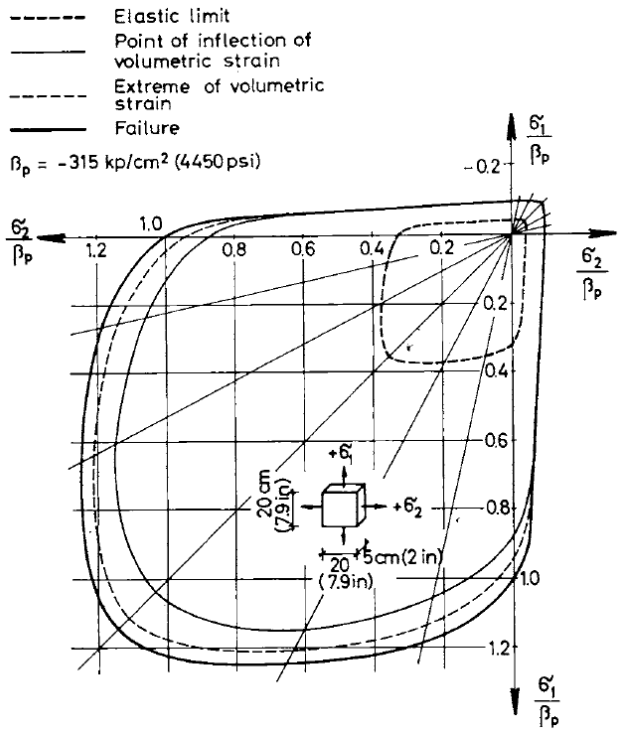

Figure 3-20: Failure stress envelope in concrete under bi-axial loading [Kufer, 1969]

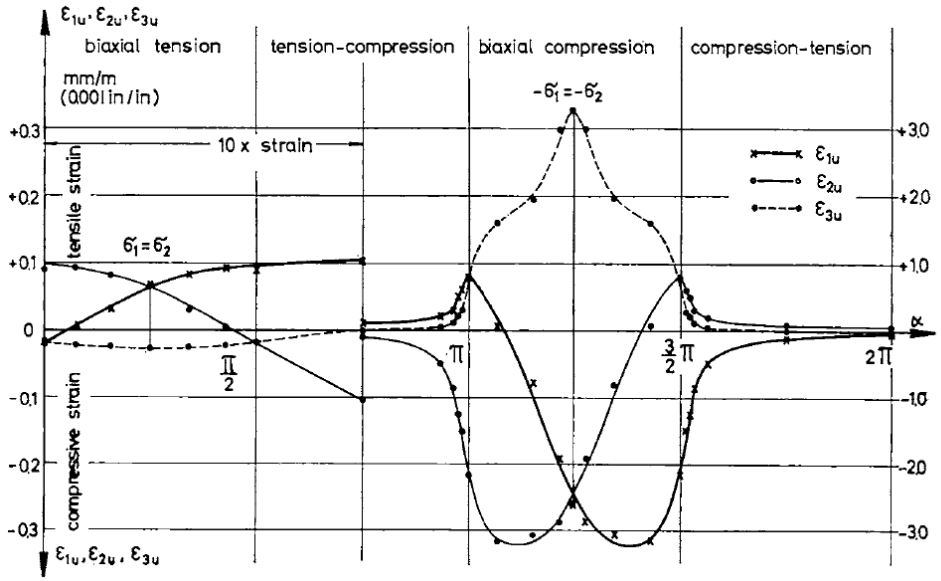

Figure 3-21: Failure strains in concrete under biaxial loading (where $\alpha = \tan^{-1}(\frac{\sigma_1}{\sigma_2})$) [Kufer, 1969].

Each compression softening test was run using 4-inch cube elements defined using *ELFORM 1* with viscous hourglass control. The elements were restrained using one pin and three rollers along the bottom face. The compression portion of the biaxial loading was prescribed using four identically defined displacement curves, while the tension portion of the loading was applied using a defined pressure. The tensile component of the loading was varied to include 0psi, 100 psi, 200 psi, and 300 psi.

The results of the compression softening analyses, presented in Figures 3-22, 3-23, 3-24, and 3-25, show that as the tensile component of the biaxial loading is increased, the compressive capacity of the element, as well as the strain corresponding to the peak compressive stress, is reduced. Note that this same behavior was exhibited by all four material models. This behavior is consistent with the trends demonstrated by the overlaid series of Saenz-Kufer theoretical curves. While the magnitude of this reduction appears to be slightly greater in the numerical results, as compared to the theoretical results, the specific magnitude of the reduction is sensitive to the concrete used to calibrate the theoretical expression. Therefore, each model's ability to capture the previously discussed trends is considered to be more important than matching the specific values presented.

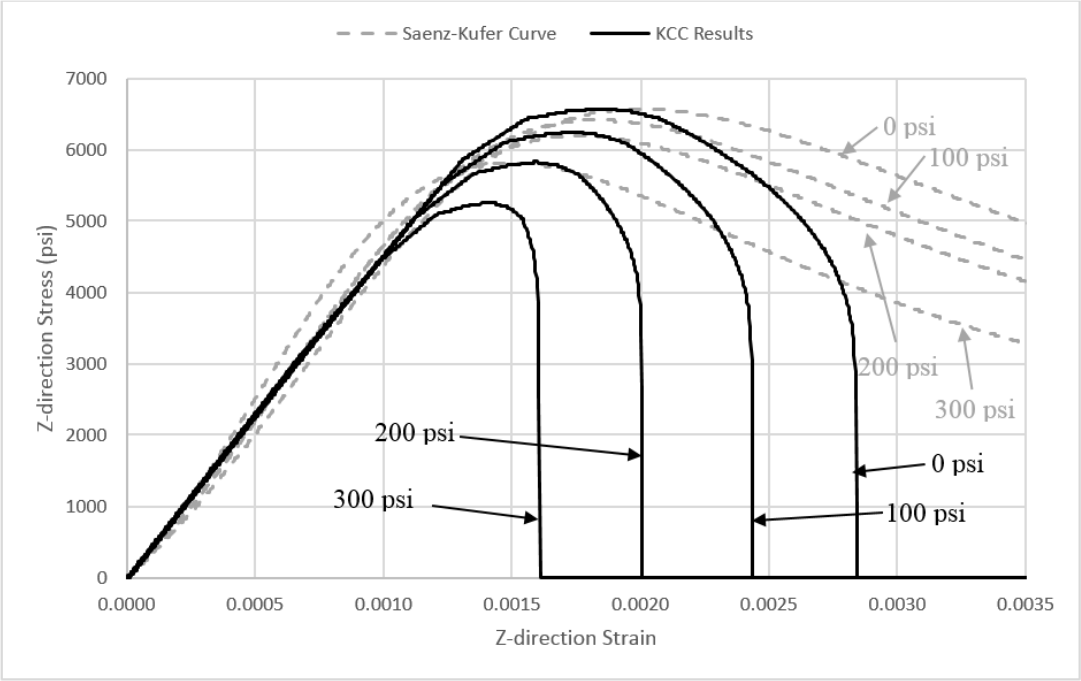

Figure 3-22: KCC compression softening study results

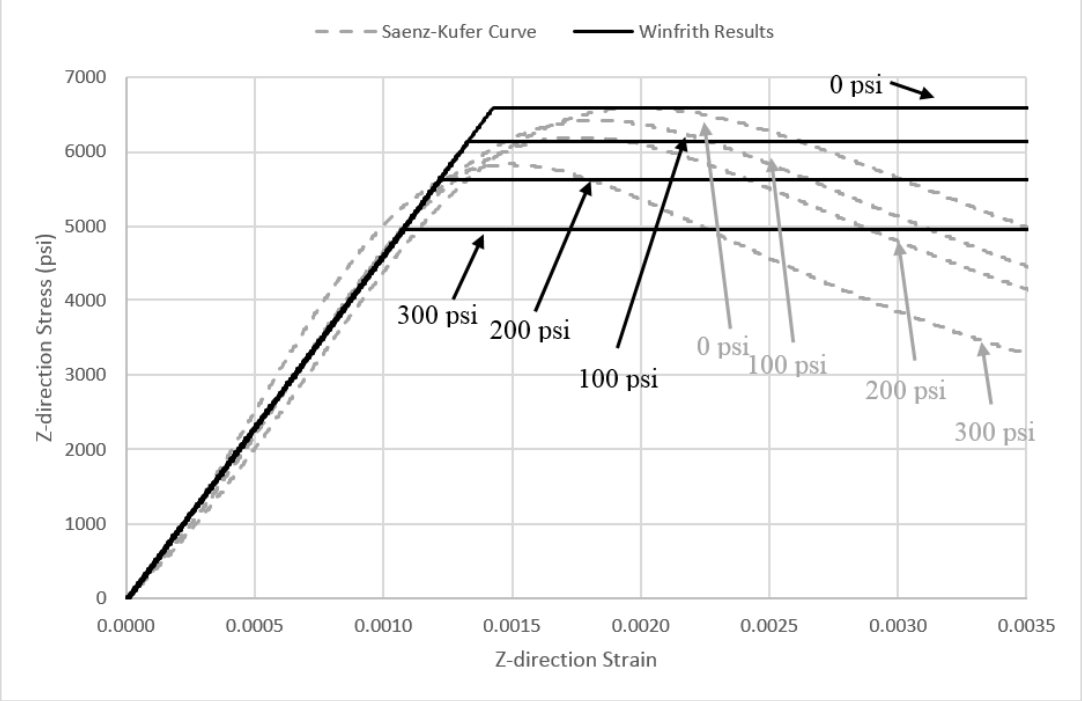

Figure 3-23: Winfrith compression softening study results

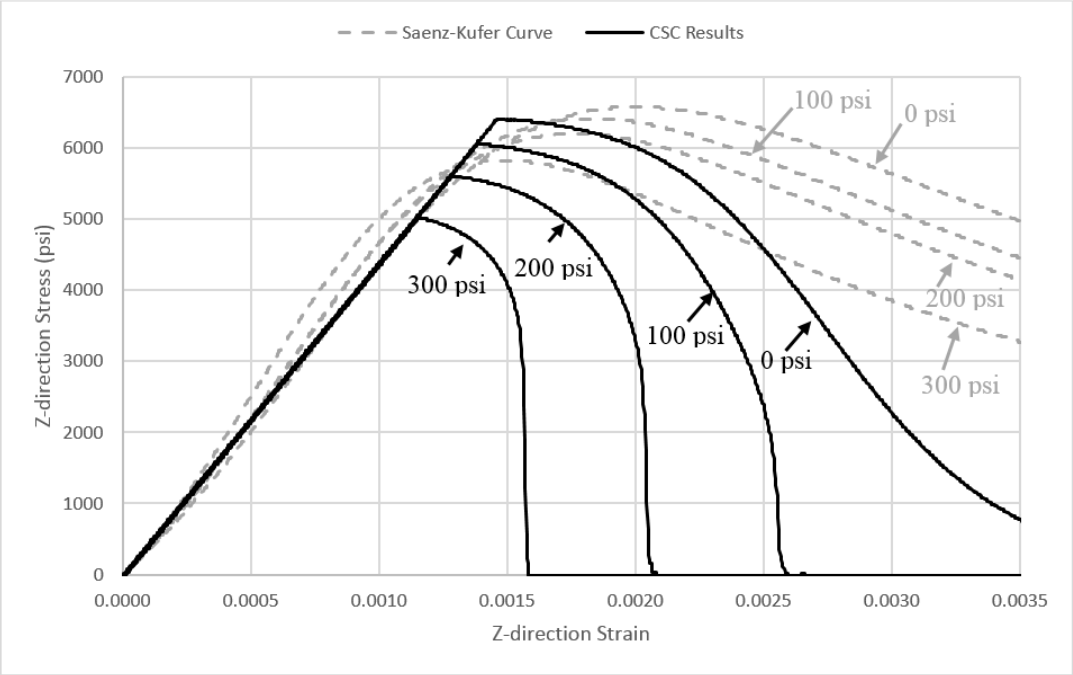

Figure 3-24: CSC compression softening study results

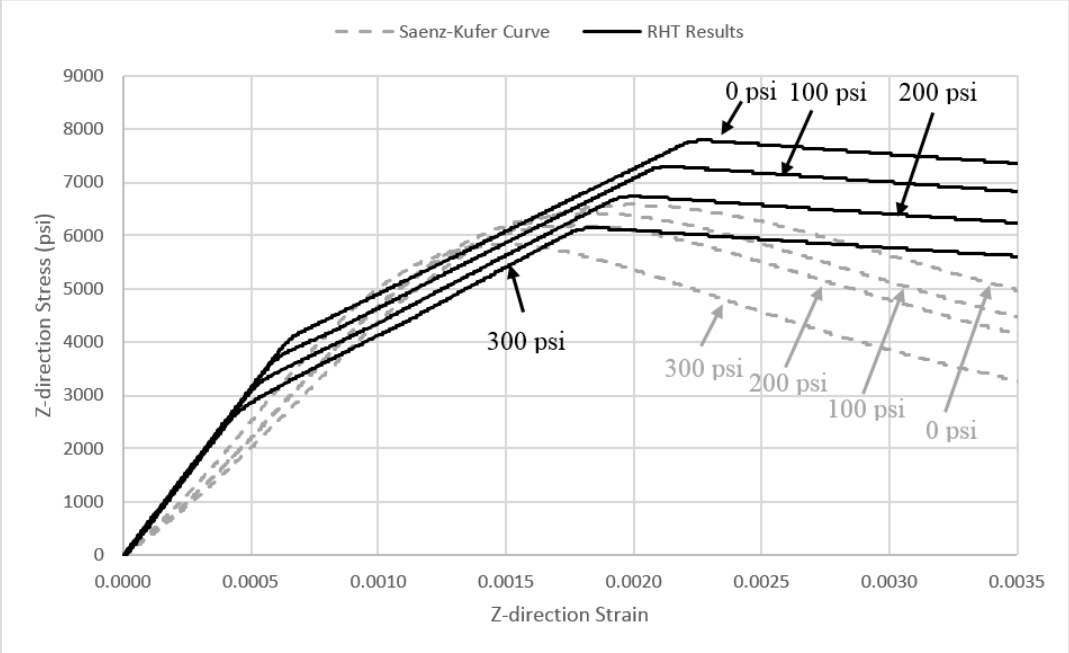

Figure 3-25: RHT compression softening study results

3.4 CYCLIC LOADING

Concrete's behavior under cyclic loading is dependent many variables including load history which, coupled with its highly nonlinear nature, makes capturing cyclic behavior rather involved [Bahn and Hsu, 1998]. Not only must proposed models capture post-peak softening behavior, they must also consider strength degradation in terms of both modulus and capacity reduction. The mathematical formulations used to describe such behavior are often complicated as it can be necessary to include sophisticated damage calculations to accurately capture the various stress paths required.

To date, LS-DYNA has been primarily used for blast and impact problems. These types of loadings have required concrete material models to accurately capture rather complicated behavior such as highly dynamic loading, confinement, shear dilatancy, etc. However, blast and impact loadings often represent single impulse problems where, outside of free vibration, there is little need to consider high magnitude cyclic loads. The result is that the concrete material models contained within the platform have seen very limited validation for such loading. As such, it's hypothesized that the formulations contained within the LS-DYNA concrete material models may not be well suited for cyclic loading, and therefore, seismic application.

The goal of this subsection is to understand how each material model tracks damage and generates a response under a cyclic loading scenario. Two single-element tests have been included within this section to illustrate both of these goals. The first test is designed to mimic a traditional cyclic compression test where the element is loaded, unloaded, and then reloaded to a progressively higher compressive strain at every iteration. This type of test is particularly useful for showing how a model unloads, reloads, and tracks damage while in a constant state of compression. While understanding this behavior is important, load reversal is very common within seismic problems, leading to an additional need to

understand how each material model captures full hysteresis loops. As such, the second test has been designed to show how the various concrete models load and unload when subjected to full compression and tension cycles.

Experimental validation for the cyclic compression test comes from results presented by Bhan and Hsu [1998]. This study was conducted to develop a simple mathematical expression that could accurately represent concrete under a full envelope of cyclic loading. Although the proposed theoretical expression seems to consistently capture the experimental results, the experimental results themselves are used for validation within this thesis. The concrete used within the study was reported to be a normal-weight mix with a maximum aggregate size of 0.375-inch. Note that the actual strength of the concrete was not included in the study as the results were reported in terms of normalized stress and strain ratios. Validation for the full tension and compression cycle test is more difficult because experimental testing does not subject pure concrete to such a scenario. However, while validation through experimental data is not possible, simple observation can lead to several important conclusions.

3.4.1 CYCLIC COMPRESSION STUDY

The 4-inch single-element model used for the cyclic compression test was restrained with boundary conditions identical to what has been previously presented. The results detailed in this subsection were collected for elements defined using *ELFORM 1* and viscous hourglass control unless otherwise specified. Four identical displacement curves, detailed in Figure 3-26, were assigned to the top corners of the element. The selected displacement curve was developed to mimic the strain history presented in [Bahn and Hsu, 1998].

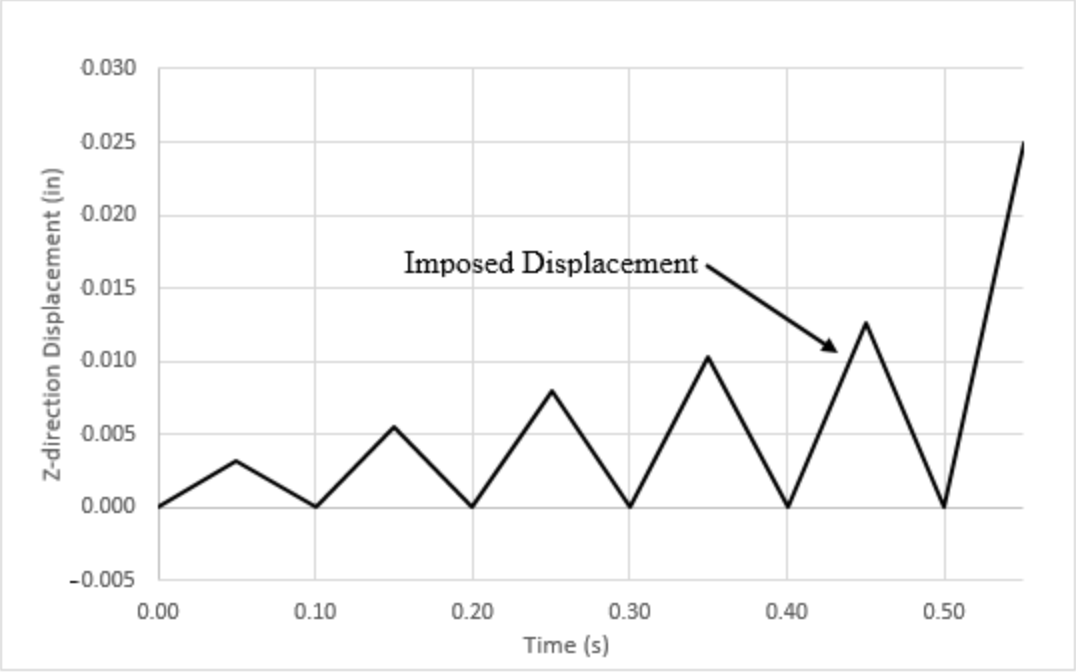

Figure 3-26: Cyclic compression imposed displacement

Figure 3-27 shows the KCC cyclic compression results overlaid with experimental data (the *b1* scaling factor has not been included in the KCC material model used to obtain these results). Note that the results are presented in terms of normalized stress and strain ratios to match those provided in [Bahn and Hsu, 1998]. It appears that the KCC model both loads and unloads with a constant modulus that matches the stiffness of the initial portion of monotonic compression curve. Consistent with that described in [Crawford et. al, 2012], damage seems to be based on a plastic strain parameter. Although the model does not capture the loops or stiffness degradation seen in the experimental results, the overall fit appears reasonable. However, because the KCC model loses all capacity at a strain ratio of roughly approximately 1.5, the high strain portion of the curve is not captured. Note that stain ratio is defined as strain normalized by strain corresponding to peak capacity.

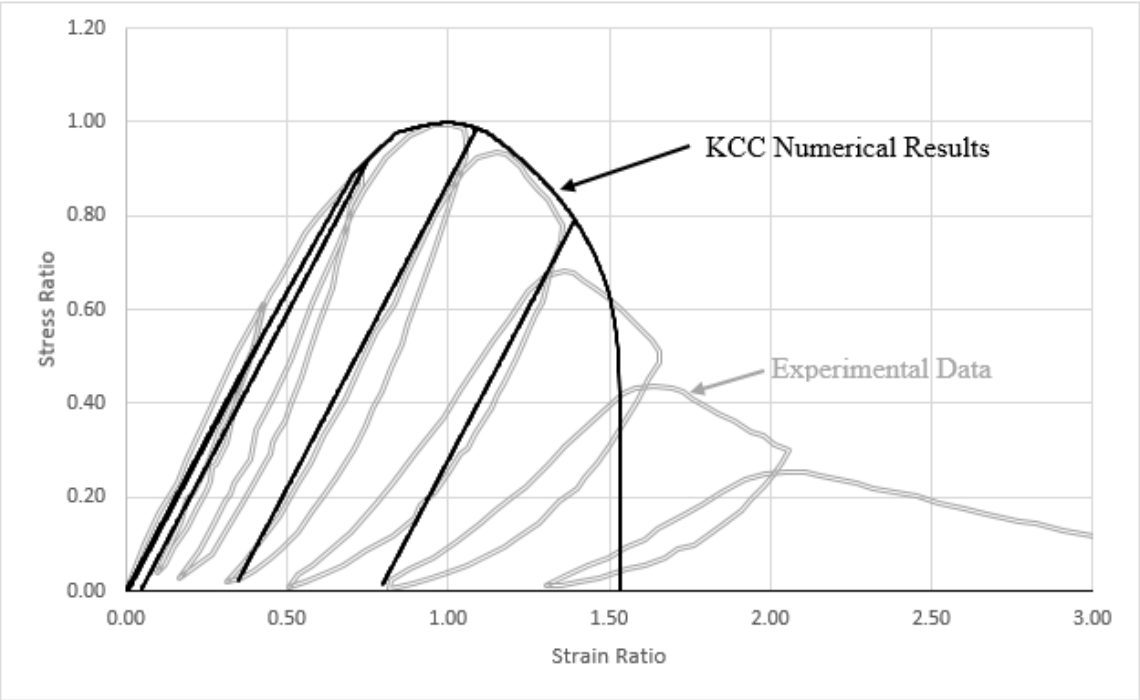

Figure 3-27: KCC normalized cyclic compression results

The results of the Winfrith cyclic compression test, presented in Figure 3-28, seem to show poor agreement between the numerically generated results and previously collected experimental data. Because the Winfrith model uses an elastic-plastic representation for the concrete, it does not have the capability to model strength degradation or stiffness degradation, two of the main components of cyclic loading response. Additionally, unloading and reloading near the elastic-plastic transition point seems to have caused a small instability in the formulation. Rather than the typical transition that is present in the monotonic curve, shown in Figure 3-3, there seems appears to be an abrupt loss of strength just past beyond the transition point.

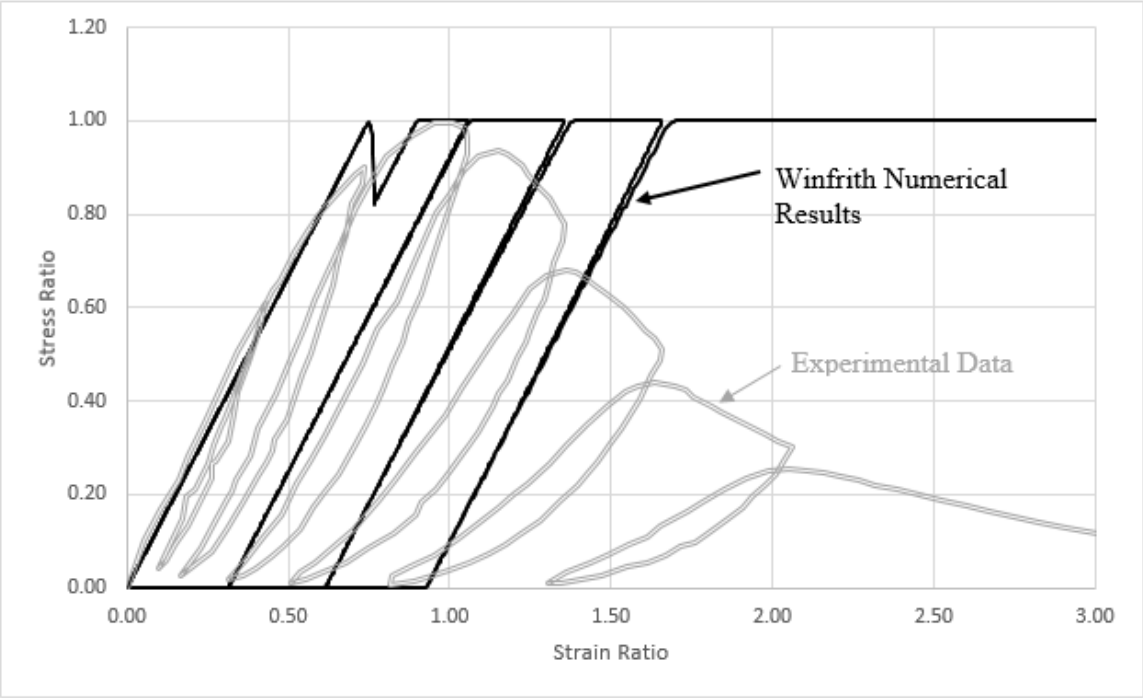

Figure 3-28: Winfrith normalized cyclic compression results

The CSC model results, shown in Figure 3-29, show very good agreement between the numerical results and experimental data. The CSC model appears to not only capture stiffness degradation, something the other three models failed to do, but also accurately matches the magnitude of stiffness degradation exhibited in the experimental data. Consistent with that described in [Murray, 2004], and similar to that used in the KCC model, damage appears to be calculated based on a plastic strain parameter. Note that the results shown in Figure 3-29 were collected based on an element defined using *ELFORM 1* and a viscous hourglass control. Figure 3-30 shows the same simulation run for an element defined using *ELFORM 2*. Again, the shape of the curve seems to corresponds reasonably well with the experimental data.

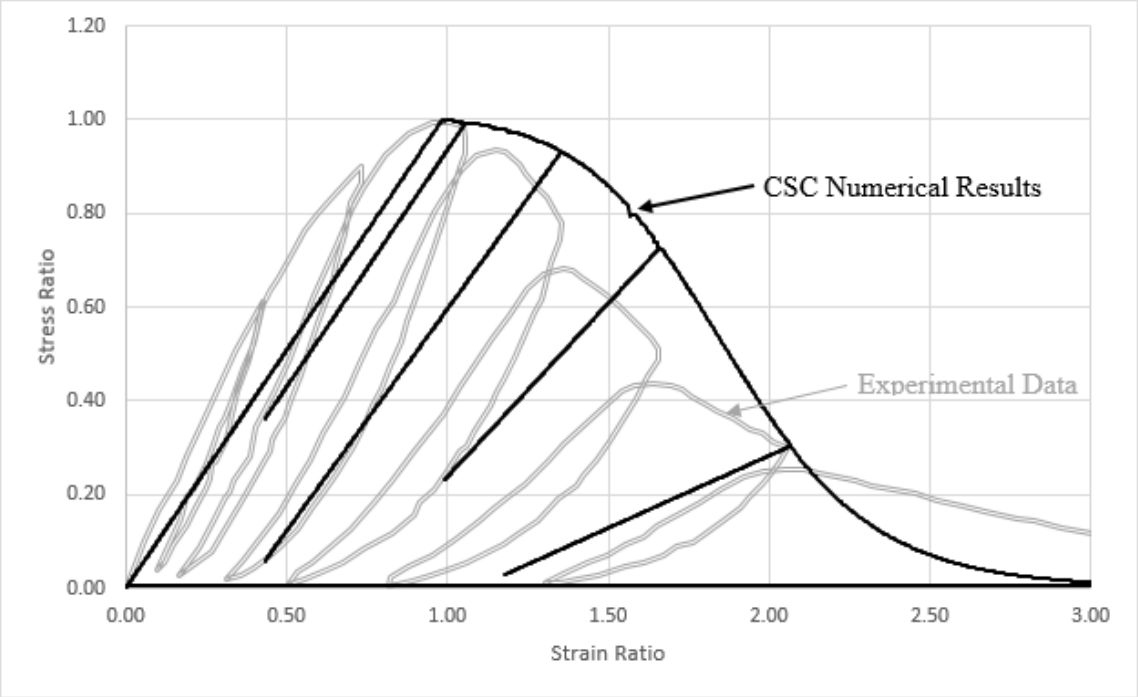

Figure 3-29: CSC normalized cyclic compression results – *ELFORM 1*

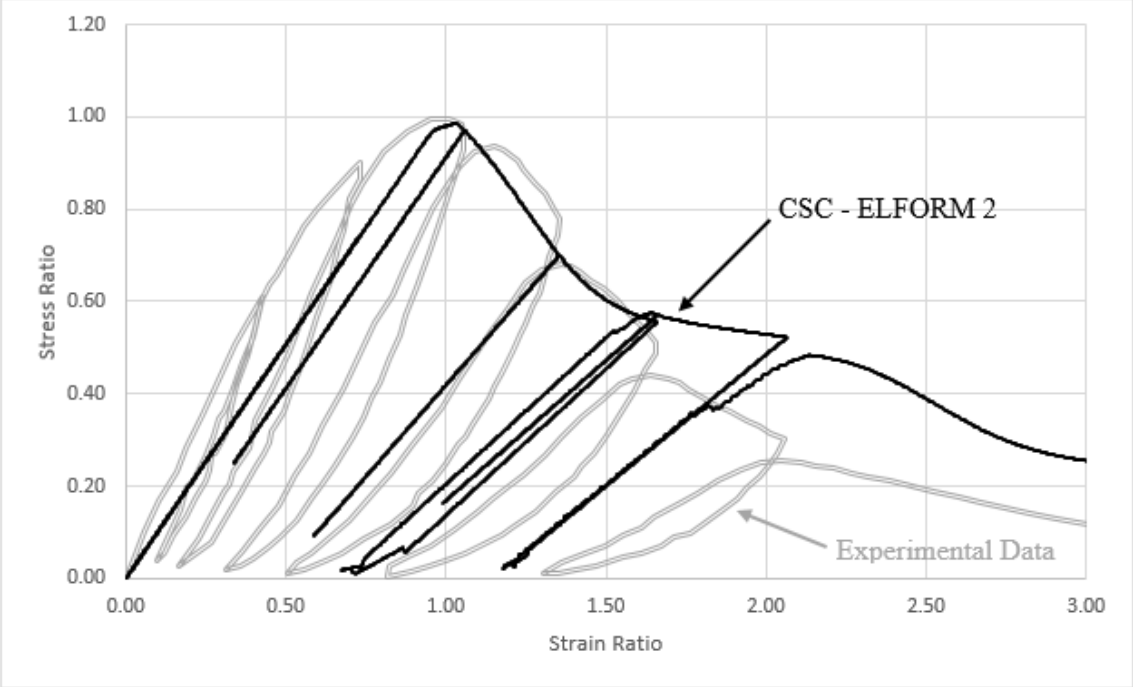

Figure 3-30: CSC normalized cyclic compression results – *ELFORM 2*

Lastly, the results for the RHT cyclic compression test are shown in Figure 3-31. Similar to the Winfrith model, the fundamental form used to model the concrete's compressive behavior severely limits the potential agreement between the numerical results and experimental data. As discussed in Section 3.2.1, the gradual softening behavior leads to significantly higher than expected concrete capacities at high strains. Additionally, the automatically generated RHT model does not achieve peak capacity until a strain ratio, as normalized with the experimental data, of nearly 1.4 which significantly offsets the numerically predicted behavior from the experimental data. Again, note that the model does not have the capability to capture stiffness degradation.

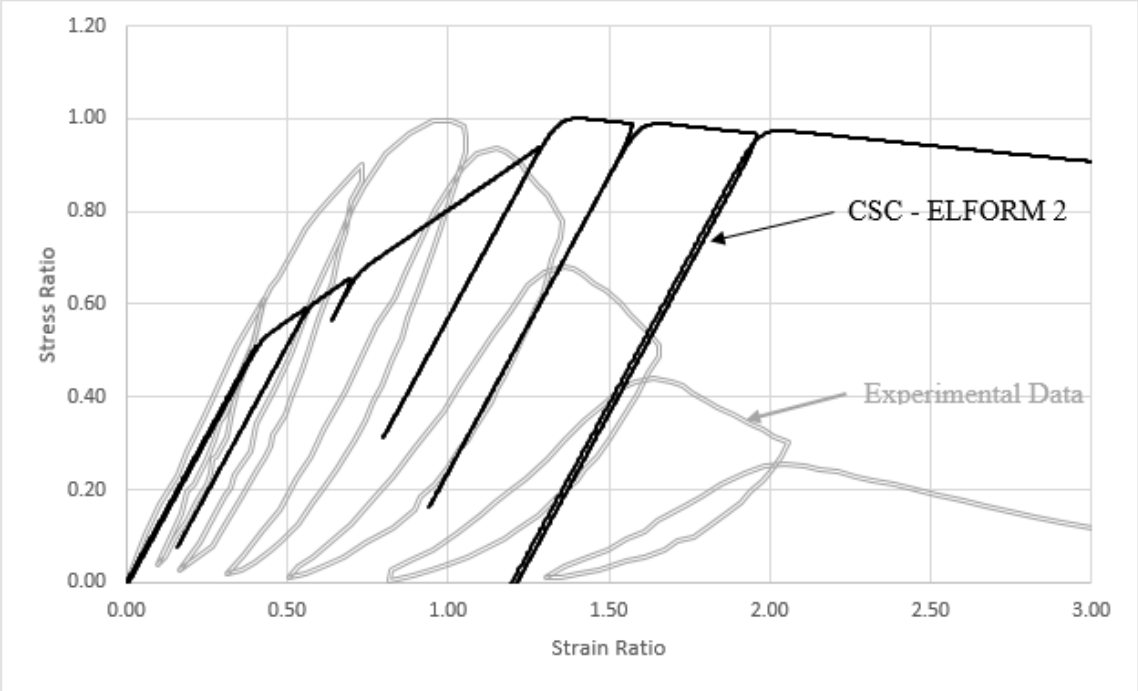

Figure 3-31: RHT normalized cyclic compression results

3.4.1 CYCLIC COMPRESSION-TENSION STUDY

The full cyclic -tension-compression test marks the final single-element test to be presented. As previously discussed, this test is designed to illustrate how each material

model unloads, reloads, and captures damage when subjected to full load reversal. The definitions described for the cyclic -compression test were also used for the cyclic -tension-compression test, with the exception of the specified load curve. The load curve has been developed such that the element is subjected to ten cycles of identical compressive and tensile displacements. The magnitude of the displacement has been strategically selected to demonstrate behavior described in the following sections.

Figure 3-32 shows the results for the KCC model subjected to ten cycles of load reversals (the *b1* scaling factor has not been included in the KCC material definition used to obtain these results). The initial compressive loading, compressive unloading, and tensile loading phases seem to behave as expected. However, once the concrete has cracked and reached a point of zero tensile strength, it appears that the compressive capacity of the model remains at zero for the remainder of the simulation. While it could be expected that the tensile capacity remains at zero for the remained remainder of the simulation, it's reasonable to assume that even cracked concrete has some level of remaining compressive capacity. The error seems to be associated with how the model tracks damage. As discussed in Section 2.3, the KCC formulation uses a single variable to record both damage accumulated in tension and damage accumulated in compression. It's hypothesized that the tensile phase of the simulation drove the single damage variable to a maximum value, eliminating any compressive capacity. Until a second damage variable is added into the formulation, release three of the KCC material is not recommended for seismic applications.

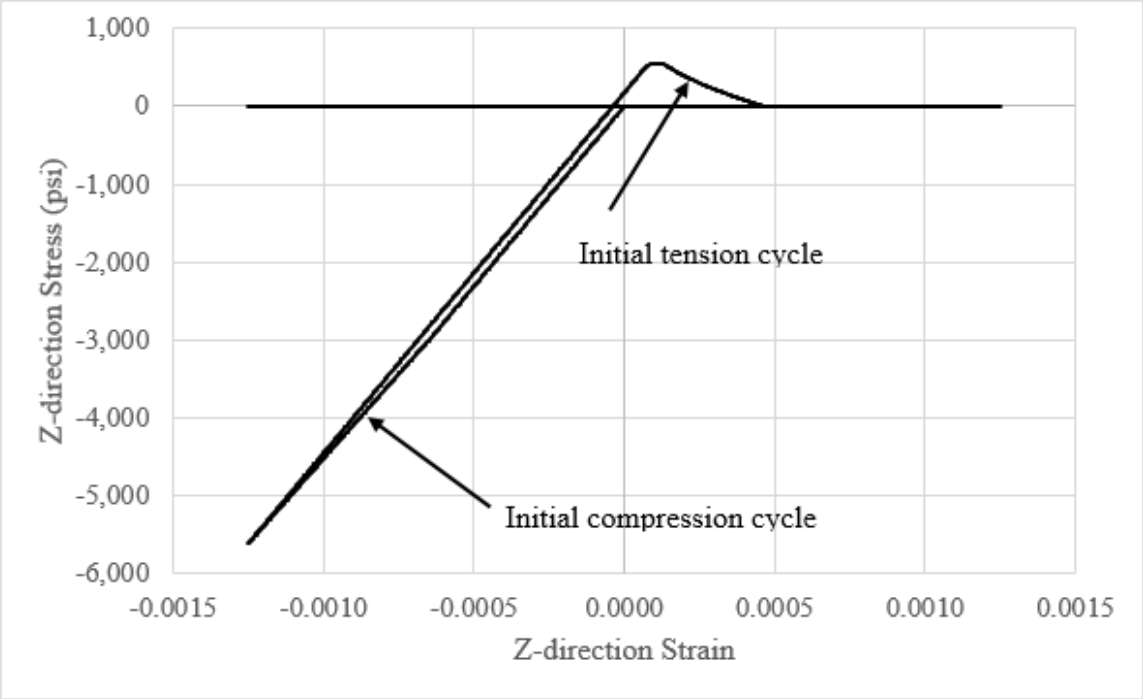

Figure 3-32: KCC – Cyclic compression-tension results

The results for the Winfrith concrete model are presented in Figure 3-33. While the model does not capture strength degradation or stiffness degradation (see previous discussion regarding Figure 3-28) the overall path of the response appears reasonable. That is, as successive cycles are applied to the element, the element is not loaded into compression until it has reached a strain corresponding to the plastic strain calculated for the previous cycle. Additionally, the tensile capacity predicted by the model is limited to the previous minimum capacity predicted on previous cycles (i.e., once the tensile capacity of the material has been reduced to zero, the model will limit the tensile capacity to zero on all successive cycles). Note that this limit to the tensile capacity does not appear to affect the compressive capacity.

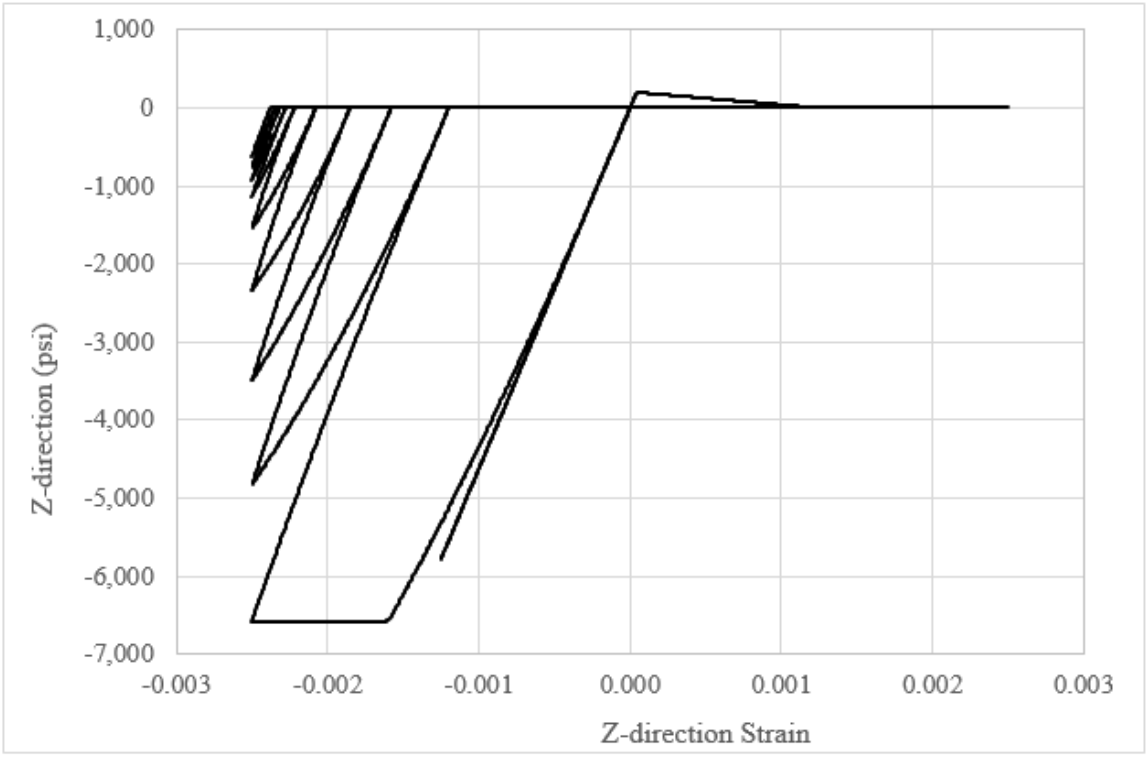

Figure 3-33: Winfrith – Cyclic compression-tension results

Results for the CSC model, defined with *ELFORM 1* using both a viscous hourglass control and stiffness hourglass control, subjected to the cyclic -compression-tension test are shown in Figure 3-34 and Figure 3-35, respectively. Note that the initial shape of the hysteresis curves are identical regardless of specified hourglass control. The hysteresis based on the stiffness hourglass control shows one iteration of stiffness degradation but repeats for the remaining simulation cycles. Note that if compressive strain is increased in a subsequent cycle, the reloading stiffness is again reduced; however, if this new compressive strain is repeated, the model will again follow the same path. The hysteresis based on the viscous hourglass control shows constant stiffness degradation even when the same strain cycle is repeated.

The loading and unloading behavior between the two models is identical aside from the before previously mentioned differences in stiffness degradation. As expected, once the concrete has cracked and reached zero tensile capacity, the formulation produces zero tensile capacity for the remainder of the simulation. However, unlike the KCC model, the CSC model includes separate tensile, or brittle, and compressive, or ductile, damage variables to ensure that the compressive capacity of the concrete is preserved even after cracking has occurred. The second compressive cycle follows an elastic-plastic path, where the transition point between the two behaviors corresponds to the initial curve's elastic deformation limit (marked with the elastic-plastic transition line).

While the described reloading shape appears reasonable, the start of the reloading path does not seem to capture what would be expected in plain concrete. To better understand this inaccuracy, consider a physical concrete cylinder that has been loaded in similar means to the single-element test being described in this section. Once the cylinder has cracked, a physical gap will open between the two pieces of concrete. This gap will expand until the specified displacement has been reached, at which point the subjected displacement will change directions. While it's clear in the physical example that gap between the two pieces of concrete must be closed prior to the concrete being loaded in compression, the numerical model suggests that concrete is almost immediately loaded in compression. It appears that the CSC formulation fails to capture any sort of crack width that may be introduced during the tensile phase of loading.

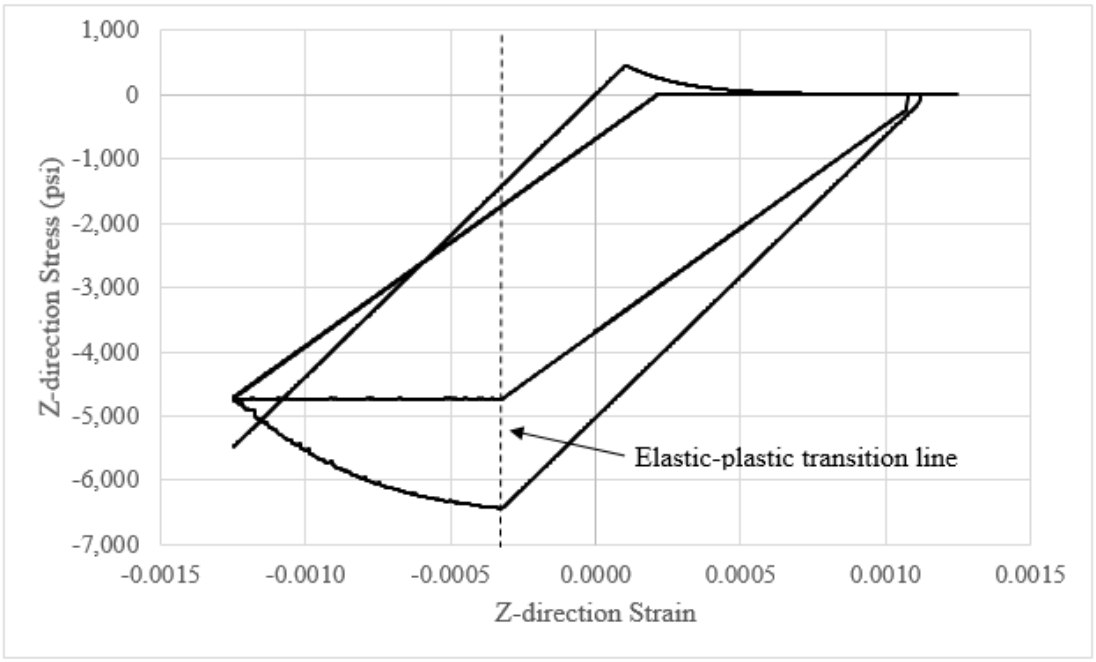

Figure 3-34: CSC – Cyclic compression-tension results – *ELFORM 1* SHG

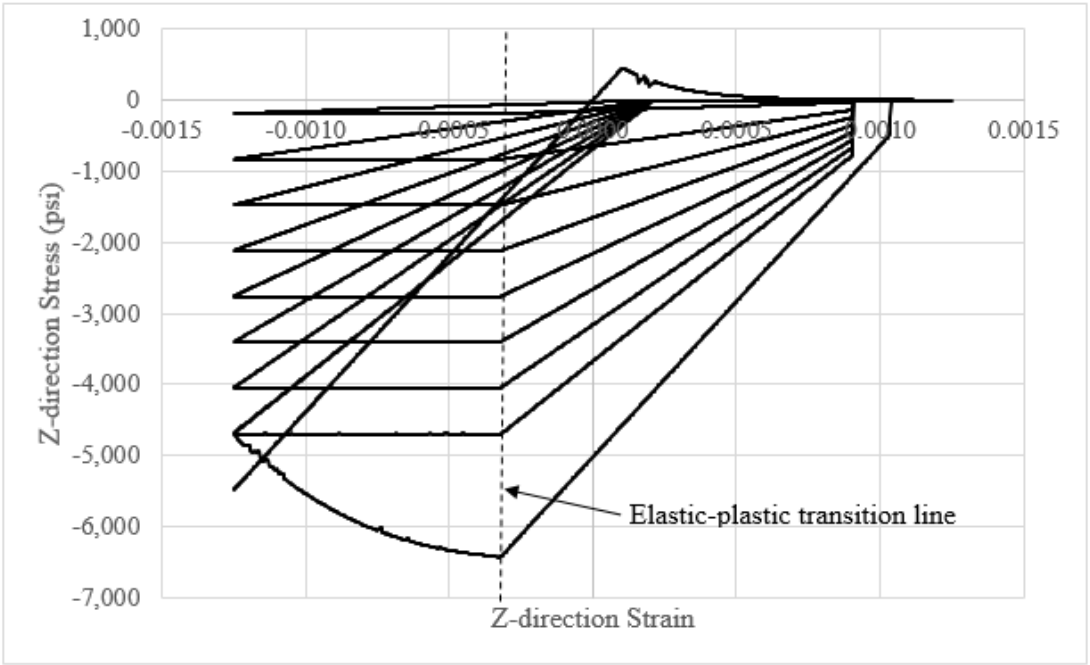

Figure 3-35: CSC – Cyclic compression-tension results – *ELFORM 1* VHG

Finally, Figure 3-36 presents the results for the RHT model subjected to the cyclic-compression-tension test. The cycles within the RHT model progress relatively simply as compared to the CSC model. Both compressive and tensile stresses are unloaded using the initial elastic slope. Reloading follows this same slope until the point of previous maximum stress has been achieved. At this point, the capacity is reduced using a continuous shallow slope. Once the tensile capacity has reached zero, the model enters one last cycle before being limited to zero capacity for both tension and compression. As with the CSC model, the RHT model exhibits the same crack width limitation. That is, the concrete is considered to be actively reloading in compression prior to the expected physical crack width being closed.

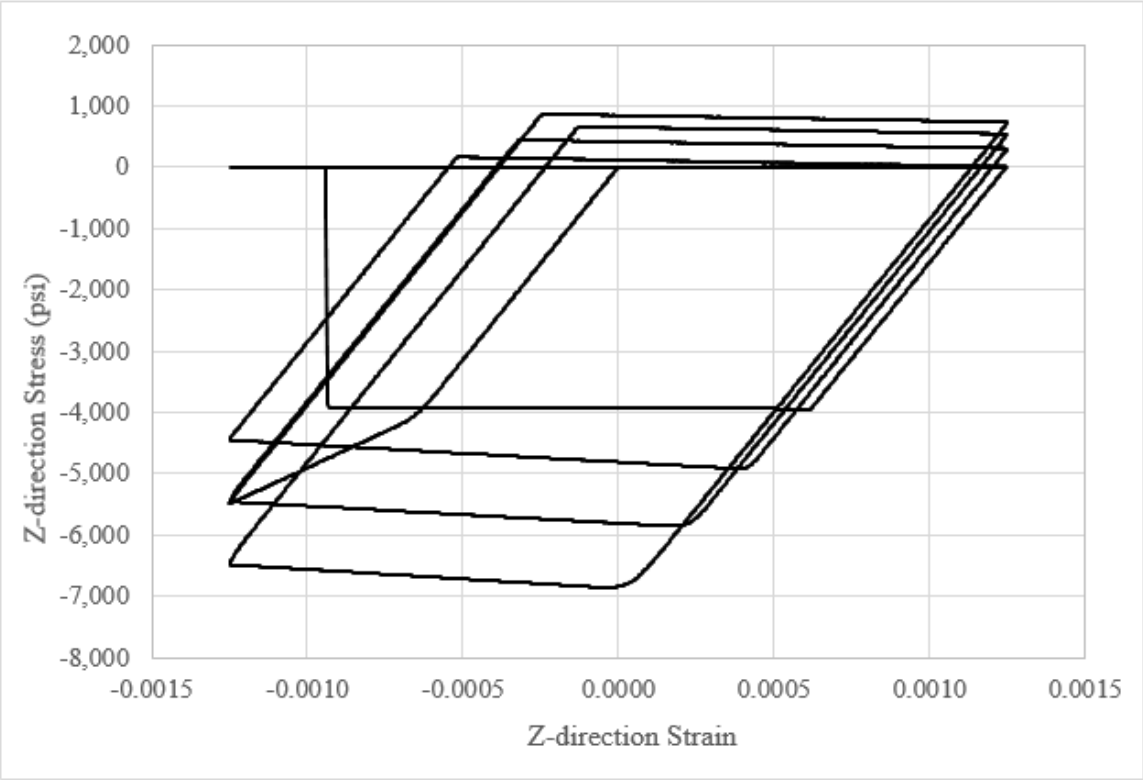

Figure 3-36: RHT – Cyclic compression-tension results

3.5 SINGLE-ELEMENT CLOSING REMARKS

As is apparent from the discussion presented in this chapter, significant attention has been given to the single-element response of the various material models under consideration for this research. Again, the goal of this chapter was to take the various material models through a set of strategically designed load paths in order to identify the strengths and weakness associated with each material model when tasked with capturing concrete's behavior under seismic loading. It is critical to understand the fundamental single-element level response of each material model prior to the progression of a multi-element model. Once additional elements are introduced, it becomes extremely challenging to identify specific strengths and weaknesses associated with the different material models, because behavior is dependent on a significantly higher number of variables.

Section 3.2 detailed the results of three separate parametric studies: (1). element formulation and hourglass control, (2). element size, and (3). strain rate.

The element formulation and hourglass control study demonstrated the importance of defining these two variables as well as the importance of documenting this choice in subsequent study (as the choice can dramatically alter the generated numerical results with all other definitions remaining constant). The study suggests that as a general recommendation, the users define all elements using *ELFORM 1* with a corresponding viscous hourglass control. While other formulation and hourglass control combinations may work for various cases, the *ELFORM 1* and viscous hourglass control definition combination appears to most consistently produce expected behavior. Additionally, this test demonstrated the limitations associated with using the Winfrith and RHT models for modeling simulating unconfined uniaxial compression (e.g., the Winfrith model uses an elastic-plastic path and the RHT model over-predicts the user -specified concrete strength).

The element size parametric study demonstrated the importance of the mesh size as it applies to the rate of exhibited softening in compression. While the Winfrith and RHT models consistently generated results independent of element size, the KCC and CSC models showed stunted stiffness degradation as the element size was reduced. Users should be sure to note that when using these models, as the element size approaches roughly 1inch, the exhibited behavior becomes effectively elastic-plastic. This effect can be mitigated in the KCC model by manually defining an element size scaling parameter. Additionally, note that when using the KCC model, the minimum element size should not be less than three times the aggregate size used in the material definition.

The strain-rate study presented each material model's capacity to handle the spectrum of strain rates associated with seismic loading. The CSC and RHT material model's appeared to best capture the expected strain rate scaling presented in Figure 2-4. While the KCC model also showed the ability to capture strain-rate effects, it appeared that there was a discrepancy between manually defined DIF values vs strain rate curve and the exhibited scaling. While the Winfrith model definition does have a strain-rate enhancement option, this option appeared to generate instability in the single-element model. Therefore, it is recommended that the users not activate this feature. Finally, note that a DIF versus strain rate curve should be included in the KCC material definition regardless of expected peak strain rate in order to avoid an apparent instability associated with slow strain rates.

Section 3.3 detailed the results of the shear study portion of this thesis. This study was conducted in two steps as is customary with indirect shear studies. The unconfined uniaxial tension portion demonstrated each model's capability to accurately capture tension stiffening effects, while the compression softening portion demonstrated each model's capability to capture concrete's behavior when subjected to compression-tension biaxial loading. Aside from the RHT model's tendency to over-predict the shear strength of the

concrete, each model appeared to exhibit adequate agreement with the presented theoretical models.

Finally, Section 3.4 detailed the results of the single-element cyclic loading study. This portion was comprised of two subsections: (1). cyclic compression cycles and (2). cyclic compression-tension cycles.

The cyclic compression cycle subsection demonstrated how the limitations associated with the Winfrith and RHT models, subjected to monotonic compression, also extend into cyclic loading. Because the Winfrith model follows an elastic-plastic path, it does not have the capability of capturing strength degradation. Similarly, the RHT model's gross over-prediction of strength and slow rate of softening severely limit the model's ability to accurately capture strength degradation. Additionally, the model CSC model was shown to be the only model that can capture stiffness degradation.

The second subsection, cyclic compression-tension cycles, demonstrated several fundamental flaws associated with the KCC, CSC, and RHT models. As shown in Figure 3-33, release three of the KCC model cannot capture successive cycles of compression and tension. As such, this material model is not recommended for seismic applications. While the CSC and RHT models maintain strength when subjected to successive cycles, they do not accurately capture crack width. This means that elements assigned this material definition can potentially be subjected to resist substantial compressive loads even when the physical specimen has cracks that have not yet closed.

As discussed in Chapter 2.3, effective validation studies address both single-element and multi-element performance. Chapter 3 illustrated the four concrete material models' performance as applied to a single-element models. Chapter 4 aims to evaluate the behaviors discussed in this Chapter in a multi-element context.

Chapter 4: Multi-Element Analysis and Evaluation

4.1 An Introduction to the Multi-Element Validation Phase

As discussed in Chapter 3, single-element models can be used to demonstrate particular strengths and weakness exhibited by material models when subjected to idealized load paths. This information is vital as it can provide users with insight into potential underlying sources of erroneous behavior. Without also running multi-element simulations, however, it can be difficult to predict the magnitude of system-level error that these discrepancies, identified in the single-element validation phase, may cause. For instance, the Winfrith model's representation of concrete as elastic-perfectly-plastic poorly fits experimental data when considering a single-element; however, it is unclear how much this oversimplified concrete behavior may affect the performance of beams subjected to cyclic loading. While it is important to understand the isolated strengths and weaknesses of the various material models, understanding system-level performance is just as vital to the overall material validation process, and is perhaps more directly beneficial to structural engineering applications.

The multi-element validation phase presented in this chapter is comprised of two simulations: (1). concrete cylinders under cyclic compression and (2). cyclic beam bending. Test one, the concrete cylinder under cyclic compression, was selected to show how a group of concrete elements behaves under cyclic compression. While this analysis has already been performed for the single-element study, repeating the analysis using multi-elements is an important step into understanding system-level cyclic performance. Test 2, the cyclic beam bending problem, has been selected as a means to perform a system-level validation. That is, this case examines a problem that may be encountered in professional practice.

As previously discussed, numerical results are driven by a collective group of definitions rather than just the material model definition. This observation is more so the case with multi-element models because they introduce even more variables and assumptions into the model assembly process than the single-element models. As such, every effort has been made to record the main assumptions made throughout each model's development to provide the reader with a comprehensive understanding of inherent assumptions included within the study. In summary, the hope is to provide the reader with additional confidence in the model and to improve the reliability and repeatability of the study.

4.2 Cyclic Compression – Concrete Cylinder

4.2.1 Introduction and Means of Validation

Although a single-element cyclic element test was presented in Section 3.4, there is additional benefit to repeating the study using multi-elements. While it would be expected that the stress versus strain results obtained from a pure concrete cylinder would be would be identical, or nearly identical, to the results obtained from a pure concrete element, this assumption should not be taken for granted. As this study demonstrates, geometric considerations can play an important role in the behavior of FE models.

The means of validation for the cyclic compression test comes from results presented by Bhan and Hsu [1998]. As presented in Section 3.4, the experimental study was conducted to support the development of a simple mathematical expression that could accurately represent concrete under a full envelope of cyclic loading. The concrete used within the study was reported to be a normal-weight mix with a maximum aggregate size of 0.375-inch. Note that the actual strength of the concrete was not included in the study, as the results were reported in terms of normalized stress and strain ratios.

4.2.2 LS-DYNA Model Construction

Error! Reference source not found. shows an illustration of the LS-DYNA model used to validate each material model for cyclic compression. Following the recommendations made in Section 3.5, all elements in the model were defined using ELFORM 1 and a viscous form of hourglass control unless otherwise noted. In some specific cases, additional test results are shown to illustrate the effects of a varying element formulation and hourglass control. The gross-geometry of the cylinder, 12 inches tall with a 6-inch diameter, was chosen to match the experimental test setup described in Section 4.2.1. Note that the elements in this section are roughly the size of 1 inch cubes.

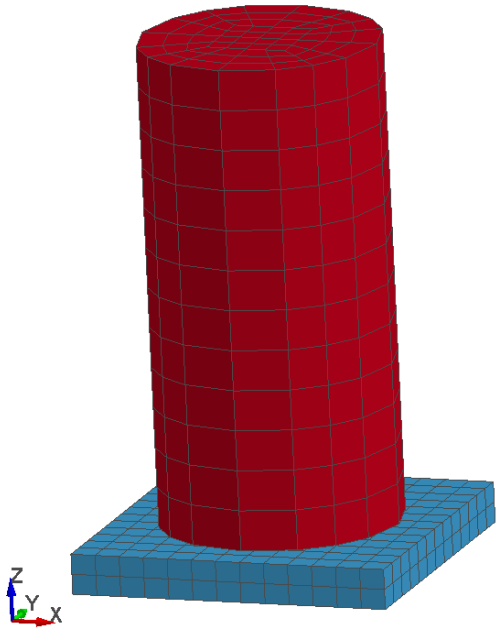

Figure 4-1: Concrete Cylinder FE Model

The bottom plate was modeled using elastic steel elements restrained from translation in all three directions. While there are admittedly several other ways to define a reaction surface (such as a rigid surface), the specific method is not likely to control the

numerical response for this specific test. Originally, a mirroring top steel plate was also defined within the model. This top plate was removed on a later iteration of the model, however, to allow for finer control of the concrete cylinder's displacement. Contact between the steel reaction surface and the concrete cylinder was controlled using the *Automatic_Surface_To_Surface* keycard.

As with the displacement methods described in Chapter 3, deformation was imposed on the model using identical *z*-direction displacement curves applied to every node on the top surface of the concrete. The specific displacement curves applied were independently configured for each material model in an effort to mimic the displacement seen during the experimental testing. In essence, the displacement of the model was treated as the independent variable, while the load at each displacement was considered the dependent variable.

4.2.3 RESULTS AND DISCUSSION

This section details the results from the concrete cylinder cyclic compression validation analyses. Note that the numerical results presented in this section can also be compared to those presented in Section 3.4.1 (the single-element version of this test). The results in this section, however, correspond to 1-inch general hexahedra elements, while the single-element version of the test corresponds to 4-inch cube elements. While the two tests should theoretically exhibit similar behavior, reducing the element size may have influence on the post peak scaling, as demonstrated in Section 3.2.2.

Figure 4-2 shows the results from the KCC concrete cylinder cyclic compression study. Note that because element size varied throughout the mesh, the *b1* factor previously discussed in this thesis was not included in the material definition. The KCC model, implemented with multi-elements, was nearly identical to the experimental results up to

the transition between elastic and inelastic response. The post-peak behavior, however, showed a slight deviation between the numerical results and the experimental results. Although the KCC model did not capture stiffness degradation, as consistent with the results presented in Section 3.4.1, the response was reasonably consistent with the experimental results.

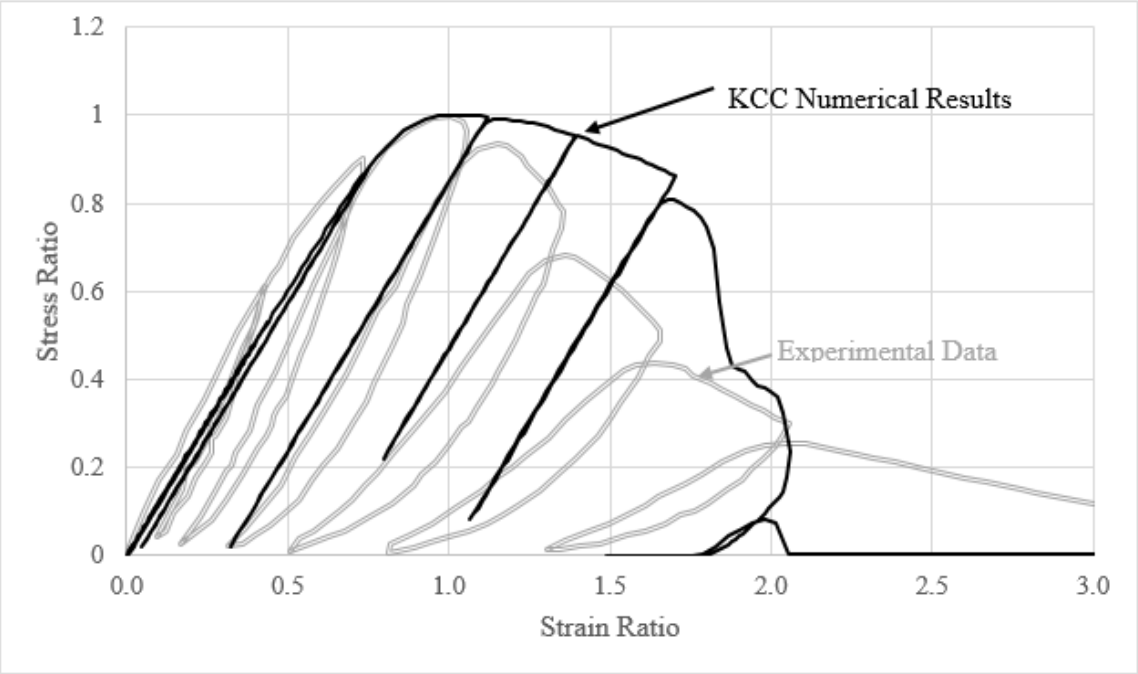

Figure 4-2: KCC Cyclic Compression – Concrete Cylinder

Results from the Winfrith concrete cylinder compression validation are shown in Figure 4-3. Unlike the KCC model, the results from the multi-element Winfrith model were not consistent with those predicted by the single-element test shown in Figure 3-28, nor were they consistent with the experimental results. Results up to the elastic limit appear reasonable; however, the exhibited post-peak behavior does not agree with what is expected. It appears that the cylinder exhibited some post-peak softening, an interesting phenomenon considering each individual element has an elastic-perfectly-plastic behavior.

Thus, individual elements do not include any post-peak softening even though such behavior is observed for the multi-element model. Additionally, while the concrete does appear to capture some stiffness degradation, there are portions of the post-peak loading and unloading curves that have a slope of zero. Again, this does not follow the anticipated response, and it is unclear as to why such behavior occurs. Further investigation showed that the elements across a cross-section taken at mid height of the cylinder had stress histories which varied in post peak behavior. Some of these elements maintained capacity and did not soften over the displacement cycles while others appeared to lose all capacity regardless of imposed displacement.

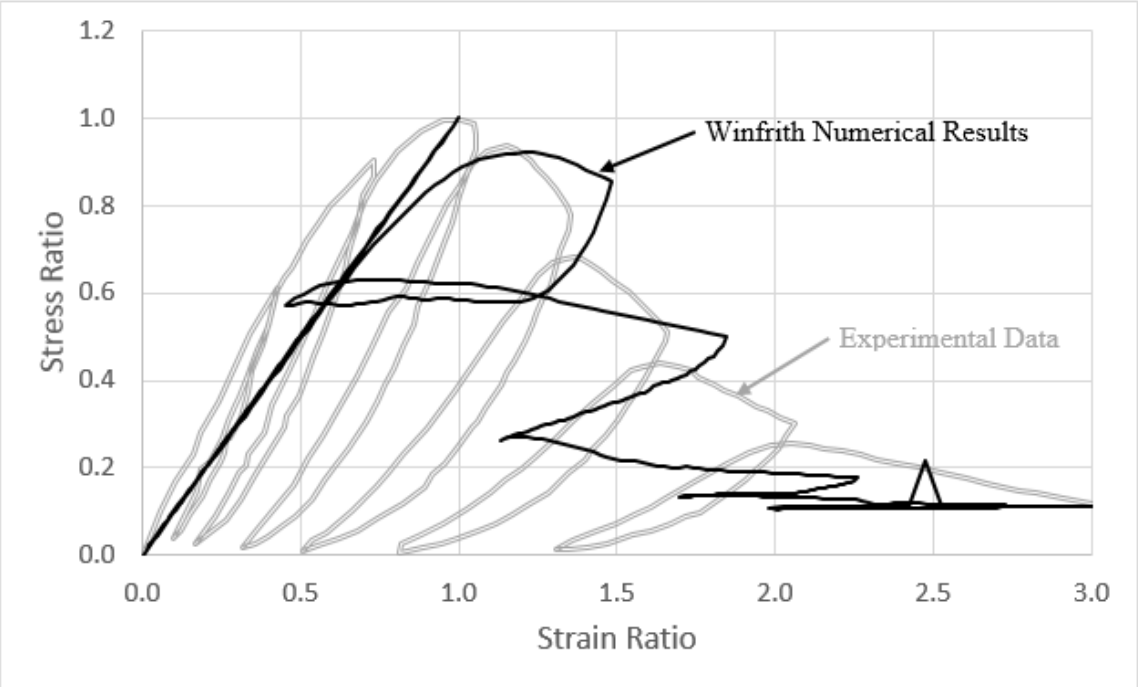

Figure 4-3: Winfrith Cyclic Compression – Concrete Cylinder

The CSC concrete cylinder compression results are shown in Figure 4-4. As with the KCC model, these results are reasonably consistent with the single-element results. One

small difference is that the multi-element test exhibited a faster rate of softening as compared to the single-element test. While the inconsistency is worth noting, post-peak behavior is unpredictable and some variation in softening rates is tolerable assuming the capacity and general trends of the behavior are not compromised. Overall the multi-element CSC model was able to capture stiffness degradation and showed good agreement with the experimental results.

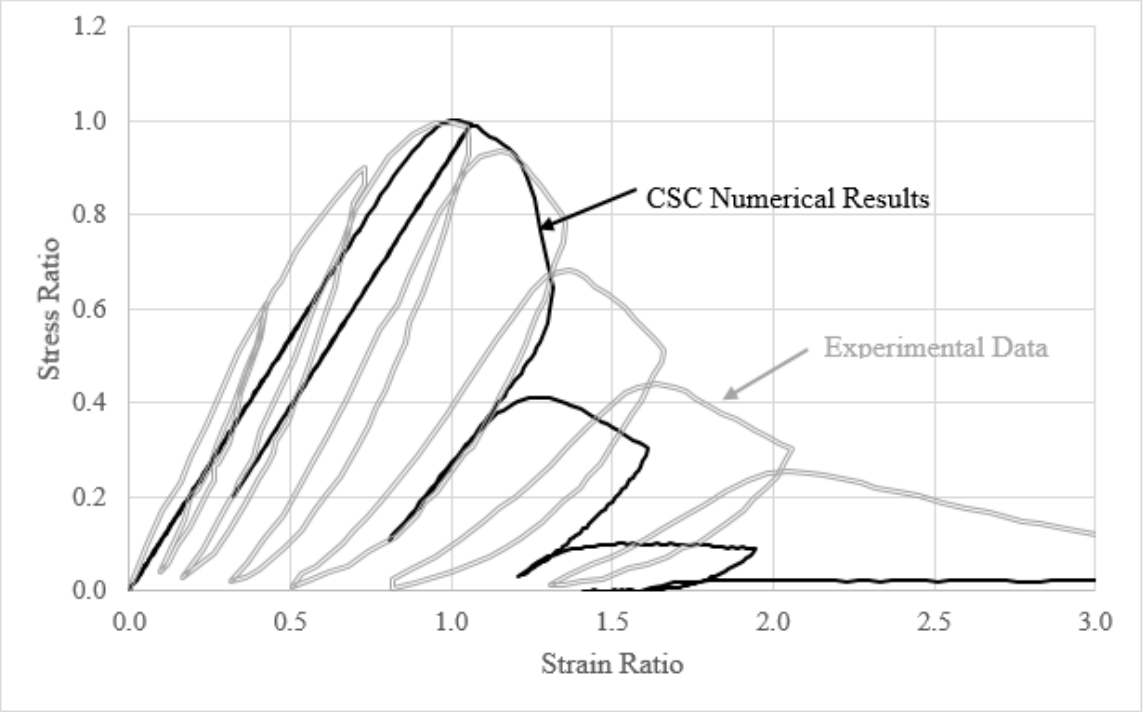

Figure 4-4: CSC Cyclic Compression – Concrete Cylinder

Lastly, the RHT concrete cylinder compression results are shown in Figure 4-5. Once again, the multi-element results appear nearly identical to the single-element results as expected. The RHT constitutive model still does not show a capability to capture stiffness degradation, and it over-predicts capacity at high strains. Overall, the model's accuracy is with regards to capacity, strain at peak capacity, and softening rates are inferior to the CSC and KCC models and poorly align with experimental results.

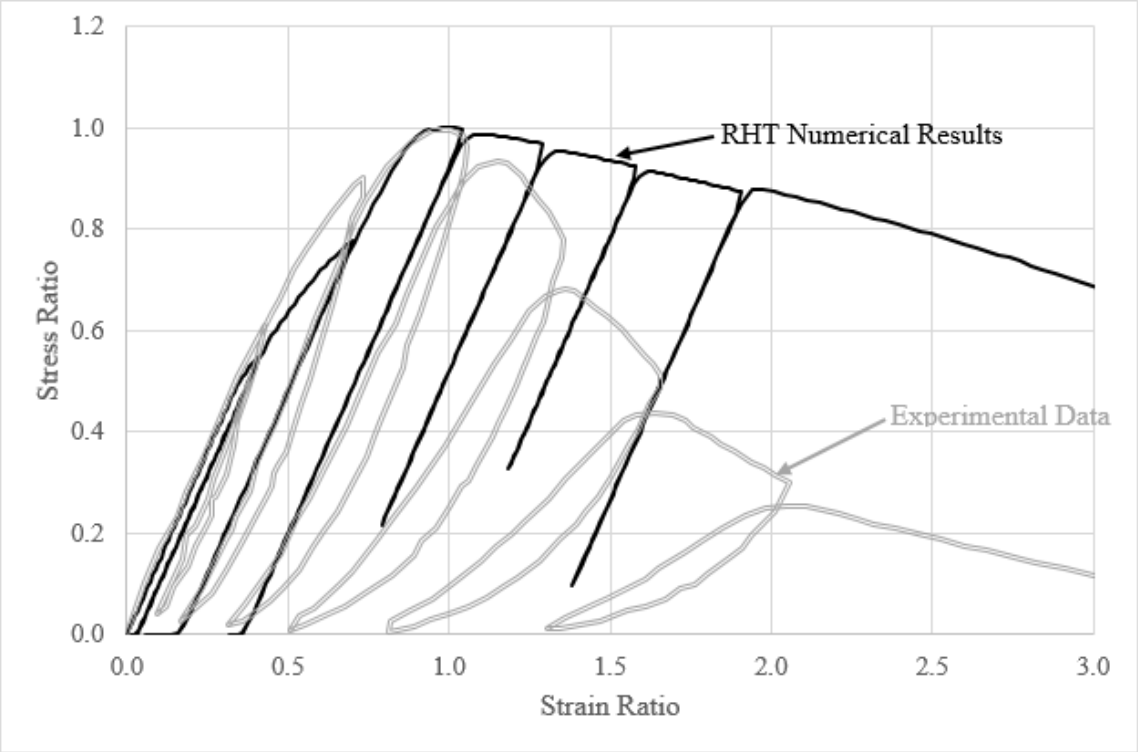

Figure 4-5: RHT Cyclic Compression – Concrete Cylinder

4.3 Cyclic Beam Bending

4.3.1 Introduction and Means of Validation

The final and most complicated scenario considered in this thesis is the cyclic bending of a reinforced concrete beam. Though the single-element studies and concrete cylinder study are important background investigations that have yielded important findings about idealized stress paths, this final study has direct application to LS-DYNA users. The test encompasses a shear component, a cyclic component, and a load reversal component, all in a multi-element setting that appeals more to actual applications than just an academic exercise (as could be said about a majority of the single-element study).

Before presenting details of the physical experiment and numerical model, it is helpful to revisit the purpose behind this specific exercise. Echoing the discussion consistently made to this point, the purpose of this work is to demonstrate each material model's capability to model cyclic response. In the context of the cyclic beam bending problem, this means identifying and discussing key trends in the results is paramount, while capturing every last complexity of the physical experiment and exactly replicating the results is less of a concern. Therefore, while effort has been made to reasonably capture the behavior of the beam such that key trends are consistent between the numerical results and experimental results, simplifications have been made and some level of error has been tolerated. In summary, demonstrating important trends such as stiffness degradation, capability of load reversal, and pinching of the hysteresis are the emphasis more so than replicating the exact capacity and stiffness of the beam through modeling such behaviors as rebar slip or reinforcement strain hardening.

Experimental validation for this test was taken from a study conducted to investigate cyclic response of concrete beams reinforced with plain bars [Marefat et al., 2009]. While plain bar reinforcement was the main focus of the study, the investigation also included two control tests run on members reinforced with deformed bars. Figure 4-6 shows the test setup used in the Marfat study. The test was conducted by imposing a series of displacements designed to load the specimen to progressively higher drifts. Note that the imposed displacements are defined in terms of drift ratio (end displacement normalized by the height of the beam). The yield drift ratio for the specimen considered in this thesis was recorded as 1.84% in the push direction and 2.3% in the pull direction.

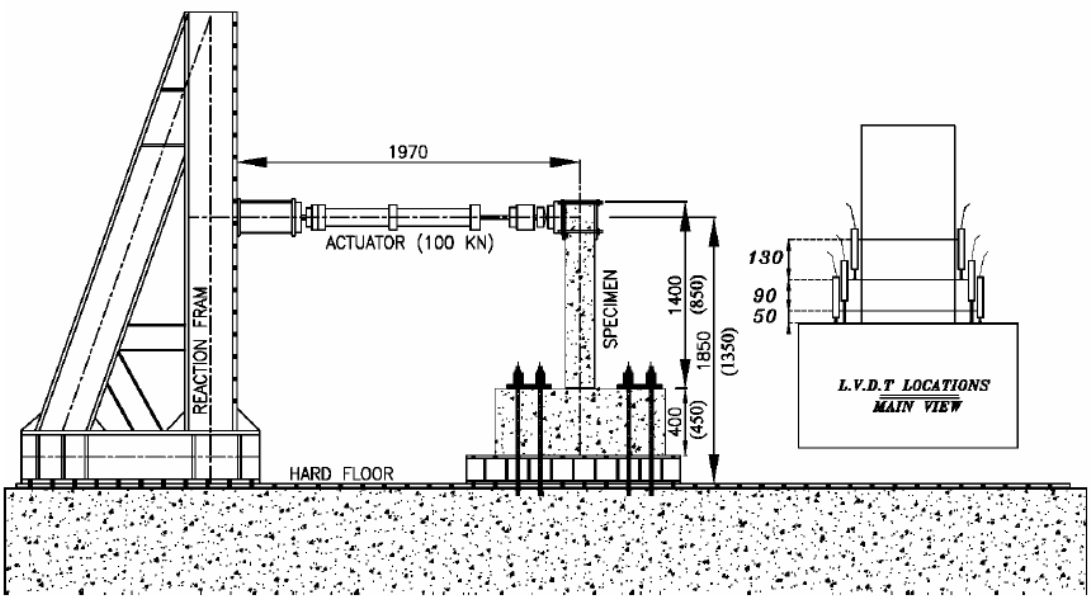

Figure 4-6: Cyclic Beam Bending Experimental Test Setup [Marefat et al., 2009]

Figure 4-7 details the dimensions and reinforcement layout for the test specimen used for validation in this thesis. This specific specimen was identified as the best candidate for the multi-element validation study because it was reinforced with deformed rebar and had substantial transverse shear reinforcement (hoops spaced at $<d/4$ in the plastic hinge region) [Marefat et al.,2009]. These two factors are advantageous to this thesis because they simplify the modeling process. Deformed bars are significantly easier to include in a numerical model than plain bars because even though some slip is expected, it is not unreasonable to assume a perfect bond between the rebar and concrete. Additionally, adequate transverse reinforcement encourages simpler flexural failure modes as opposed to the more complicated shear failures or longitudinal bar buckling failures that are often associated with minimal transverse reinforcement. These simplifications reduce the complexity of the model and emphasize the importance of concrete material behavior.

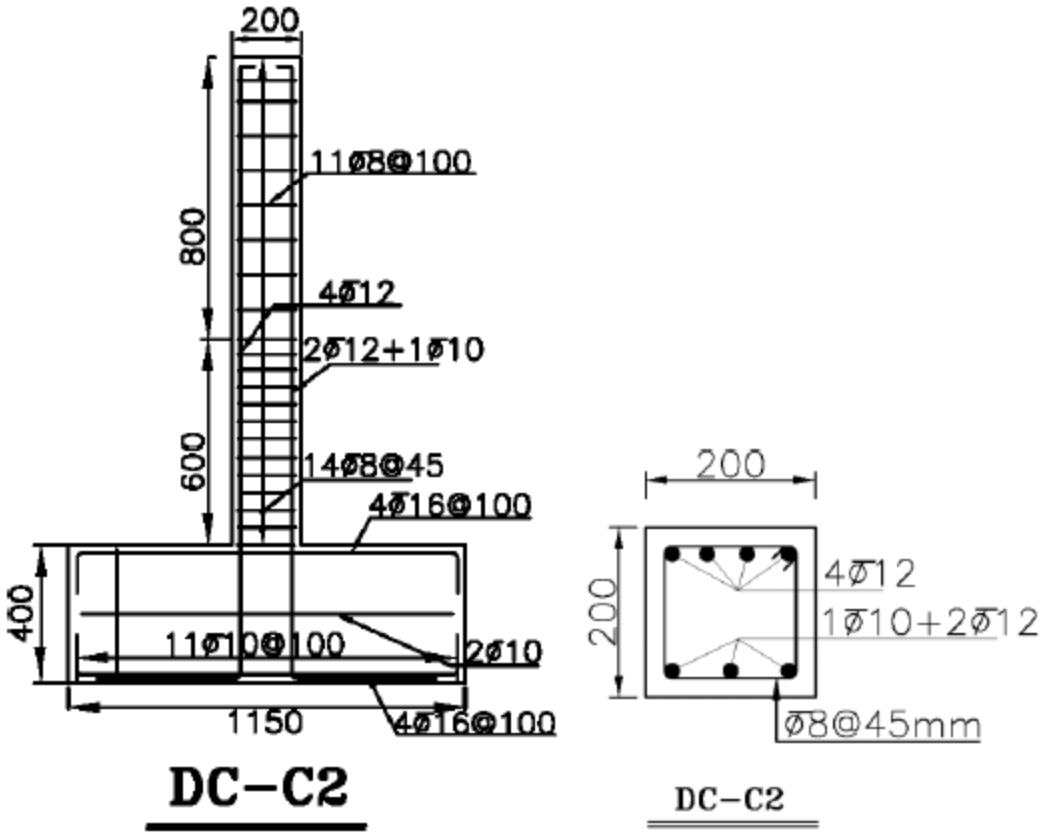

Figure 4-7: Reinforcement layout for specimen DC-C2 [Marefat et al.,2009]

Basic material properties for specimen DC-C2 are provided in Table 4-1. Note that the Marefat et al. study does not document transverse reinforcement material properties, nor does it provide any information regarding the aggregate size used in the concrete mix design. These two assumptions are discussed in Section 4.3.2. The experimental results of the study are presented in Figure 4-8.

Table 4-1: Specimen DC-C2 material properties

Concrete	Longitudinal Reinforcement			
f'_c	f_y	ε_y	f_u	ε_u
3340	59800	0.0017	74000	0.18

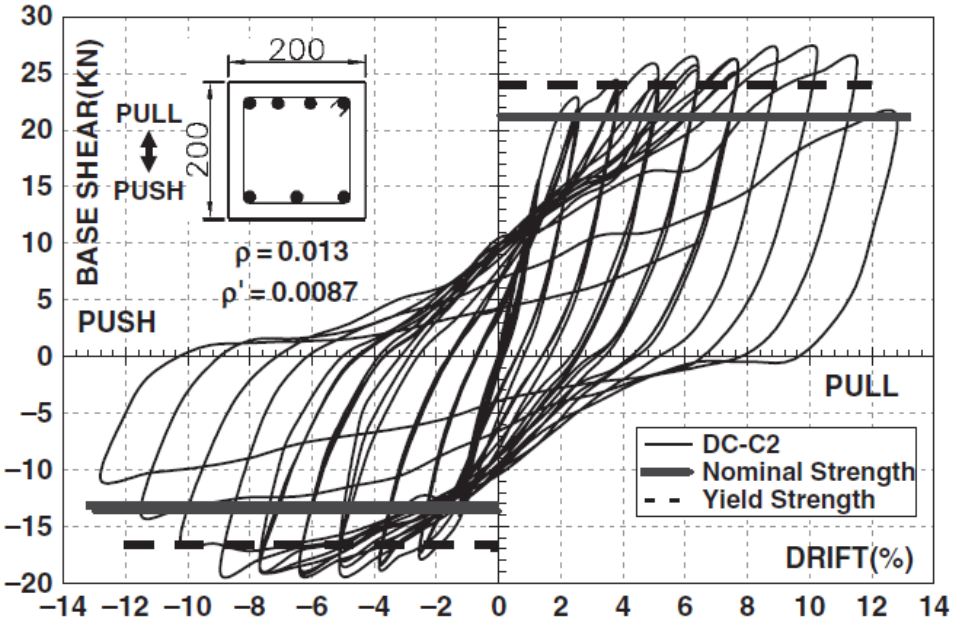

Figure 4-8: Experimental Beam Bending Results [Marefat et al.,2009]

4.3.2 LS-DYNA Model Assembly

To improve the repeatability of this study, every effort has been made to record the definitions and assumptions made throughout the modeling process. Specific keycard definitions are provided in Appendix A. Figure 4-9 shows a rendering of the final FE model used to obtain the results presented herein.

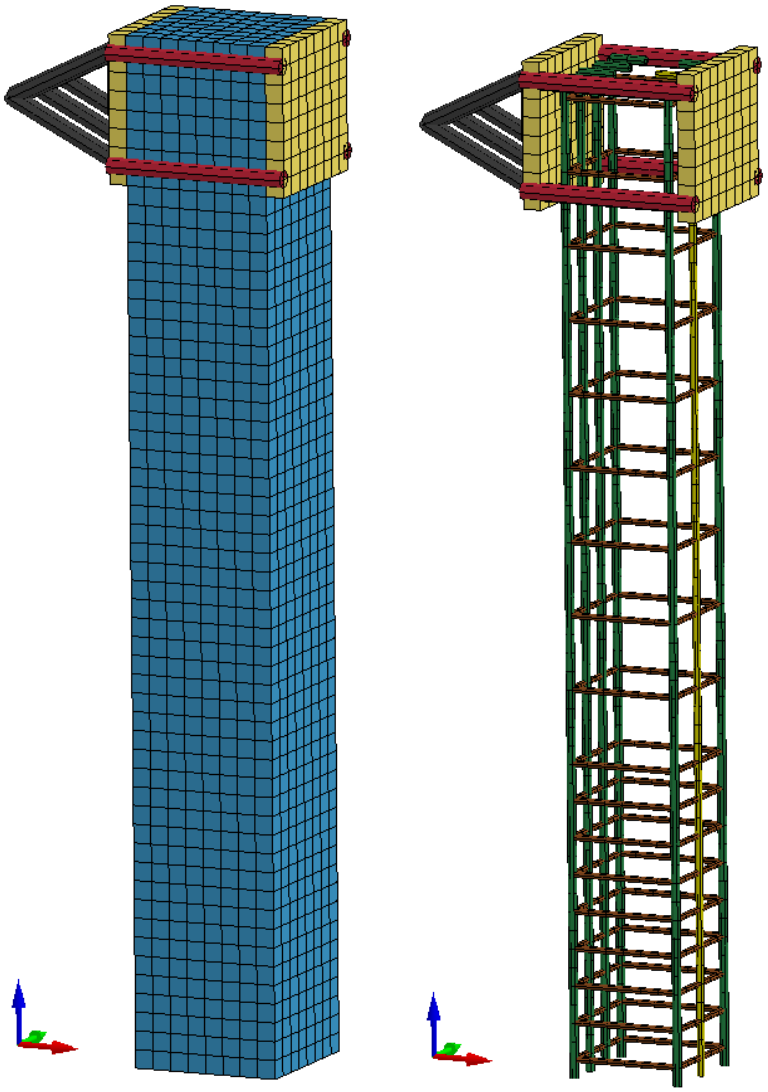

Figure 4-9: Cyclic Beam Bending FE Model

Although the experiment dimensions were documented in metric units, the numerical model was constructed using English units (inches, psi, etc.). This choice was made to preserve consistency with the previous models presented in this thesis. The gross dimensions of the numerical model were defined to match those listed in the experimental documentation. Key dimensions include a beam height of 55 inches, a beam width and

depth of 8 inches, a longitudinal reinforcement depth of 1 inch, and shear hoop spacing of 2-inches within the flexural plastic hinge region and 4-inches over the remaining height of the beam.

The concrete beam was meshed using 1 inch by 1 inch by 1 inch brick elements. This mesh was selected because it conveniently matched the gross dimension of the beam and generated nodes coinciding with the location the rebar. Both the flexural reinforcement and shear reinforcement were modeled using 1-inch long beam elements. Because deformed rebar was used in the experimental test, a perfect bond was assumed between the concrete and reinforcement. This perfect bond was modeled by merging the nodes of the rebar cage with the coinciding nodes of the concrete brick element mesh. While in reality there was likely some amount of slip between the reinforcement and concrete, this minimal slip was not expected to impact the outcome of the test in a significant way. Additionally, merging reinforcement nodes to concrete mesh nodes has been established as common practice for modeling reinforcement within reinforced concrete numerical models [Abbas et al., 2010; Adhikary et al., 2012; Chen and May, 2009].

All brick elements were defined using *ELFORM 1*. The beam elements used to model the reinforcement were defined using the default LS-DYNA beam formulation, Hughes-Liu. All reinforcement was defined using a circular cross-section, matching that documented in the experimental test.

Both the flexural and shear reinforcement were modeled as elastic-perfectly-plastic based on the yield stress from the experimental documentation presented in Table 4-1. The various concrete models were defined using the unconfined compressive strength from the experimental documentation, again listed in Table 4-1. The mix aggregate size was not documented, which required an assumption to be made. As such, 3/8-inch aggregate was

selected to limit the chance of numerical instabilities associated with the concrete brick-to-aggregate ratio within the numerical model.

The boundary conditions applied during the experimental test were not well documented; therefore, several assumptions were made during this portion of the modeling process. These assumptions have the potential to significantly impact the results of the numerical model; however, as previously discussed, this validation does not aim to replicate the exact results of the experimental test, but rather demonstrate the strengths and weaknesses of the implemented concrete material formulations.

The bottom boundary condition used in the experimental test can be seen in Figure 4-9. Note that the base block has not been explicitly modeled. Rather, idealized fixed constraints have been applied to the bottom surface of the beam. In the experimental study, it appears that the base block has been clamped to a strong floor using tie rods that have likely been post tensioned to prevent any slip from occurring along the interface formed between the base block and the strong floor. This setup would also limit deformations over the height of the block. Additionally, the longitudinal bars have been adequately developed into the base block, meaning that significant slip of the longitudinal bars is not expected to occur. Because of the perfect bond assumed between the rebar and concrete during the modeling process, this slip would not be captured anyway. Therefore, the only perceived advantage of modeling the base block is to capture localized failures around the interface formed between the base block and beam. While this behavior may be critical for capturing an anticipated shear failure, it is less important for capturing a flexural failure. Furthermore, the results presented in Section 4.3.4 do not indicate a need for further detail at this boundary condition. Thus, it is reasonable to assume the base of the beam is fixed.

The top boundary condition used in the experimental test and numerical simulation is shown in Figure 4-10. All discussion surrounding the experimental load application

suggests the use of a hinge between the actuator and reaction plates, allowing the beam to freely rotate. Again, it appears that tie rods have been used to clamp the reaction plates to the beam to ensure that the far side of the beam is engaged during pull cycles. The load application apparatus has been modeled using a series of three parts consisting of (1). a load hinge, (2). reaction plates, and (3). tie rods.

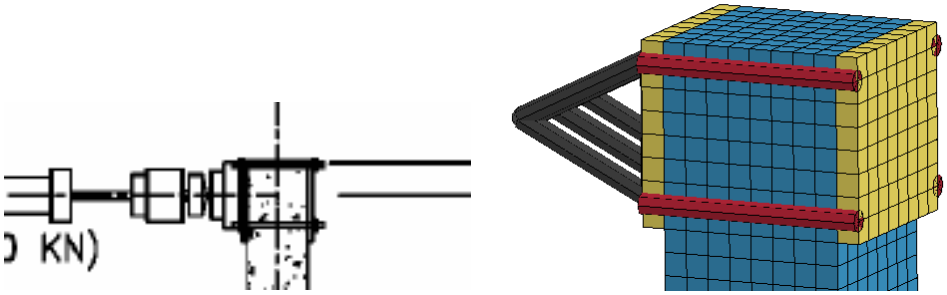

Figure 4-10: Experimental and modeled top boundary condition

The load hinge was designed to allow an imposed displacement curve to be applied on the horizontal plane while leaving the beam's rotational degree of freedom unrestricted. Both the tie rods and reaction frame were modeled using rigid truss elements, and the reaction plates were modeled as elastic bricks with a stiffness that prevented deformations of more than 1%. To simulate the clamping force in the tie-rods, the reaction plates were merged to the coinciding concrete beam nodes. This assumption also served to limit artificial high-frequency noise between the two interfaces.

The final component of the numerical modeling process was defining a displacement curve that mimicked the displacement imposed during the experimental investigation. The word curve is important here because it implies displacement's relationship to an additional variable, which in this case is time. Note that the physical experiment was run as a quasi-static test where the displacement was imposed over such a

long time frame that displacement's relation to time became insignificant and was not recorded (i.e., inertial effects did not influence the response). This poses a problem for an explicit code such as LS-DYNA, which was originally developed to solve high-rate of loading problems. Although LS-DYNA does have implicit capabilities, the implicit solver does not support the CSC or RHT concrete models, making this analysis approach unsuitable for this particular study.

Simulating a quasi-static test using explicit software must be approached carefully, as dynamic problems introduce inertia into the governing equilibrium equations. Ideally, the explicit simulation would be run over a large time span (like the experimental test) to reduce the magnitude of such inertial forces, thus negating any influence they may have on the problem. Explicit solvers are conditionally stable, however, and require a small time step, typically on the order of 1E-6 seconds. This time step varies depending on the simulation parameters and can be artificially inflated through a process known as *mass scaling*. Because mass is directly proportional to the generated inertial forces, however, mass scaling can potentially cause more harm than good in "quasi-static" simulations. Generally, running an explicit simulation for more than a few seconds is difficult considering the heavy computational demands. Therefore, a balance must be struck between acceptable inertial contribution and acceptable problem run time.

Before devising a means to limit inertial effects, it is necessary to first understand the source of these inertial forces and how they may potentially influence the computed results. Consider the general form of the equation of motion presented in Equation 4-1. In a quasi-static problem, acceleration and velocity are effectively zero, reducing the expression to that presented in Equation 4-2 where the applied force is equal to the product of the stiffness and displacement of the system. When velocity and acceleration are not zero, however, such as the case with the numerical problem under consideration, these two

components contribute to the equation. The "inertial" component is specifically defined as the product of the acceleration and mass of the system. Note that the inertial forces are the main focus of this discussion because the product of damping and velocity is often so small it can be neglected.

$$m\ddot{u} + c\dot{u} + ku = p(t) \qquad \text{Equation 4-1}$$

$$ku = p(t) \qquad \text{Equation 4-2}$$

where m is mass, c is the viscous damping coefficient, k is stiffness, $\ddot{u}$ is acceleration, $\dot{u}$ is velocity, u is displacement, and $p(t)$ is the external force history with respect to time.

The problem can also be approached considering energy. Again, first consider the quasi-static problem. In this case, the only energy in the system is the internal energy that goes into displacing the concrete beam. Once velocity is given a non-zero value, however, kinetic energy also exists within the system.

Accurately modeling the experimental test requires limiting both the inertial components of the system and the kinetic energy within the system. Both of these metrics have been monitored and reported to ensure adequate attention has been given to limiting the generated error that is inherently introduced when a quasi-static system is analyzed using the dynamic equilibrium equations.

The following methodology was implemented to minimize the inertial force and kinetic energy while limiting the problem's run time. Note that the physical experiment being modeled was a displacement-controlled problem; thus, the beam was taken to specifically defined displacements (the independent variable), and the resulting lateral resistance (the dependent variable) was then recorded. This same procedure must be captured in the numerical problem as well and can be accomplished by imposing a displacement, a velocity, or an acceleration curve to the load application apparatus. While displacement, velocity, and acceleration are all interrelated, in that they can be calculated

from one another through integration or differentiation, these processes inevitably involve some degree of numerical error and therefore, imposing a displacement curve produces different results than imposing an acceleration or velocity curve. Before selecting the appropriate application method, it's important to consider the advantages and disadvantages of each method.

Imposing a displacement curve most accurately captures the intended displacement of the test while also introducing the most noise to the applied acceleration curve. This characteristic is important because noise in the acceleration curve means noise in the inertial force contribution. Ideally, the inertial force is held constant throughout the simulation to help reduce uncertainty in base shear results. A constant inertial force is best accomplished through specifying a user-defined acceleration curve. When this method is implemented, however, there is a tendency for the recorded displacements to begin to diverge from the displacements imposed during the experimental test. Additionally, acceleration cannot be directly imposed on a rigid body in LS-DYNA. Recall that the load application apparatus has been defined as rigid. Finally, load application can be defined using a velocity curve. After repeating the FE simulation using the different methods described in this paragraph, using a velocity curve most effectively limited noise in the acceleration curve while limiting divergence from the desired displacement curve. The imposed velocity curve used for the remainder of the simulations is presented in Figure 4-11, and sample resulting displacement and acceleration curves are presented in Figure 4-12. Note that the acceleration curve consists of constant accelerations over specified time intervals that are separated with discrete jumps. This is convenient as it generates constant inertial forces that can be easily monitored.

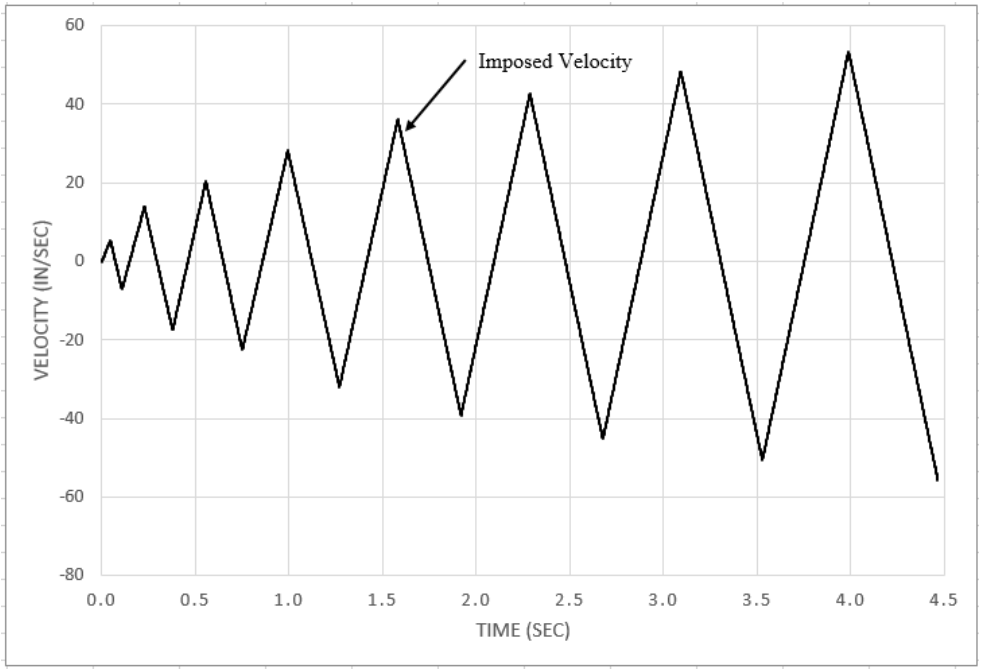

Figure 4-11: Imposed Velocity Curve

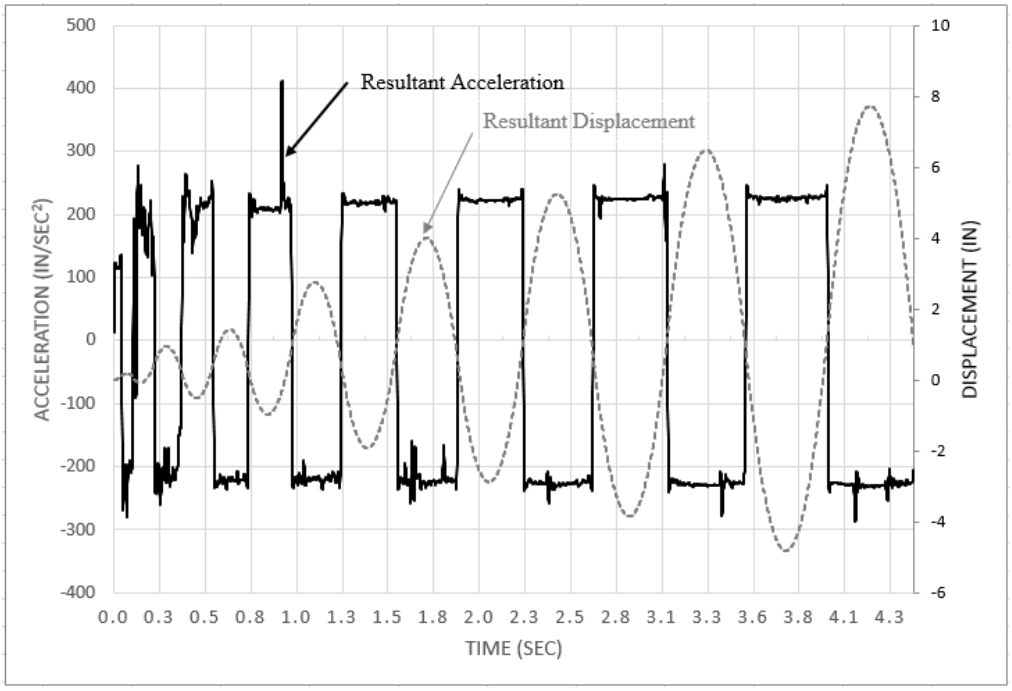

Figure 4-12: Resultant Acceleration and Displacement Curves

To approximate the anticipated inertial force contribution, the system can be simplified to a single-degree-of-freedom problem (SDOF). As part of this simplification, the total mass of the multi-degree-of-freedom (MDOF) system must be converted into an equivalent mass that will participate in the SDOF system. Considering the boundary conditions for the problem under consideration (i.e., fixed-free), [UFC 3-340-02, 2008] Table 3-12 recommends a mass participation coefficient of 0.33 for plastic systems and 0.24 for elastic systems. The 0.33 value is more conservative (as it means more mass is participating and contributing to the inertial load) and will be used for this approximation. This means that a cantilever beam can be approximated as an SDOF system with an effective mass equal to 33% of that in the real system. This calculation is shown in Equation 4.3.

$$m_{eff} = 0.33 m_{phys} = (0.33)\frac{\left(55in \cdot 8in \cdot 8in \cdot \frac{150lbf\ /\ ft^3}{(12in\ /\ ft)^3}\right)}{386.09in/\sec^2} = 0.791\frac{lb \cdot s^2}{in}$$

Equation 4-3

where m_{eff} is the effective mass of the idealized SDOF system and m_{phys} is the mass of the real system.

Assuming a mass participation equal to that calculated using the SDOF system, the inertial force component of Equation 4-1 can be calculated as shown in Equation 4-4. This force represents an approximation of error introduced into the problem by representing the quasi-static experiment with a dynamic simulation. Normalizing this error over the expected base shear taken from the experimental results yields a meaningful approximation of expected error. Experimental peak base shear was reported as approximately 6000-lbs., yielding an estimated error due to inertial effects of approximately 3%.

$$F_{in,\max} = \frac{d^2u}{dt^2} m = 0.791 \cdot A_{\max} = 180lbs \qquad \text{Equation 4-4}$$

Again, because the goal of the validation effort described in this section is to demonstrate strengths and weaknesses of the selected concrete models rather than to replicate the exact experimental results, this level of error is considered to be acceptable.

Figure 4-13 shows an energy plot from the final simulation using the Winfrith model. Note that kinetic energy comprises roughly 0.5% of the total energy of them system. Once again, this level of error is tolerable.

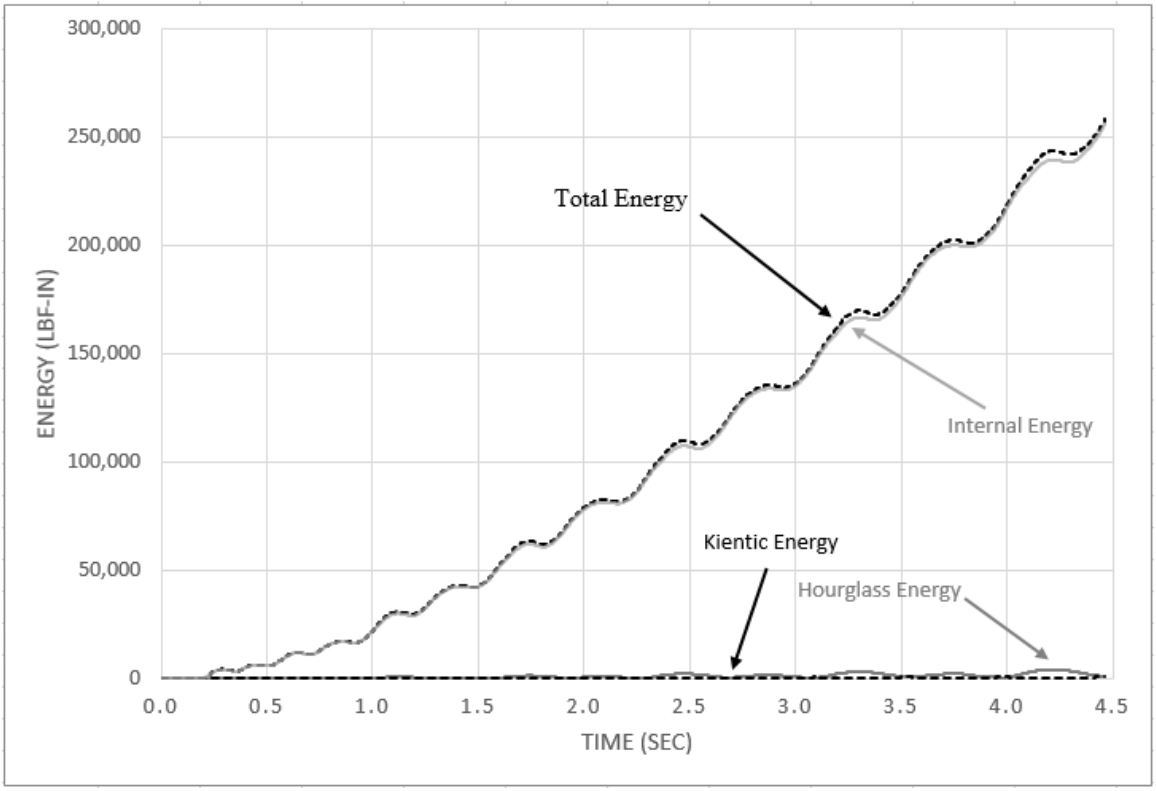

Figure 4-13: Beam Bending Energy Plot

4.3.3 HOURGLASS STUDY

The final portion of the FE model assembly was defining an hourglass control. Initial FE simulations showed significant zero-energy deformation at the base of the beam, as shown in Figure 4-14, when the default LS-DYNA hourglass control was specified. Although the poor results included significant hourglass deformation, or zero-energy deformation, such results can indicate one of a number underlying problems including: (1) improper selection of hourglass control, (2). improper definition of boundary conditions (i.e., the idealized fixity applied to the bottom of the beam is a poor representation of reality and has overly constrained the problem), (3). improper load application, and (4). inadequate mesh refinement (i.e., cracks are smeared over too few elements to accurately capture physical behavior). As a first step in investigating the source of the erroneous behavior, the specified hourglass control was varied, and the results were examined to determine if improper hourglass control was the source of the problem or if additional investigation was necessary.

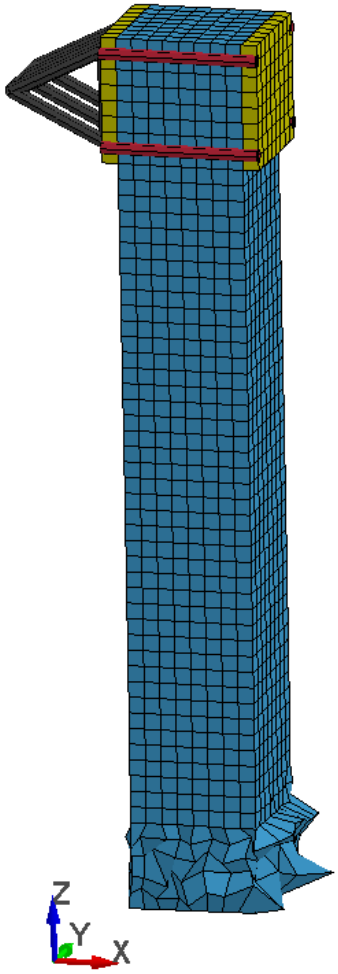

Figure 4-14: Initial Beam Bending Simulations

As discussed in Section 2.2, hourglass control definition is most sensitive to what is called an hourglass control type (i.e., the mathematical formulation used to limit rigid body modes of deformation). To this point, this thesis has focused on the default formulations, including a viscous form (*IHQ 1*), an exact integration viscous form (*IHQ 3*), and an exact integration stiffness form (*IHQ 5*). These same three forms were selected for the scope of the hourglass study to remain consistent with the work presented to this point and because they are perhaps the three most commonly used forms for typical structural engineering problems. Additionally, hourglass control definition requires

specification of an hourglassing coefficient. This coefficient is essentially a weighting factor used in the formulation. For the preliminary hourglass study, this coefficient was defined as 0.1, which was in accordance with the default LS-DYNA recommendation. This parameter can be varied from 0.1 to 0.15; however, numerical error can occur for values exceeding 0.15[DYNA Manual, 2012].

In summary, the preliminary hourglass control study consisted of three identical models, all defined using the Winfrith material model, with the exception of a varying hourglass definition card. Specimen 1 was defined using *IHQ 1*, Specimen 2 was defined using *IHQ 3*, and Specimen 3 was defined using IHQ 5. Renderings taken from the final time step of each simulation are presented in Figure 4-15.

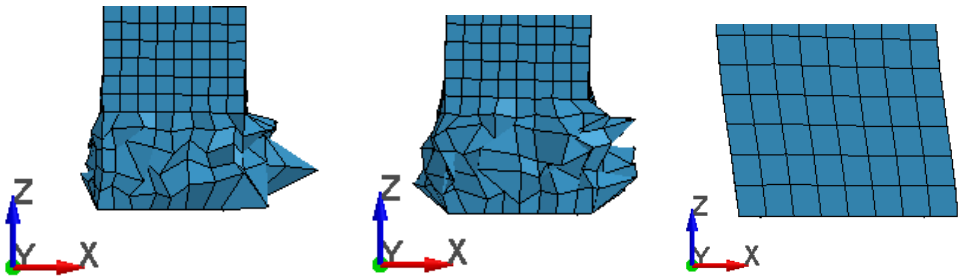

Specimen 1 – IHQ 1 Specimen 2 – *IHQ 3* Specimen 3 – *IHQ 5*

Figure 4-15: Hourglass Control Study Renderings -Enlarged Base

Upon visual inspection, it is evident that Specimen 3, corresponding to *IHQ 5* (the stiffness-based exact integration hourglass form), showed the least zero-energy deformation by a wide margin. Note that the results from Figure 4-15 are all plotted using an amplification factor of 1.0 for the deflected shape. Each of models defined using the viscous forms produced displaced shapes that deviated from reality by such a wide margin that their results should not be considered valid. Recall from Section 2.2 that the stiffness form is considered most effective in problems with low velocities, while the viscous form

is considered most effective in problems involving high velocities. The renderings presented in Figure 4-15 appear to align well with these expectations.

In addition to visual inspection, it is considered good modeling practice to identify the energy used by the specified hourglass control. Recall from Chapter 2 that hourglass control works by introducing an artificial force that resists the element's tendency to displace in a zero-energy deformation mode. Note that this artificial force does work on the element and therefore reduces the energy in the system. It is common practice to limit this artificially consumed hourglass energy to a maximum value 10% for most problems [Baeck et al.].

The hourglassing energy and total energy for the three simulations are presented in Figure 4-13. The hourglassing energy corresponding to both viscous forms slightly exceeds 10%, while the energy of the stiffness-based control does not exceed 1%. While both viscous forms imposed higher forces to attempt to control hourglassing, the results show their formulations were both ineffective and inefficient in terms of producing the correct solution. On the contrary, the stiffness form eliminated hourglassing in an efficient manner and demonstrated its suitability for the problem under consideration. These results have important implications for the RHT model, as this particular model has been shown in Chapter 3 to be ill-configured for use with stiffness-based hourglass control.

4.3.4 Results and Discussion

The results presented in this section aim to illustrate each material model's ability to accurately capture peak lateral resistance, lateral stiffness, cyclic loading, load reversal, and energy dissipation. Figure 4-16 through Figure 4-19 show renderings of each FE model at peak imposed displacement and at the termination time when the imposed displacement was specified to be zero.

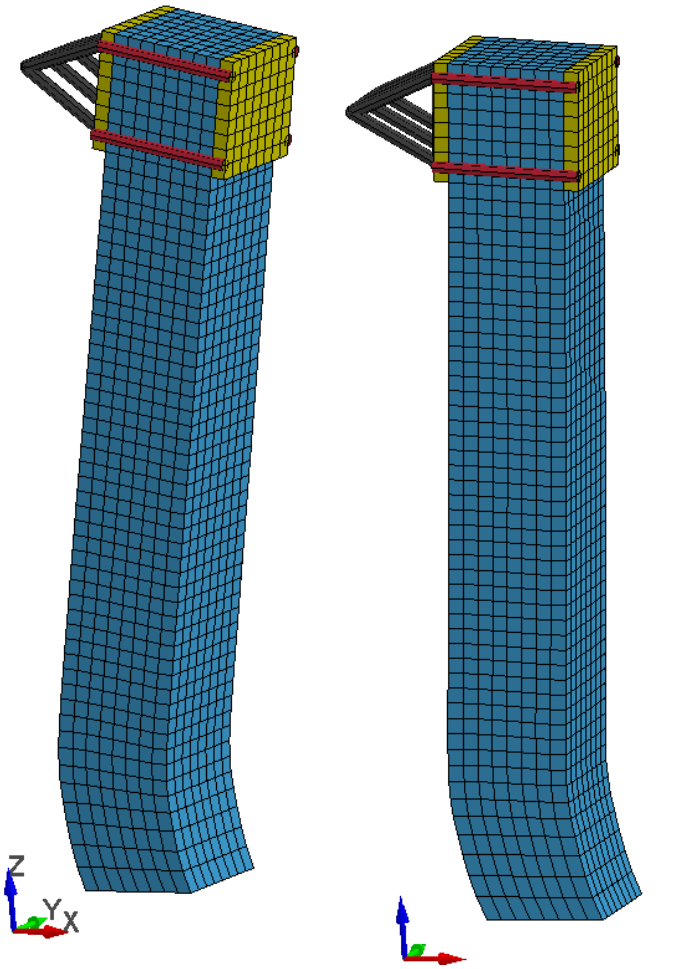

Peak Displacement Termination Time

Figure 4-16: KCC Beam Renderings

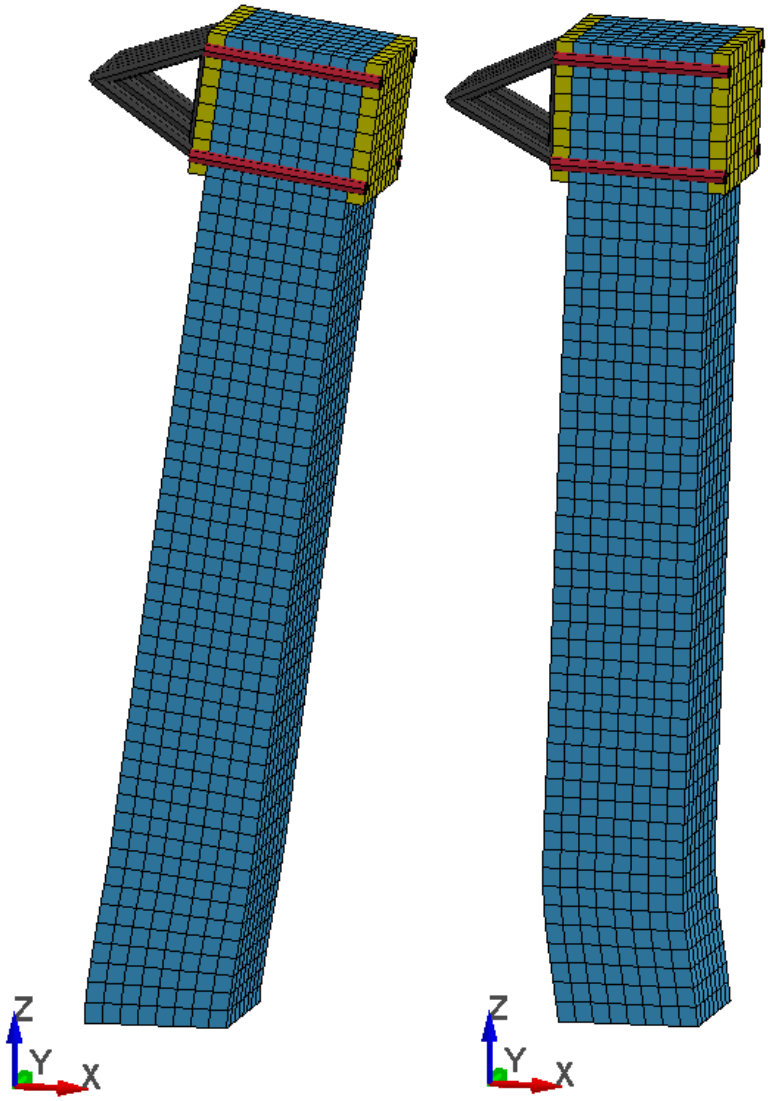

Peak Displacement Termination Time

Figure 4-17: Winfrith Beam Renderings

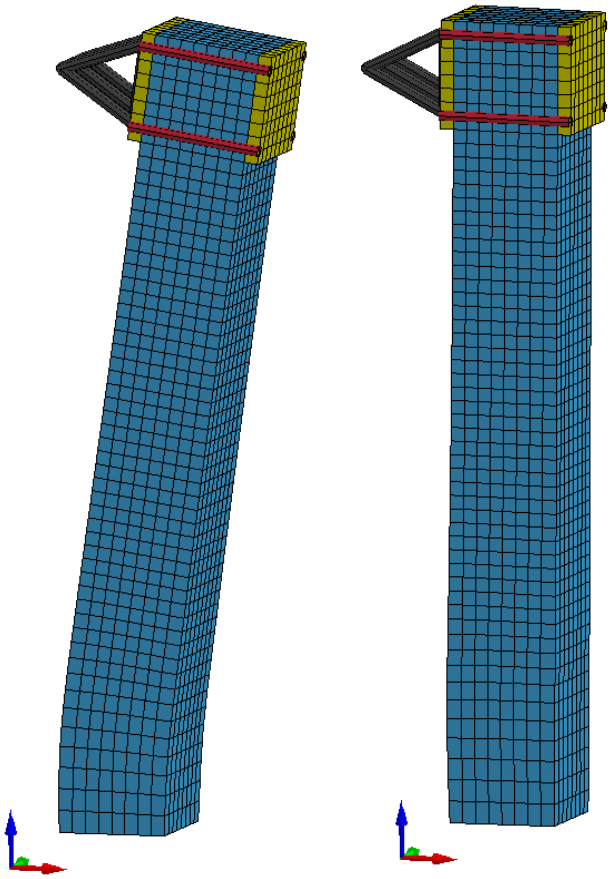

Peak Displacement Termination Time

Figure 4-18: SCS Beam Renderings

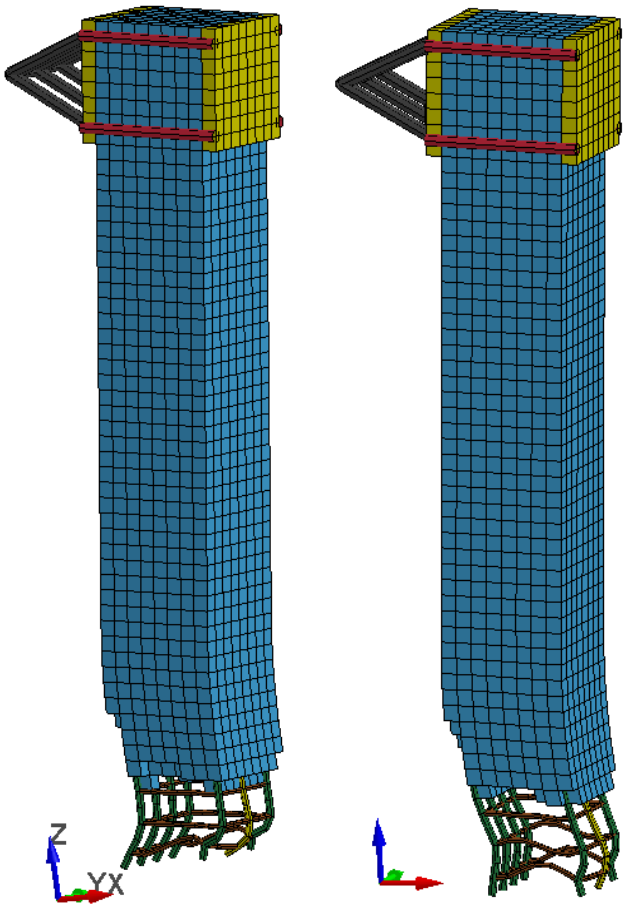

Peak Displacement Termination Time

Figure 4-19: RHT Beam Renderings

Base shear versus displacement results for the KCC cyclic beam bending test are presented in Figure 4-20. While the KCC model reasonably captured cyclic loading in the push direction, load reversal was completed missed. These results were expected and are consistent with conclusions drawn from Section 3.4.1 in which a single element was also unable to capture load reversal. Because the damage model within the formulation uses a coupled damage parameter to represent both tensile and compressive damage, once the concrete elements have cracked in tension, they can no longer carry compressive stress.

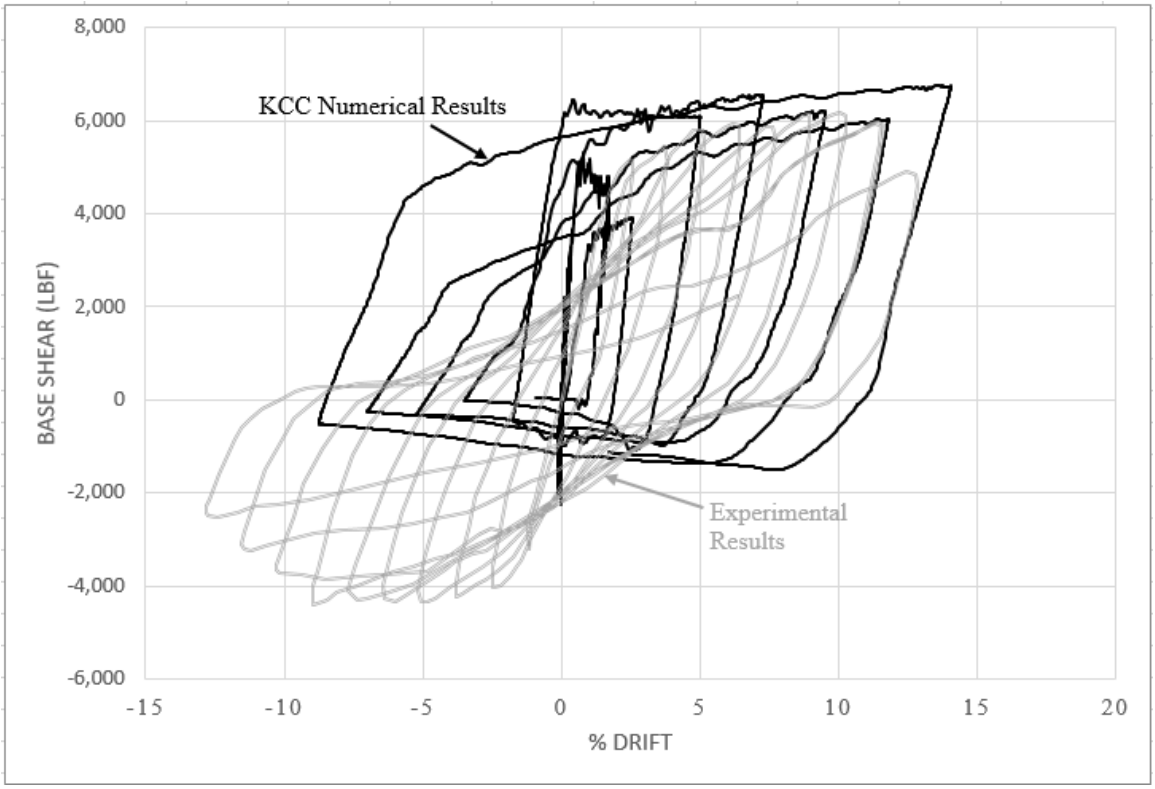

Figure 4-20: KCC Cyclic Beam Bending Results

Note that the final displaced shape of the KCC beam, as shown in Figure 4-16, includes considerable plastic deformation. This result is another by-product of the model's inability to handle load reversal. To better understand this behavior, consider a full push-pull cycle as depicted in Figure 4-21. As the beam is initially displaced in the push direction, Side A of the beam is loaded in tension and Side B is loaded in compression. Note that the neutral axis for this example has been shown at the center of the beam simply for the sake of illustration.

Initially, it can be expected that a large majority, if not all, of the tension force on Side A will be carried by the reinforcement because a majority of the concrete on Side A will crack and not contribute any significant resistance. On Side B, the concrete can be expected to contribute a majority of the resultant compression force. As the direction of

displacement is reversed, the roles of the concrete are also reversed; thus, the concrete on Side A will now be expected to contribute a majority of the compression force and the concrete on Side B will be expected to undergo tensile cracking. However, because the concrete on Side A has already cracked in tension and the KCC formulation incorporates a tension/compression coupled damage parameter, the concrete on Side A no longer has any compressive capacity. Consequently, the concrete on Side B will not undergo tensile cracking because there is no longer a significant force couple driving a large tensile force on Side B. Displacement will occur with relatively little lateral resistance as illustrated in Figure 4-20.

Finally, as the load is reversed yet again into a second push cycle, the concrete on Side B will be re-engaged in compression. Because this concrete did not undergo tensile cracking in the previous pull cycle, it can still reach full compressive capacity. This explains why Figure 4-20 shows reasonable agreement between the KCC model and experimental results for push cycles but inaccurately predicts the response on pull cycles. Note that the displaced shape following the initial pull cycle is “locked in” for the remainder of the simulation.

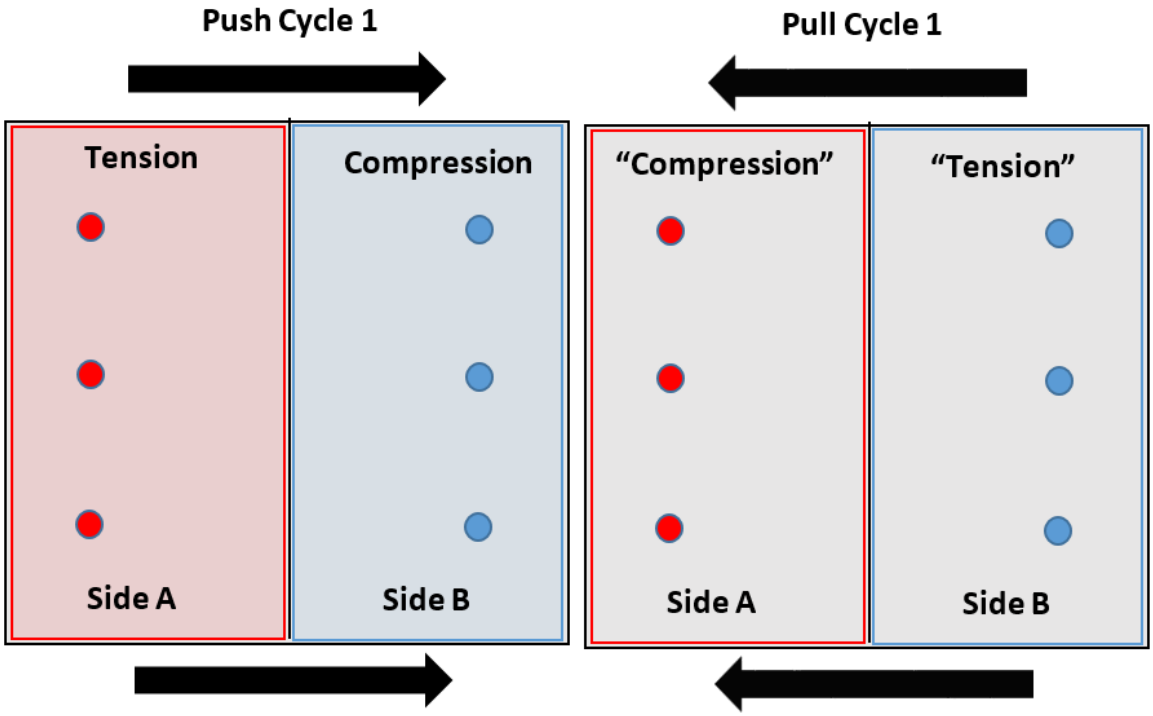

Figure 4-21: KCC Coupled Damage Illustration

Base shear versus drift results for the Winfrith cyclic beam bending model are presented in Figure 4-22. The Winfrith model captured peak lateral resistance in both the push and pull directions, demonstrating that it has the capability to handle both load reversal and cyclic loading. The accuracy of the peak lateral resistance is an important finding, especially for this particular material model, as one of the main concerns identified in Chapter 3 was the model's elastic-perfectly-plastic concrete behavior assumption. While it was hypothesized that this assumption was an over-simplification and would negatively affect the computed results for multi-element models, this does not appear to be the case. Lastly, while hysteresis loops generated by the Winfrith model are significantly more full than the experimental hysteresis (meaning the Winfrith model dissipates more energy than the test specimen), there does appear to some pinching occurring during the push cycles.

This observation is consistent with the conclusions drawn from the single-element analyses described in Section 3.4.1, where the model's ability to "close cracks" was demonstrated.

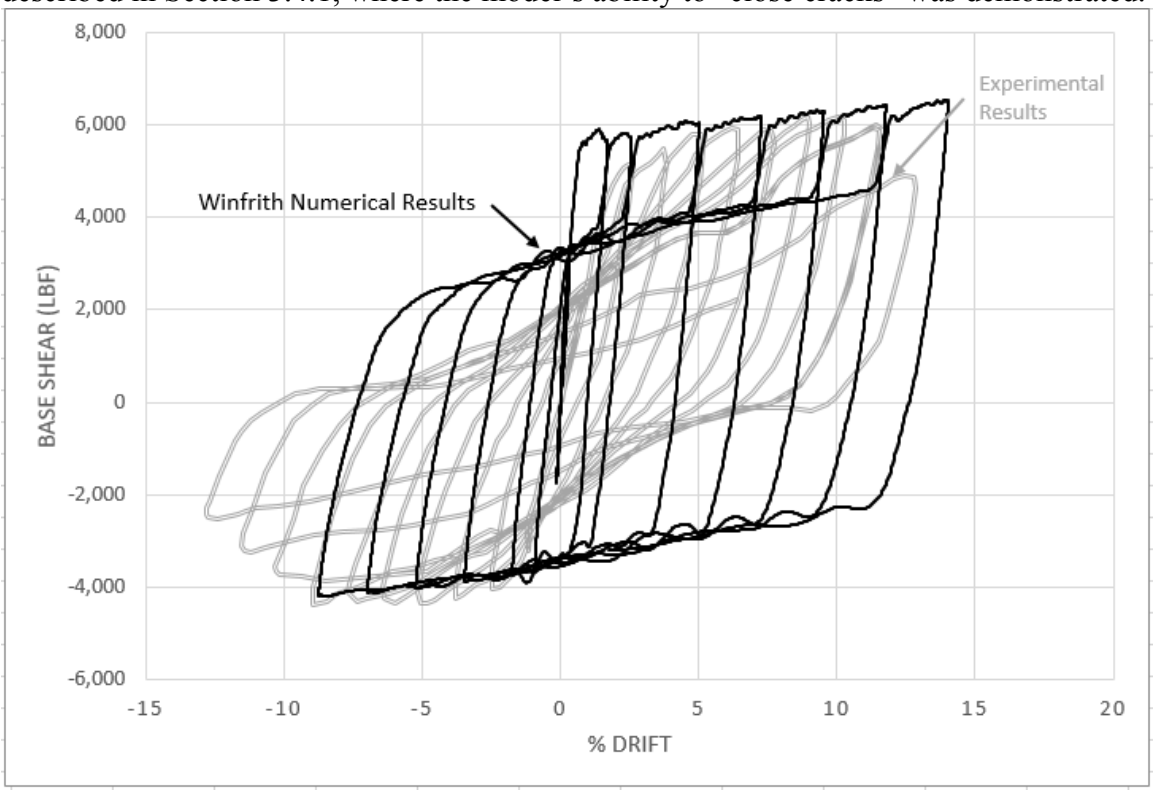

Figure 4-22: Winfrith Cyclic Beam Bending Results

Base shear versus drift results for the CSC cyclic beam bending model are presented in Figure 4-23. Like the Winfrith model, the results indicate the CSC material model can handle both load reversal and cyclic loading on a multi-element level. However, unlike the Winfrith model, the CSC model struggled to accurately predict peak lateral capacities.

It is hypothesized that the poor agreement with the experimental results arose from an issue demonstrated in Section 3.4.1; namely, that the CSC material model cannot capture the physical crack width that is opened during tensile loading. Further description of this phenomenon is provided in Section 3.4.1, but the key repercussion here is that as load reversal occurs, the beam is shown to immediately resist movement in the opposite

direction. Thus, the cracks on the tensile side of the beam immediately close at the onset of load reversal and begin to engage in compression, thereby resisting the movement of the beam as it returns to the neutral position. This means that peak lateral resistance is achieved far before the beam has reached the neutral position. Additionally, because peak lateral resistance is achieved prior to the neutral position, compression softening begins to play a role in reducing the peak lateral resistance of the beam when it finally reaches its maximum drift. Furthermore, this response creates full hysteresis loops that differ from the relatively pinched hysteresis loops seen in the experimental results. This mismatch in hysteresis shape has implications for energy dissipation as well.

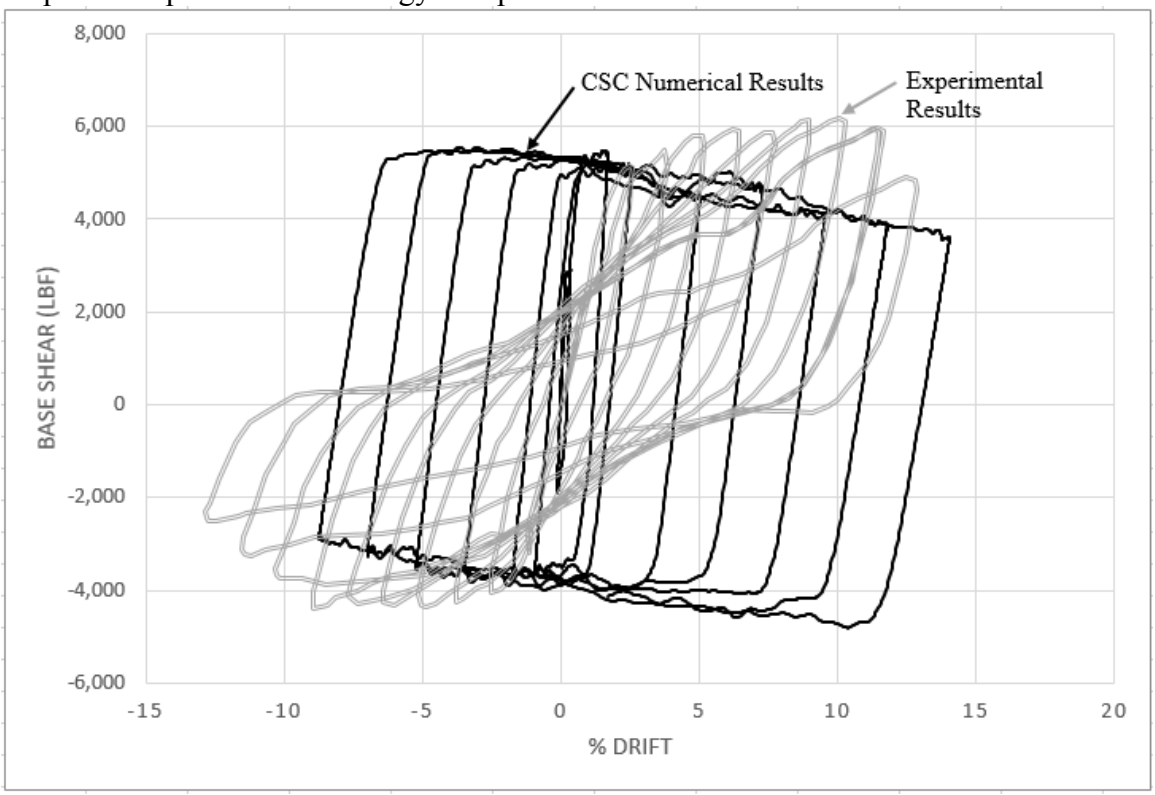

Figure 4-23: CSC Cyclic Beam Bending Results

The results for the RHT cyclic beam bending simulation are presented in Figure 4-24. As predicted in Section 4.3.3, the restriction placed on prescribed hourglass control for

the RHT concrete model significantly impacted the results of the beam bending problem. While the KCC, Winfrith, and CSC models were all defined using a stiffness-based form of hourglass control that, as shown in Section 4.3.3, effectively eliminated zero-energy deformation modes from forming, the RHT model required a viscous form of hourglass control and was therefore subject to significant zero-energy deformations.

Figure 4-19 shows a rendering of the RHT cyclic beam bending model at the final time step of the simulation. Note the missing elements at the base of the column. The reason for these missing elements is a combination of poor hourglass control and built-in erosion within the RHT concrete model formulation. Erosion, or an elimination of specific elements within the model based on the exceedance of a specified maximum displacement, is a tool often included in FE models to avoid erroneous results due to contributions from highly deformed elements. Thus, if an element exceeds a specified displacement, that specific element is removed from the simulation and can no longer influence the results of the model. Recall from Figure 4-14 the large deformations in the concrete elements at the bottom of the column due to poor hourglass control. Again, because the RHT model includes a built-in erosion function, these large zero-energy deformations likely caused the elements at the bottom of the column to exceed their maximum allowed displacement and were therefore removed from the model. This explanation is also supported by the timing of the dramatic reduction in lateral resistance illustrated in Figure 4-24. The hourglass study showed significant increase in zero-energy deformation between cycle four and five of the simulation. Not surprisingly, erosion and loss of lateral capacity occurred between cycles four and five in the RHT simulation as well.

Note that the results taken from the model shown in Figure 4-14 and the results reported here in Figure 4-24 are both incorrect. The key conclusion to be drawn here is not

that erosion is bad, but rather that the viscous hourglass control restriction severely limits the RHT model's ability to be applied to low-velocity seismic problems.

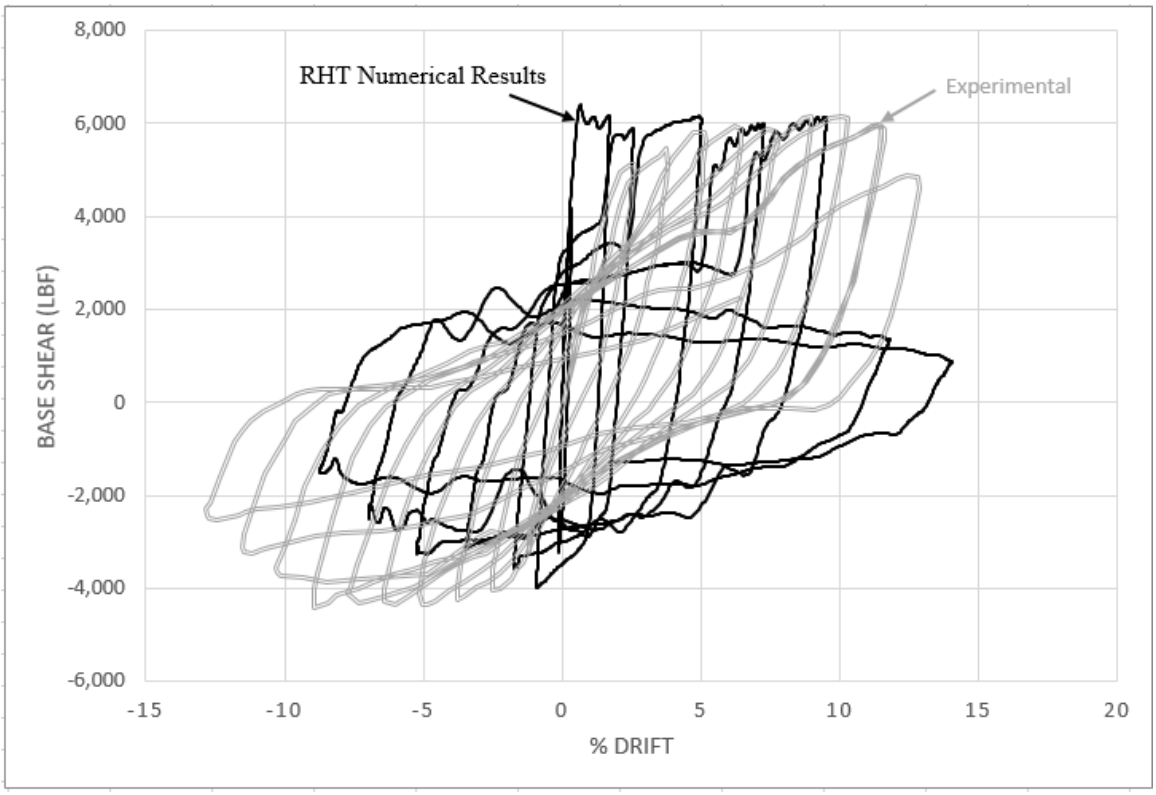

Figure 4-24: RHT Cyclic Beam Bending Results

4.4 Multi-Element Validation Closing Remarks

Recall that the objective of the multi-element validation study was to demonstrate the ramifications of each material model's limitations. This objective was met through a detailed parametric study in which LS-DYNA predictions were compared against experimental data for a cyclically loaded beam. Several hypotheses drawn from Chapter 3 were verified, and others were discredited.

As anticipated, the KCC model's coupled damage formulation prevented the model from capturing realistic results. In simple terms, the test presented in Section 4.3 has shown

that the KCC model is not well suited for analyzing structures subjected to seismic loads. The Winfrith model was shown in Chapter 3 to represent concrete as elastic-perfectly-plastic, and the expectation moving into Chapter 4 was that this simplification of behavior would adversely affect the performance when using this model for realistic problems. As demonstrated in Section 4.3, however, this was not the case. The Winfrith model performed better than the other three more sophisticated models. The CSC model showed relatively good performance, especially when compared to the KCC and RHT models, though the manner in which cracked concrete is treated by this model did introduce erroneous results. As expected, this simplification resulted in full hysteresis loops that poorly matched experimental results. The implications of this behavior are addressed in Chapter 5. Finally, the RHT model's inflexibility with regard to hourglass control was shown to have adverse effects on modeling full-scale seismic problems.

Chapters 3 and 4 presented results from eight different studies conducted with the KCC, Winfrith, CSC, and RHT concrete models. These studies evaluated each model's capabilities to capture simple compression, shear, cyclic loading, and load reversal, among other things. This broad scope of analysis is necessary for validating the performance of each model; however, considering such a broad scope of analysis makes it all the more necessary to compile the results and derive useful and applicable conclusions. Chapter 5 aims to accomplish this final task.

Chapter 5: Conclusions

5.1 General Remarks

Prior to presenting conclusions that can be drawn from the work presented in this thesis, it is beneficial to revisit the primary goal and motivation of this effort. Chapter 1 demonstrated how FE modeling of seismic performance could be useful in closing a current knowledge gap in seismic design. For FE modeling to beneficial, however, the validity of the simulations must be established. To date, limited validation work has been performed using the LS-DYNA platform. Therefore, this thesis has aimed to contribute to the validation effort by providing an overview of the seismic performance of various LS-DYNA concrete constitutive models as well as present a list of recommendations and limitations associated with each material model's capabilities. Chapters 3 and 4 presented an overview of the performance of four particular LS-DYNA concrete models as compared to experimental data, Section 5.2 presents a list of limitations and recommendations associated with each model, and Section 5.3 presents a final collection of recommendations regarding general modeling of seismically loaded systems using LS-DYNA concrete models.

Note that it's important to consider the following conclusions in context. The models considered in this thesis were not designed specifically for seismic performance. While each of the models were developed by leading experts in the blast and impact fields and have been thoroughly validated in this context, they do not necessarily have the capabilities required to handle seismic response. With this in mind, this thesis does not aim to discredit any particular concrete model. Rather, it aims to demonstrate the strengths and limitations of the models as applied to analysis of structures under seismic loads.

5.2 Performance Overview and Recommendations

This section summarizes the conclusions drawn from the single-element and multiple-element investigations, presented in Chapters 3 and 4, respectively, and presents a series of limitations and recommendations specific to each material model. Additional details can be found in the appropriate sections of Chapters 3 and 4. Final recommendations for seismic modeling of structural systems are presented in Section 5.3.

5.2.1 KCC

5.2.1.1 Performance Overview and Limitations

Monotonic compression results for the KCC formulation showed that the model's post-peak behavior is sensitive to element size. As element size decreased, the element maintained capacity for large strains that exceed what is expected. While the formulation does have an option to manually adjust post-peak scaling based on element size and the use of this feature does improve consistency of the behavior predicted by the element, the accuracy, with respect to the Thorenfeldt model, is not improved. Additionally, users should be cautious of using element sizes smaller than three times the defined size of the aggregate, as this was shown to cause erroneous results.

Strain-rate effects are included in the KCC model by incorporating a DIF curve in the material's definition. Although this process is straightforward, users should note a couple inconsistencies in the results. First, results from the strain rate investigation showed that the KCC model exceeded the manually specified DIF at high strain rates. Second, analyses showed instability in the results for low strain rates when a DIF curve was not specified.

The indirect shear investigation demonstrated the model's capability to accurately capture both uniaxial tension and compression softening. As discussed in Section 3.3,

accurate representation of these two behaviors indicates a model that is adequately configured to handle shear.

Cyclic compression tests, conducted both with single-and multiple-element models, showed that the KCC material model could capture load cycles relatively accurately. Although the model did not capture stiffness degradation, both the capacity and the backbone post-peak behavior curve showed reasonable agreement with experimentally collected results.

The model's inability to capture load reversal was identified in Section 3.4, and the repercussions of this limitation were demonstrated in Section 4.3. In short, the model's inability to capture load reversal significantly impacted the results for seismic loading to a point where they were no longer reflective of the physical system.

5.2.1.2 Recommendations

To address inconsistencies in post-peak behavior, it is recommended that analysts use the B1 scaling factor when possible. When element size varies over the domain of a model, post-peak behavior should be carefully monitored. Additionally, users should be wary of specifying the KCC formulation for elements smaller than three times the defined aggregate size. While it's possible that smaller meshes may be used, these results should be carefully evaluated.

To address the apparent instability detected when structures respond with low strain rates, it's recommended that users carefully monitor peak compressive capacities and always included A DIF curve as part of the material definition (even if this curve simply specifies a DIF of 1.0 for all strain rates).

Because the load reversal limitation stems from a coupling of tensile and compressive damage, there is no recommendation that can be made to address this issue.

Fundamentally, the KCC model is ill-configured for use with seismic problems where any tensile strains are expected.

5.2.2 WINFRITH

5.2.2.1 Performance Overview and Limitations

The Winfrith monotonic compression results showed that this model approximates concrete behavior as elastic-perfectly-plastic. While perhaps an oversimplification (at least at the single-element level), the behavior was shown to be consistent over all tested strain rates, hourglass formulations, element formulations, and element sizes, establishing it as the most consistent model considered in the study.

Similarly, to the KCC formulation, the indirect shear investigation demonstrated the model's capability to accurately capture both uniaxial tension and compression softening. As discussed in Section 3.3, accurate representation of these two behaviors indicates a model that is adequately configured to handle shear.

The single-element cyclic compression tests showed that the Winfrith model captures load cycles relatively accurately. While the elastic-plastic backbone of the model has limited agreement with experimental results, the cyclic nature of loading was captured consistently (although again, stiffness degradation was not considered). The multiple-element cyclic compression test, however, yielded results that seemed to contradict the single-element test results. The cause of this discrepancy is unclear.

Unlike the KCC model, the Winfrith model was able to accurately capture load reversal. This capability was demonstrated both in the single-element study presented in Section 3.4.1 and the beam bending problem presented in Section 4.3. Note that for this particular problem, the Winfrith model dissipated roughly 200% of the energy dissipated in the experimental test. Repercussions of this inconsistency are discussed in Section 5.3.

5.2.1.2 Recommendations

Few recommendations are required for this model as it performed consistently over a broad spectrum of tests. The exception to this consistency was observed in the multiple-element cyclic compression test. Because it is not clear what caused the unique loops seen in the results, it is difficult to provide specific recommendations to address this concern. Users are encouraged to spot check the behavior of elements defined with the Winfrith model.

5.2.3 CSC

5.2.3.1 Performance Overview and Limitations

The CSC monotonic compression results were nearly identical to the Thorenfeldt theoretical model. Nonetheless, as with the KCC model, the results were sensitive to hourglass formulation, element formulation, and element size. Post-peak scaling was especially sensitive to element size. As shown in Section 3.2.2, strength degradation was almost negligible for an element size of one inch. Additionally, the strain-rate study appeared to show that as strain rate increased to 1 sec^{-1}, the capacity of the concrete became smaller as compared to concrete loaded at a slower strain rate. This reduction in capacity is inconsistent with expectations drawn from experimental data.

Once again, the indirect shear investigation demonstrated the model's capability to accurately capture both uniaxial tension and compression softening. As discussed in Section 3.3, accurate representation of these two behaviors indicates a model that is adequately configured to handle shear.

Both the single-element and multiple-element cyclic compression tests showed that the CSC model was effective at capturing load cycles. Not only did the model capture the

capacity and backbone of the experimental data, but it also captured stiffness degradation, which is something the KCC, Winfrith, and RHT models failed to do.

Results from the compression-tension single-element tests and beam bending tests showed that while the CSC model was able to consider load reversal, the model fails to consider realistic crack behavior. As demonstrated in the beam bending problem, this particular simplification leads to full hysteresis loops that do not pass through the origin, which poorly aligns with experimental data. This aspect of response is important when considering the energy dissipated by the system. The CSC model in Section 4.3 dissipated roughly 300% of the energy dissipated in the experimental test. Repercussions of this inconsistency are discussed in Section 5.3.

5.2.3.2 Recommendations

Users should understand the implications of changing the element size in models that incorporate the CSC material model. While 4-inch elements reproduce experimental/theoretical results exceptionally well, 1-inch elements produce nearly elastic-perfectly-plastic behavior. As noted for the Winfrith model, elastic-plastic response of a single element does not necessarily adversely affect multiple-element performance, but the inherent assumption should still be understood.

The most significant limitation identified for the CSC model was again the simplification of crack behavior. As with the KCC model's damage limitation, this crack limitation is inherent to the model; therefore, no recommendation can be made to correct it.

5.2.4 RHT

5.2.4.1 Performance Overview and Limitations

The RHT monotonic compression results produced several important conclusions: (1). the model over-predicts concrete strength, (2). the model over-predicts yield strain, (3). post-peak response is nearly elastic-perfectly-plastic, and (4). the model is ill-configured for use with stiffness hourglass formulations. All four of these points represent fairly important limitations of the model that were later shown in Section 4.3 to adversely affect multiple-element response.

As before, the indirect shear investigation demonstrated the model's capability to accurately capture both uniaxial tension and compression softening. As discussed in Section 3.3, accurate representation of these two behaviors indicates a model that is adequately configured to handle shear.

Both the single-element and multi-element cyclic compression tests showed that the even though the RHT model could capture compression load cycles, the backbone response of the formulation limits agreement with experimental results. Lastly, results from the beam bending problem demonstrated perhaps the most significant limitation associated with the RHT model—it's inability to be used in conjunction with a stiffness-based hourglass formulation. This is a major limitation for structures under seismic loads because these specific types of problems contain relatively low velocities, as compared with blast or impact problems. Accordingly, rigid-body modes, such as the one demonstrated in Section 4.3, are most effectively corrected with stiffness-based hourglass formulations. Because the RHT model is forced to use a less efficient hourglass formulation, the model is likely to be adversely affected by rigid-body displacements. Again, as demonstrated in Section 4.3, this can lead to results that significantly deviate from the physical problem.

5.2.4.2 Recommendations

The numerous limitations associated with the RHT model are largely all problems inherent to the formulation itself and therefore cannot be easily addressed by the user. For example, the model's over-prediction of specified strength, yield strain, and under - prediction of realistic post-peak softening are all products of the RHT's automatic parameter generation tool. Users that do choose to use the RHT material model should consider manual specification of parameters rather than reliance on the automatic generation tool. A simpler recommendation may be to avoid the model in favor of the Winfrith or CSC models.

5.3 CLOSING RECOMMENDATIONS AND REMARKS

Fundamentally, the KCC model is ill-configured for use with seismic problems where any tensile strains are expected. Therefore, the KCC model is not recommended for analyzing structures subjected to seismic loads.

While the Winfrith model utilizes the simplest representation of concrete behavior, (elastic--perfectly-plastic), it consistently captures this behavior regardless of varying element sizes, element formulations, and other parameters. This consistency should not be overlooked, especially when considering the formulation for use in sophisticated problems where it may be necessary to perform mesh refinement or hourglass control studies. Additionally, the beam bending problem demonstrated that the model's simplification of concrete behavior may not adversely affect the results of a multiple-element model. Both the capacity and stiffness of the beam bending problem were accurately captured. Therefore, the Winfirth model appears to be adequately configured for use with seismic problems.

As with the Winfrith model, the CSC model demonstrated that it includes all the necessary capabilities for use with seismic problems. Nonetheless, users should understand

the inherent cracking simplification and its impact on hysteresis shape and energy dissipation. Overall, the CSC model appears to be adequately configured for use with seismic problems.

Due to the over-prediction of manually specified strength, poor representation of yield strains and softening rates, and the model's inability to be used in conjunction with stiffness-based hourglass formulations, the RHT model is not recommended for analyzing seismically loaded structures. The other models considered in this study showed better behavior when compared to experimentally measured values.

This thesis recommends the use of either the Winfrith or CSC model for use with seismic applications. Additionally, based on the results presented in Section 4.3, readers can conclude that the Winfrith model provides the best capabilities for capturing accurate seismic performance. However, note that even the Winfrith model over-predicted energy dissipation relative to the experimental test by over 200%. This error was not particularly important for the beam bending problem presented in Section 4.3 because this problem was displacement-controlled. If LS-DYNA concrete models are to be used for more realistic seismic problems that introduce acceleration histories, however, accurately capturing peak displacement depends strongly on proper calculation of energy dissipation. As a result, this thesis does not recommend LS-DYNA to be used to simulate problems that included acceleration histories. Instead, another FE platform is recommended.

5.4 FUTURE WORK

The work included in this thesis presents a strong foundation for seismic validation of the KCC, Winfirth, CSC, and RHT concrete models. As is the case with any research, however, the scope of the effort is limited. Because a large effort was spent understanding the fundamental behavior of the material models on a single-element level, this thesis only

included one realistic seismic analysis problem. Therefore, future effort made on this topic should aim to expand the validation effort to additional full-scale problems of seismically loaded structures. One suggestion is to study a concrete moment frame subjected to an acceleration history to verify the hypothesis made at the end of Section 5.3.

Although the Winfrith and CSC models were able to accurately capture many aspects unique to seismic loading, the material models still neglected strength degradation due to cyclic loading and generated full hystereses that differ from the pinched hystereses observed in the experimental data. Again, this indicates poor representation of energy dissipation. Therefore, if LS-DYNA is to be used for future seismic research, particularly research that utilizes imposed acceleration histories, it may be beneficial to develop an additional material model that can more accurately capture strength degradation and energy dissipation. As it currently stands, numerical results of concrete structures subjected to acceleration histories can be expected to significantly underestimate peak displacements.

Appendix A – LS-DYNA Keycards

This appendix provides the keycards used for the beam bending problem presented in Section 4.3. The keycards used to define geometry (i.e. nodes, beams, solids etc.) have been excluded for the sake of brevity. LS PrePost® V4.3 was used to generated the keyword file.

A1 – Material Definitions

```
*MAT_CONCRETE_DAMAGE_REL3_TITLE
Mat 072 - KCC
$#     mid        ro        pr
         1  12.24900E-4      0.15
$#      ft        a0        a1        a2        b1     omega       a1f
       0.0   -3340.0       0.0       0.0       0.0       0.0       0.0
$# slambda      nout     edrop     rsize       ucf    lcrate  locwidth      npts
       0.0       0.0       0.0       1.0       1.0         0     0.125       0.0
$# lambda1   lambda2   lambda3   lambda4   lambda5   lambda6   lambda7   lambda8
       0.0       0.0       0.0       0.0       0.0       0.0       0.0       0.0
$#lambda09  lambda10  lambda11  lambda12  lambda13        b3       a0y       a1y
       0.0       0.0       0.0       0.0       0.0       0.0       0.0       0.0
$#     eta1      eta2      eta3      eta4      eta5      eta6      eta7      eta8
       0.0       0.0       0.0       0.0       0.0       0.0       0.0       0.0
$#    eta09     eta10     eta11     eta12     eta13        b2       a2f       a2y
       0.0       0.0       0.0       0.0       0.0       0.0       0.0       0.0
*MAT_WINFRITH_CONCRETE_TITLE
Mat 084 - Winfrith
$#     mid        ro        tm        pr       ucs       uts        fe     asize
         2  22.24900E-4   3249000      0.15    3340.0     333.4     0.005     0.125
$#       e        ys        eh    uelong      rate      conm      conl      cont
       0.0       0.0       0.0       0.0       2.0       0.0       0.0       0.0
$#    eps1      eps2      eps3      eps4      eps5      eps6      eps7      eps8
       0.0       0.0       0.0       0.0       0.0       0.0       0.0       0.0
$#      p1        p2        p3        p4        p5        p6        p7        p8
       0.0       0.0       0.0       0.0       0.0       0.0       0.0       0.0
*MAT_CSCM_CONCRETE_TITLE
Mat 159 - CSC
$#     mid        ro     nplot     incre     irate     erode     recov   itretrc
         3  32.24900E-4         1       0.0         0       0.0       0.0         0
$#    pred
       0.0
$#     fpc      dagg     units
    3340.0     0.125         3
```

```
*MAT_RHT_TITLE
Mat 272 - RHT
$#     mid        ro     shear    onempa      epsf        b0        b1        t1
         42.24900E-4       0.0     -4.0       2.0       0.0       0.0       0.0
$#       a         n        fc       fs*       ft*       q0         b        t2
       0.0       0.0    3340.0       0.0       0.0       0.0       0.0       0.0
$#     e0c       e0t        ec        et     betac     betat       ptf
       0.0       0.0       0.0       0.0       0.0       0.0     0.001
$#     gc*       gt*        xi        d1        d2       epm        af        nf
       0.0       0.0       0.0       0.0       0.0       0.0       0.0       0.0
$#   gamma        a1        a2        a3       pel       pco        np     alpha
       0.0       0.0       0.0       0.0       0.0       0.0       0.0       0.0
*MAT_PLASTIC_KINEMATIC_TITLE
Mat 03 - Elastic Plastic
$#     mid        ro         e        pr      sigy      etan      beta
         5  0.0036652.900000E7       0.3   59800.0       0.0       0.0
$#     src       srp        fs        vp
       0.0       0.0       0.0       0.0
*MAT_ELASTIC
$#     mid        ro         e        pr        da        db  not used
         68.06000E-43.000000E8       0.3       0.0       0.0         0
*MAT_RIGID_TITLE
Rigid
$#     mid        ro         e        pr         n    couple         m     alias
         87.33000E-42.900000E7       0.3       0.0       0.0       0.0
$#     cmo      con1      con2
       0.0         0         0
$#lco or a1        a2        a3        v1        v2        v3
       0.0       0.0       0.0       0.0       0.0       0.0
```

A2 – ELEMENT FORMULATIONS AND HOURGLASS CONTROL

```
*SECTION_SOLID_TITLE
ELF1 - Solid
$#   secid    elform       aet
         1         1         0
*SECTION_BEAM_TITLE
Number 8 Bar
$#   secid    elform      shrf   qr/irid       cst     scoor       nsm
         5         1       1.0         2         1       0.0       0.0
$#     ts1       ts2       tt1       tt2     nsloc     ntloc
     0.315     0.315       0.0       0.0       0.0       0.0
*SECTION_BEAM_TITLE
Number 12 Bar
$#   secid    elform      shrf   qr/irid       cst     scoor       nsm
         3         1       1.0         2         1       0.0       0.0
$#     ts1       ts2       tt1       tt2     nsloc     ntloc
     0.472     0.472       0.0       0.0       0.0       0.0
```

```
*SECTION_BEAM_TITLE
Number 16 Bar
$#    secid     elform      shrf    qr/irid       cst     scoor       nsm
         6          1       1.0          2         1       0.0       0.0
$#      ts1        ts2        tt1        tt2     nsloc     ntloc
     0.623      0.623        0.0        0.0       0.0       0.0
*SECTION_BEAM_TITLE
Truss
$#    secid     elform      shrf    qr/irid       cst     scoor       nsm
         7          3       1.0          2         1       0.0       0.0
$#        a      rampt     stress
      0.75        0.0        0.0
*HOURGLASS_TITLE
IHQ0 Default
$#     hgid       ihq        qm       ibq        q1        q2     qb/vdc        qw
         3         1       0.1         0       1.5      0.06       0.1       0.1
*HOURGLASS_TITLE
IHQ3 Default
$#     hgid       ihq        qm       ibq        q1        q2     qb/vdc        qw
         4         3       0.1         0       1.5      0.06       0.1       0.1
*HOURGLASS_TITLE
IHQ5 Default
$#     hgid       ihq        qm       ibq        q1        q2     qb/vdc        qw
         5         5       0.1         0       1.5      0.06       0.1       0.1
```

A3 – CONTROL AND LOAD APPLICATION CARDS

```
*CONTROL_ENERGY
$#     hgen      rwen    slnten     rylen
         2         2         1         2
*CONTROL_TERMINATION
$#  endtim    endcyc     dtmin    endeng    endmas
  4.464214         0       0.0       0.01.000000E8
*CONTROL_TIMESTEP
$#  dtinit    tssfac      isdo    tslimt     dt2ms      lctm     erode     ms1st
       0.0       0.9         0       0.0       0.0         0         0         0
$#  dt2msf   dt2mslc     imscl    unused    unused     rmscl
       0.0         0         0                         0.0
*BOUNDARY_PRESCRIBED_MOTION_RIGID
$#     pid       dof       vad      lcid        sf       vid     death     birth
        12         1         0         2       1.0         01.00000E28       0.0
```

```
*DEFINE_CURVE_TITLE
Impulse Method (Definied Velocity)
$#     lcid      sidr       sfa       sfo      offa      offo    dattyp     lcint
         2         0       1.0       1.0       0.0       0.0         0         0
$#               a1                  o1
                 0.0                 0.0
            0.045943            5.321497
            0.107583            -7.13954
            0.227389            13.87677
            0.378375            -17.4882
            0.555123            20.47221
            0.750045            -22.5772
            0.993155            28.15872
            1.268816             -31.929
             1.58042            36.09215
            1.918034            -39.1049
            2.285582            42.57198
            2.675426            -45.1544
            3.091462            48.18821
             3.52732            -50.4842
            3.986755            53.21497
            4.464214            -55.3026
```

A4 – DATABASE CARDS

```
*DATABASE_GLSTAT
$#      dt    binary      lcur     ioopt
     0.001         1         0         1
*DATABASE_SECFORC
$#      dt    binary      lcur     ioopt
     0.001         1         0         1
*DATABASE_BINARY_D3PLOT
$#      dt      lcdt      beam     npltc    psetid
     0.001         0         0         0         0
$#   ioopt
         0
*DATABASE_CROSS_SECTION_PLANE_ID
$#     csid                                                         title
         1Column - Base Block Interface
$#     psid       xct       yct       zct       xch       ych       zch    radius
         0       0.0       0.0      17.0       0.0       0.0      18.0      50.0
$#     xhev      yhev      zhev      lenl      lenm        id     itype
       0.0       0.0       0.0       0.0       0.0         0         0
```

References

Abbas AA, Pullen AD and Cotsovos DM (2010) Structural response of RC wide beams under low-rate and impact loading. Magazine of Concrete Research 62(10): 723–740.

Adhikary SD, Li B and Fujikake K (2012) Dynamic behavior of reinforced concrete beams under varying rates of concentrated loading. International Journal of Impact Engineering 47: 24–38.

Alves, S W, and C R Nobel. Experimental Validations of LLNL Finite Element Codes for Nonlinear Seismic Simulation (Progress, Year 1 of 2) . 2006, pp. 1–30.

Alves, S W, and C R Nobel. Validation of Reinforced Concrete Modeling Capabilities for Seismic Response. 2007, pp. 1–43.

Baeck, K., J. Goffin, and J. Vander Sloten. "The Effects of Different Brain Material Properties, FE Mesh Size and Hourglass Modes on the Results of FE Head Impact Analyses." IFMBE Proceedings World Congress on Medical Physics and Biomedical Engineering, September 7 -12, 2009, Munich, Germany (2009): 902-05. Web.

Bahn, Byong Youl, and Cheng-Tzu Thomas Hsu. “Stress-Strain Behavior of Concrete

under Cyclic Loading." ACI Materials Journal, vol. 95, no. 2, 1998, doi:10.14359/363.

Behfarnia, K. "The Effect of Tension Stiffening on the Behavior of R/C Beams." Asian Journal of Civil Engineering (Building and Housing), vol. 10, no. No. 3, 2009, pp. 243–255.

Bischoff, P H, and S H Perry. "Compressive Behavior of Concrete at High Strain Rates." Materials and Structures Materiaux Et Concstructions, vol. 1991, 1991, pp. 425–450.

Borrvall, Thomas and Riedel Werner, "The RHT Concrete Model in LS-DYNA," for 8th European LS-DYNA Users Conference, Strasbourg, May, 2011.

Chen Y and May IM (2009) Reinforced concrete members under drop-weight impacts. Proceedings of the Institution of Civil Engineers – Structures and Buildings 162(1): 45–56.

Chen, W. F., and A. F. Saleeb (1981): "Constitutive Equations for Engineering Materials," vol. 1, "Elasticity and Modeling," Wiley, New York.

Crawford, J. E., Wu, J., Choi, H. J., Magallanes, J. M., and Lan, S. "Use and Validation of the Release III K&C Concrete Model in LS-DYNA." Karagozian & Case TR-11-36.5, 2012.

LS-DYNA Keyword User's Manual, Version 971, Volume I-III, Livermore Technology Software Corporation (LSTC), May 2012.

LS-DYNA Theory Manual, Livemore Technology Software Corporation (LSTC), March, 2006.

Magallanes, J. M., Wu, Y., Malvar, L. J., and Crawford, J. E., "Recent Improvements to Release III of the K&C Concrete Model," for 11th International LS-DYNA Users Conference, Dearborn, MI, June 6-8, 2010.

Marefat, Mohammad S. et al. "Cyclic Response of Concrete Beams Reinforced by Plain ' Bars." Journal of Earthquake Engineering, vol. 13, no. 4, Apr. 2009, pp. 463–481. doi:10.1080/13632460902837769.

Murray, Y., D., "Theory and Evaluation of Concrete Material Model 159," for the 8th international LD-DYNA Users Conference, Dearborn, MI, May 2-4, 2004.

Murray, Y.D., "Users manual for LS-DYNA concrete material model 159," Report No. FHWA-HRT-05-062, Federal Highway Administration, 2007

Pajak, Malgorzata. "The Influence of the Strain Rate of the Strength of Concrete Taking Into Account the Experiential Techniques." Architecture Civil Engineering Environment, 20 Sept. 2011, pp. 77–87.

Saenz, L. P. (1964): Discussion of "Equation for the Stress-Strain Curve of Concrete," by

Dessayi and Krishnan, Proc. Am. Concr. Inst., vol. 61, no. 9, September, pp. 1229-1235.

Schwer, L. E., Key, S., W., Pucik, T. A., and Binderman. L. P., "An Assesment of the LS-DYNA Hourglass Formulations via the 3D Patch Test," for the 5th European LS-DYNA Users Conference, Birmingham, UK, May 25-26, 2005.

Shetye, Gujan Ashock. "Finite Element Analysis and Experimental Validation of Reinforced Concrete Single-Mat Slabs Subjected to Blast Load." University of Missouri-Kansas City, 2012, pp. 1–172.

Unified Facilities Criteria (UFC) 3-340-02, "Structures to Resist the Effects of Accidental Explosions." December, 2008.

Vecchio, F. J., and Collins, M. P., "Response of Reinforced Concrete to In-Plane Shear and Normal Stress," Publication No. 82-03, Department of Civil Engineering, University of Toronto, Mar. 1982, 332 pp.

Vecchio, Frank J, and Michael P Colins. "The Modified Compression-Field Theory for Reinforced Concrete Elements Subjected to Shear." ACI Journal Proceedings, vol. 83, no. 2, 1986, pp. 219–231. doi:10.14359/10416.

Wu, Y., Malvar, L. J., Crawford, J. E., and Magallanes, J. M., "Performance of LS-DYNA Concrete Constitutive Models," for 12th International LS-DYNA Users Conference, Dearborn, MI, June 6-8, 2010.

Zienkiewicz, O.c., and R.l. Taylor. “The Finite Element Patch Test Revisited a Computer Test for Convergence, Validation and Error Estimates.” Computer Methods in Applied Mechanics and Engineering, vol. 149, no. 1-4, 1997, pp. 223–254. doi:10.1016/s0045-7825(97)00085-6.